

REPORT DOCUMENTATION PAGE

AFRL-SR-AR-TR-02-

Public reporting burden for this collection of information is estimated to average 1 hour per response, including the time for reviewing inst data needed, and completing and reviewing this collection of information. Send comments regarding this burden estimate or any other as this burden to Department of Defense, Washington Headquarters Services, Directorate for Information Operations and Reports (0704-011 4302). Respondents should be aware that notwithstanding any other provision of law, no person shall be subject to any penalty for failing valid OMB control number. PLEASE DO NOT RETURN YOUR FORM TO THE ABOVE ADDRESS.

0326

1. REPORT DATE (DD-MM-YYYY) 01-07-2002		2. REPORT TYPE Final		3. DATES COVERED (From - To) May 1999 - April 2002	
4. TITLE AND SUBTITLE Random Noise Polarimetry Technique for Covert Detection Of Targets Obscured by Foliage				5a. CONTRACT NUMBER F49620-99-1-0209	
				5b. GRANT NUMBER	
				5c. PROGRAM ELEMENT NUMBER	
6. AUTHOR(S) Narayanan, Ram, M.; Xu, Xiaojian; Henning, Joseph, A. and Kumru, Cihan				5d. PROJECT NUMBER	
				5e. TASK NUMBER	
				5f. WORK UNIT NUMBER	
7. PERFORMING ORGANIZATION NAME(S) AND ADDRESS(ES) University of Nebraska- Lincoln Department of Electrical Engineering Center for Electro-Optics 209N Walter Scott Engineering Center Lincoln, NE 68588-0511				8. PERFORMING ORGANIZATION REPORT NUMBER	
9. SPONSORING / MONITORING AGENCY NAME(S) AND ADDRESS(ES) Air Force Office of Scientific Research AFOSR/NM 801 N, Randolph Street, Suite 732 Arlington, VA 22203				10. SPONSOR/MONITOR'S ACRONYM(S) AFOSR/NM	
				11. SPONSOR/MONITOR'S REPORT NUMBER(S)	

12. DISTRIBUTION / AVAILABILITY STATEMENT
Approved for public release,
distribution unlimited

13. SUPPLEMENTARY NOTES

20021008 015

14. ABSTRACT
The University of Nebraska has been investigating a novel technique called random noise polarimetry for foliage penetration (FOPEN) imaging applications, under support from the US Air Force Office of Scientific Research (AFOSR). In this final report, we summarize the main activities and results of the research during the past three years (1999-2002). These include: (a) Development of an experimental UHF band ultra wideband (UWB) FOPEN noise radar system; (b) Development of a down range sidelobe suppression; (c) Study of the foliage transmission model and the impact of foliage obscuration; (d) Development of FOPEN SAR imaging model and image formation algorithms; (e) Study of the impact of frequency and aspect angle dependent target signatures on UWB SAR images; (f) Three-dimensional interferometric SAR and ISAR imaging techniques; (g) Development of SAR image enhancement techniques; and (h) Field tests, data acquisition and image processing using the experimental random noise radar system. Suggestions for future work are also presented.

15. SUBJECT TERMS Foliage penetration, Polarimetry, Radar, Random noise, Synthetic aperture radar (SAR), Image processing.				
16. SECURITY CLASSIFICATION OF: U		17. LIMITATION OF ABSTRACT UU	18. NUMBER OF PAGES 173	19a. NAME OF RESPONSIBLE PERSON
a. REPORT U	b. ABSTRACT U			c. THIS PAGE U

FINAL REPORT
RANDOM NOISE POLARIMETRY TECHNIQUE
FOR COVERT DETECTION OF TARGETS
OBSCURED BY FOLIAGE

Submitted by:

Dr. Ram M. Narayanan

Professor

Department of Electrical Engineering

Center for Electro-Optics

University of Nebraska

Lincoln, NE 68588-0511

Tel: (402)472-5141

Email: rnarayanan@unl.edu

Submitted to:

Dr. Arje Nachman

AFOSR/NM

Contract Number:

F49620-99-1-0209

Random Noise Polarimetry Technique for Covert Detection of Targets Obscured by Foliage

Abstract

The University of Nebraska has been investigating a novel technique called random noise polarimetry for foliage penetration (FOPEN) imaging applications, under support from the US Air Force Office of Scientific Research (AFOSR). In this final report, we summarize the main activities and results of the research during the past three years (1999-2002). These activities include: (a) Development and performance analysis of an experimental UHF band ultra wideband (UWB) FOPEN noise radar system operating at frequency band 250-500 MHz; (b) Development of a down range sidelobe suppression technique in UWB random noise radar imaging; (c) Study of the foliage transmission model and the impact of foliage obscuration on UWB synthetic aperture radar (SAR) images of complex targets; (d) Development of FOPEN SAR imaging model and image formation algorithms; (e) Study of the impact of frequency and aspect angle dependent target signatures on UWB SAR images; (f) Three-dimensional interferometric SAR and inverse SAR (ISAR) imaging techniques; (g) Development of SAR image enhancement techniques with applications to FOPEN SAR image processing; and (h) Field tests, data acquisition and image processing using the experimental random noise radar system. Suggestions for future work are also presented.

Subject Terms: Foliage penetration, Polarimetry, Radar, Random noise, Synthetic aperture radar (SAR), Image processing.

Contents

1	INTRODUCTION	1
2	THEORY OF UWB RANDOM NOISE RADAR IMAGING	5
2.1	Analytical Description of an Ultra-Wideband Gaussian Noise Process	5
2.2	Correlation Receiving in Random Noise Radars	8
2.2.1	Principles	8
2.2.2	Implementation	9
2.3	Down Range Resolution	10
2.4	Doppler Resolution	13
2.5	Range-Doppler 2-D resolution	14
3	RANGE SIDELobe SUPPRESSION FOR UWB RANDOM NOISE RADAR IMAGING	16
3.1	Background	16
3.2	Mathematical Representation of a Practical UWB Noise Radar System . . .	18
3.3	Sidelobe Suppression Technique	19
3.3.1	Performance Analysis of the PSF	19
3.3.2	Sidelobe Suppression by Apodization Filtering	21
3.3.3	Filter Coefficients Solution	22
3.4	Computational and Experimental Results	24
3.4.1	Computational Results	24
3.4.2	Application to Ground Penetration Noise Radar Data	26
3.5	Summary	28

4	IMPACT OF FOLIAGE OBSCURATION ON SAR IMAGES	30
4.1	Background	30
4.2	FOPEN Radar Imaging System Model	33
4.3	Foliage Transmission Modeling	34
4.3.1	Proposed statistical-physical model	35
4.3.2	Validation of the foliage transmission model	38
4.4	Foliage Obscuration Pattern Analysis	41
4.4.1	Distortion induced by amplitude fluctuations	43
4.4.2	Distortion induced by phase fluctuations	44
4.5	Comparative Study of Step-Frequency and Random Noise SAR Using Simulation	45
4.5.1	Brief description of the two systems	46
4.5.2	Comparison of the Ideal PSFs	46
4.5.3	Comparison of Anti-RFI Performance	47
4.5.4	Comparison of the Foliage Obscured PSFs	50
4.5.5	Comparison of the 2-D images for complex target	52
4.6	Summary	55
5	FOPEN UWB RANDOM NOISE SAR IMAGE FORMATION	61
5.1	Background	61
5.2	1-D Time Domain Radar Response Model	62
5.3	2-D FOPEN SAR Imaging Model	63
5.4	SAR Image Formation	67
5.5	2-D Image Sidelobe Reduction	71
5.5.1	Slant Range Apodization Filtering	71
5.5.2	Cross Range Sidelobe Reduction	72
5.6	Impact of Frequency and Azimuth Dependent Target RCS	73
5.6.1	Images of a Conducting Sphere	75
5.6.2	Images of a Conducting Circular Plate	76
6	THREE-DIMENSIONAL INTERFEROMETRIC ISAR IMAGING TECH- NIQUE	82

6.1	Background	82
6.2	3-D Imaging System Geometry	85
6.3	2-D Image Reconstruction	87
6.4	3-D IF-ISAR Image Processing	88
6.4.1	General Bistatic Imaging	89
6.4.2	Single Antenna Imaging	92
6.5	Image Formation Issues	92
6.5.1	Data Collection Constraints	93
6.5.2	Impact of Multiple Scattering Centers	93
6.6	Experimental Results	97
6.6.1	Two-Antenna Ground Plane Imaging	97
6.6.2	Slant Plane Imaging	98
6.7	Summary	101
7	EXPERIMENTAL RADAR SYSTEM AND TESTS RESULTS	102
7.1	Brief Description of the Experimental UWB Random Noise Radar	102
7.2	Performance Analysis of the FOPEN UWB Random Noise Radar System . .	105
7.2.1	System PSF and the down range resolving capability	106
7.2.2	System dynamic range and sensitivity	108
7.2.3	Impact of the number of integrated echo samples	108
7.3	Field Test Results	111
7.3.1	SAR Imaging on Unobscured Targets	111
7.3.2	SAR Imaging on Obscured Targets	113
8	FOPEN SAR IMAGE ENHANCEMENT	116
8.1	Background	116
8.2	A Brief Review of SVA and Super-SVA	119
8.2.1	SVA for 1-D image processing	119
8.2.2	Super SVA	122
8.3	A Modified Version of Noninteger Nyquist SVA	124
8.4	An Iterative Super-SVA Procedure for SAR Image Enhancement	128

8.4.1	2-D Noninteger Nyquist SVA for SAR image processing	128
8.4.2	An iterative super SVA procedure	131
8.5	Application Examples	133
8.5.1	Application to SAR Image Enhancement for ATR	134
8.5.2	Application to 3-D IF-ISAR Image Enhancement	143
8.6	Application of Super SVA to FOPEN Random Noise SAR Images	145
8.7	Summary	146
9	CONCLUSIONS AND FUTURE WORK	148
	Bibliography	150
	Appendix: Publication List	163

List of Figures

2.1	Block diagram of a random noise radar system.	8
2.2	Implementation of a time cross-correlation receiver.	10
2.3	Rectangular (a) and Gaussian (b) power spectral densities.	11
2.4	Average ambiguity function for UWB noise radar.	15
3.1	PSFs before and after filtering.	20
3.2	PSL and ISLR as functions of the normalized filter length.	25
3.3	PSL and ISLR as functions of the normalized mainlobe width.	26
3.4	True PSFs of the ground penetration noise radar before and after filtering. .	27
3.5	Comparison of ground penetration radar images before and after filtering processing.	28
4.1	Spotlight mode SAR imaging geometry.	33
4.2	System model for FOPEN radar imaging.	35
4.3	Comparison of the cumulative probability distributions.	39
4.4	Simulated amplitude and phase fluctuation vs. flight path.	40
4.5	Simplified diagrams of the two radar systems.	46
4.6	Ideal PSFs of the two radar systems.	48
4.7	ISLR and PSL as functions of the number of integration samples. The solid line shows the noise radar, while the dashed lines show the step-frequency radar with appropriate taper window.	49
4.8	ISLR and PSL as functions of the percentage bandwidth coverage of RFI. . .	51
4.9	Foliage obscured down range PSFs of the two radar systems.	53

4.10	Comparisons of the 2-D PSFs of the two radar systems. (a). Unobscured PSF for step-frequency radar; (b). Foliage obscured PSF for step-frequency radar; (c). Unobscured PSF for random noise radar; and (d). Foliage obscured PSF for random noise radar.	54
4.11	2-D images of step-frequency SAR.	56
4.12	2-D images of random noise SAR, integration number 32.	57
4.13	2-D images of random noise SAR, integration number 128.	58
4.14	2-D images of random noise SAR, integration number 512.	59
5.1	1-D FOPEN random noise radar response model	62
5.2	The 3-D and the equivalent 2-D imaging geometry for FOPEN random noise SAR.	64
5.3	The equivalent transmit pulse and its frequency spectrum	71
5.4	The spectral ROS of the focused SAR image.	73
5.5	Images of a point target with different synthetic aperture angles.	74
5.6	The frequency response of a conducting sphere of radius 150 cm.	77
5.7	The 2-D images of the conducting sphere for the UWB (left) and conventional (right) SAR's.	78
5.8	The RCS of a conducting circular plate of radius 150 cm.	79
5.9	The 2-D images of the conducting circular plate at a 30° incidence angle for the UWB (left) and conventional (right) SAR's.	80
6.1	3-D interferometric ISAR imaging geometry.	86
6.2	Multiple scattering centers at position (x, y)	94
6.3	Images of a scaled aircraft model.	99
6.4	Images of a T-72 tank.	100
7.1	Block diagram of the FOPEN random noise radar system	103
7.2	PSF of the FOPEN random noise radar system, channel-1 (above) and channel-2 (below).	107
7.3	System responses at different input power levels	109

7.4	System responses for different numbers of the integrated echo samples. . . .	110
7.5	The boom van-borned random noise SAR system.	112
7.6	2-D SAR images of a trihedral and a van in open air.	113
7.7	FOPEN random noise SAR image of two trihedral reflectors obscured behind trees.	114
7.8	Wall penetration SAR image of a trihedral reflector obscured behind wall. . .	115
8.1	The block diagram of super SVA procedure.	123
8.2	The IPRs for different aperture functions.	125
8.3	The block diagram of the iterative super SVA procedure.	132
8.4	Comparison of the super SVA SAR images using different noninteger Nyquist formulations.	135
8.5	Simplified block diagram of super SVA processing of the MSTAR SAR images.	136
8.6	SLICY images, from top to bottom, left to right: Target photograph, Original MSTAR image; Equalized image, Taylor windowed image; SVA image, Super SVA image-2; Super SVA image-4, and Super SVA image-6.	137
8.7	SLICY images using 25% partial phase history data, from top to bottom, left to right: Unwindowed image from partial data, Taylor windowed image; SVA image, Super SVA image-1; Super SVA image-2, Super SVA image-3; Super SVA image-4, and Super SVA image-6.	138
8.8	T72-A64 images, from top to bottom, left to right: Target photograph, Orig- inal MSTAR image; Equalized image, Taylor windowed image; SVA image, Super SVA image-1; Super SVA image-2, and Super SVA image-3.	141
8.9	Clutter images, from top to bottom, left to right: Original MSTAR image, SVA image, Super SVA image-1; and Super SVA image-3.	142
8.10	Amplitude distribution of the original (blue) and the super SVA (red) images .	142
8.11	Super SVA IF-ISAR images of an aircraft model.	144
8.12	Spectral ROS used in super SVA image enhancement	146
8.13	Super SVA image enhancement of the FOPEN random noise SAR image of two trihedral reflectors obscured behind foliage	147

Chapter 1

INTRODUCTION

Ultra wideband (UWB) radar has proven to be a very powerful tool for underground and foliage obscured object detection and identification [1]-[4]. The combination of using low frequencies (which exhibit very good foliage and ground penetration capabilities) such as VHF and UHF bands or even lower, and using UWB waveforms (which provide very high range resolution), creates a wide variety of applications. The UWB waveforms can be impulse waveform, linear FM (LFM), step-frequency, random noise, and so on. Among various UWB interrogation signals, random noise waveform would be a desirable choice for military applications.

Research work has been conducted on the subject of using random or pseudo-random noise signals as a radar transmit waveform since the early 1950s [5]-[7]. In recent years, the research results from several research groups around the world have shown that random noise radar is a promising UWB technique to achieve high resolution in both range and velocity, and for both military and civilian applications [8]-[16]. For foliage penetration (FOPEN) imaging applications, the transmission of a UWB random noise waveform provides additional advantages. Random noise radars are relatively inexpensive to build and possess inherent immunity to jamming and interference from other radar systems or electronic facilities operating in the same theater of operations. In fact, a coherent random radar system usually provides a simplified system design while preserving all the advantages and avoiding the drawbacks possessed by conventional radar systems, such as impulse, linear frequency-modulated (LFM) or step-frequency radars. These include yielding high resolu-

tion, preservation of scattering phase characteristics, inherent low probability of intercept (LPI), low probability of detection (LPD), and immunity from the impacts of antenna coupling as well as radio frequency interference (RFI), which usually has severe impact on the radar operation at VHF and UHF bands, and so on.

Different noise radar systems have been designed and used for various applications, such as the measurement of radar cross section (RCS) and target range profiles [8], moving target Doppler estimation [9], detection and imaging of objects buried underground [10], interferometry [11], SAR [12, 13] and ISAR imaging [14, 15, 16] and so on. This list is far from complete and does not reflect the extent of the literature on noise radar development. A more complete list of the references were provided by Liu *et al.*[17].

The University of Nebraska has developed a novel technique that permits coherent processing of backscatter data acquired by a radar that transmits UWB random noise signals. In this technique, a truly random noise signal within the desired frequency band is transmitted toward the target, and detection is accomplished by employing a heterodyne correlation receiver that preserves the phase as well as the amplitude of the received signal. This process is accomplished by mixing the delayed transmit replica by a phase-locked coherent oscillator prior to the correlation operation. Thus, coherent processing algorithms can be used to enhance the detection of targets or to reduce the clutter effects. Furthermore, reception of orthogonally polarized signals reflected from target permits the extraction of the target's polarimetric phase for improved detectability and better target identification. This noise radar technique has been used in various applications, such as ground penetration detection of buried objects, Doppler estimation and interferometry, SAR and ISAR imaging [9, 10, 11, 12, 15] and so on.

In the current work, we investigate the extension of the coherent UWB random noise radar concept to foliage penetration applications, under support from the US Air Force Office of Scientific Research (AFOSR). The three-year research work started in 1999. This final report summarizes the research activities and results of the three-year research project. During the past three years, our research had focused on the following topics:

(a) Development and performance analysis of an experimental UHF band UWB FOPEN noise radar system operating at frequency band 250-500 MHz;

- (b) Development of a down range sidelobe suppression technique in UWB random noise radar imaging;
- (c) Study of the foliage transmission model and the impact of foliage obscuration on UWB SAR images of complex targets;
- (d) Development of FOPEN SAR imaging model and image formation algorithms;
- (e) Study of the impact of frequency and aspect angle dependent target signatures on UWB SAR images;
- (f) Three-dimensional interferometric SAR and ISAR imaging techniques;
- (g) Development of SAR image enhancement techniques with applications to FOPEN SAR image processing; and
- (h) Field tests, data acquisition and image processing using the experimental random noise radar system.

The remainder of this report is organized as follows. In Chapter 2, the theory of UWB random noise radar imaging is briefly introduced. This includes an analytical description of UWB random noise radar waveforms, correlation receiving technique and the random noise radar system model, and the principles of two-dimensional (2-D) resolution. In Chapter 3, after an in-depth analysis of the performance of the point-spread function (PSF) of a UWB random noise imaging radar system, we develop an apodization filtering technique for down range sidelobe suppression in UWB random noise radar imaging. Both computational and experimental results are presented. Chapter 4 analyzes the impact of foliage obscuration on the SAR images of complex targets. A physical-statistical model for foliage transmission is first proposed and validated. The foliage obscuration pattern of a point target is then analyzed in terms of the theory of paired echoes. By computer simulation, a comparative study of step-frequency and random noise SAR is conducted. A complete FOPEN SAR imaging model and the corresponding SAR image formation procedure are presented in Chapter 5. An analysis of the impact of frequency and aspect dependent target radar cross section (RCS) on the 2-D images is also given in this chapter. Chapter 6 develops a three-dimensional (3-D) interferometric ISAR imaging technique, with applications to both

indoor and outdoor range phase history data of complex targets. In Chapter 7, a brief description and a performance analysis of the experimental UWB random noise radar system and typical field test results are given. A powerful SAR image enhancement technique, namely, the modified spatially variant apodization (SVA) technique, is proposed in Chapter 8. The applications of this technique include the enhancement of MSTAR SAR images for automatic target recognition (ATR), ISAR image enhancement in 3-D interferometric ISAR imaging, and FOPEN UWB random noise SAR images enhancement. Finally, in Chapter 9, we conclude the report and provide suggestions for future work.

Chapter 2

THEORY OF UWB RANDOM NOISE RADAR IMAGING

2.1 Analytical Description of an Ultra-Wideband Gaussian Noise Process

In several communications books (e.g., [18]-[20]), the following equation is used to represent a *narrow band* wide-sense stationary (WSS) Gaussian process with zero-mean and variance σ^2 :

$$s(t) = s_I(t) \cos(2\pi f_0 t) - s_Q(t) \sin(2\pi f_0 t), \quad (2.1)$$

where $s_I(t)$ and $s_Q(t)$ are Gaussian, f_0 is the central frequency, and the term *narrow band* means that the system fractional bandwidth $\frac{B}{f_0} \ll 1$. Eq. (2.1) can also be represented as

$$s(t) = A(t) \cos[2\pi f_0 t + \phi(t)], \quad (2.2)$$

where $A(t)$ is the envelope function

$$A(t) = \sqrt{s_I^2(t) + s_Q^2(t)}, \quad (2.3)$$

which has a Rayleigh distribution, while $\phi(t)$ is the phase function

$$\phi(t) = \tan^{-1} \left[\frac{s_Q(t)}{s_I(t)} \right], \quad (2.4)$$

which is uniformly distributed over $[-\pi, +\pi]$.

In the following, we show that any band-limited WSS Gaussian process can be represented by Eq. (2.1) or (2.2), whether it is a *narrow band* or an *ultra wideband* random process.

Without loss of generality, let us represent the random process in the time interval $[-T_0/2, T_0/2]$. This allows us to consider the process to be a cyclostationary random process (with the period $T_0 \rightarrow \infty$). The Fourier series expansion of a cyclostationary random process converges in the sense of mean square to the process [20]. We make use of the Fourier series to represent the band-limited Gaussian process $s(t)$ in the interval $[-T_0/2, T_0/2]$:

$$s(t) = \sum_{k=1}^{\infty} [a_k \cos(2\pi k f_1 t) + b_k \sin(2\pi k f_1 t)], \quad (2.5)$$

where $f_1 = \frac{1}{T_0}$, and

$$\begin{aligned} a_k &= \frac{2}{T} \int_{-T_0/2}^{T_0/2} s(t) \cos(2\pi k f_1 t) dt, \\ b_k &= \frac{2}{T} \int_{-T_0/2}^{T_0/2} s(t) \sin(2\pi k f_1 t) dt. \end{aligned} \quad (2.6)$$

And we also have

$$\begin{aligned} s_I(t) &= \sum_{k=1}^{\infty} [a_k \cos(2\pi f_k t) + b_k \sin(2\pi f_k t)], \\ s_Q(t) &= \sum_{k=1}^{\infty} [a_k \sin(2\pi f_k t) - b_k \cos(2\pi f_k t)], \end{aligned} \quad (2.7)$$

where $f_k = k f_1 - f_0$. Using the fact that $E[a_k b_m] = 0$ for $k \neq m$ and $E[a_k^2] = E[b_k^2]$, it is easy to show that

$$E[s_I(t) s_Q(t)] = 0, \quad (2.8)$$

where $E[\cdot]$ denotes the expectation operation. Thus, $s_I(t)$ and $s_Q(t)$ are uncorrelated in the limit of $T_0 \rightarrow \infty$. Since $s_I(t)$ and $s_Q(t)$ are also Gaussian, they are independent and the joint probability density function (PDF) can be written as

$$p_{IQ}(s_I, s_Q) = p_I(s_I)p_Q(s_Q). \quad (2.9)$$

We also have

$$E[s_I^2(t)] = E[s_Q^2(t)] = E[a_k^2] = E[b_k^2] = E[s^2(t)] = \sigma^2. \quad (2.10)$$

Therefore, if $s(t)$ is a WSS Gaussian process, the joint PDF in Eq. (2.9) can be expressed as

$$p_{IQ}(s_I, s_Q) = \frac{1}{2\pi\sigma^2} \exp\left\{-\frac{s_I^2 + s_Q^2}{2\sigma^2}\right\}. \quad (2.11)$$

The joint PDF $p_{A\phi}(A, \phi)$ of the envelope function, $A(t)$, and the phase function, $\phi(t)$, can be found by using

$$p_{A\phi}(A, \phi) = p_{IQ}(s_I, s_Q) \left| J\left(\frac{s_I, s_Q}{A, \phi}\right) \right|, \quad (2.12)$$

where $J(\cdot)$ is the determinant of the Jacobian transformation matrix, and $\left| J\left(\frac{s_I, s_Q}{A, \phi}\right) \right| = A$.

Thus Eq. (2.12) becomes

$$p_{A\phi}(A, \phi) = \begin{cases} \frac{A}{2\pi\sigma^2} \exp\left\{-\frac{A^2}{2\sigma^2}\right\} & \text{if } A \geq 0 \\ 0 & \text{otherwise} \end{cases}, \quad (2.13)$$

and the univariate PDF for $A(t)$ and $\phi(t)$ can then be found to be, respectively,

$$p_A(A) = \begin{cases} \frac{A}{\sigma^2} \exp\left\{-\frac{A^2}{2\sigma^2}\right\} & \text{if } A \geq 0 \\ 0 & \text{otherwise} \end{cases}, \quad (2.14)$$

and

$$p_\phi(\phi) = \begin{cases} \frac{1}{2\pi} & \text{if } -\pi \leq \phi < \pi \\ 0 & \text{otherwise} \end{cases}, \quad (2.15)$$

i.e., the envelope function has a Rayleigh PDF, while the phase function is uniformly distributed over $[-\pi, \pi]$.

In the above derivation, there is no additional constraint on the central frequency f_0 and the system bandwidth B . Therefore, we conclude that Eqs. (2.1) and (2.2) are valid for any

band-limited WSS Gaussian process, whether it is narrow band or ultra-wideband, as long as $\frac{B}{f_0} \leq 2$, which is a physical limit for real-world radar systems. This allows us to represent an ultra-wideband Gaussian process using a complex analytical signal of the form

$$s(t) = \frac{1}{2}[s_c(t)e^{j2\pi f_0 t} + s_c^*(t)e^{-j2\pi f_0 t}], \quad (2.16)$$

where $s_c(t) = s_I(t) + js_Q(t)$ is the complex envelope, and $*$ denotes complex conjugate.

2.2 Correlation Receiving in Random Noise Radars

2.2.1 Principles

We consider the simplified diagram of a random noise radar system as shown in Figure 2.1. A band-limited Gaussian noise signal is generated and radiated from the transmit antenna. A replica of the transmit signal is delayed and correlated with the received signal. The correlation receiver consists of a delay line and a correlator.

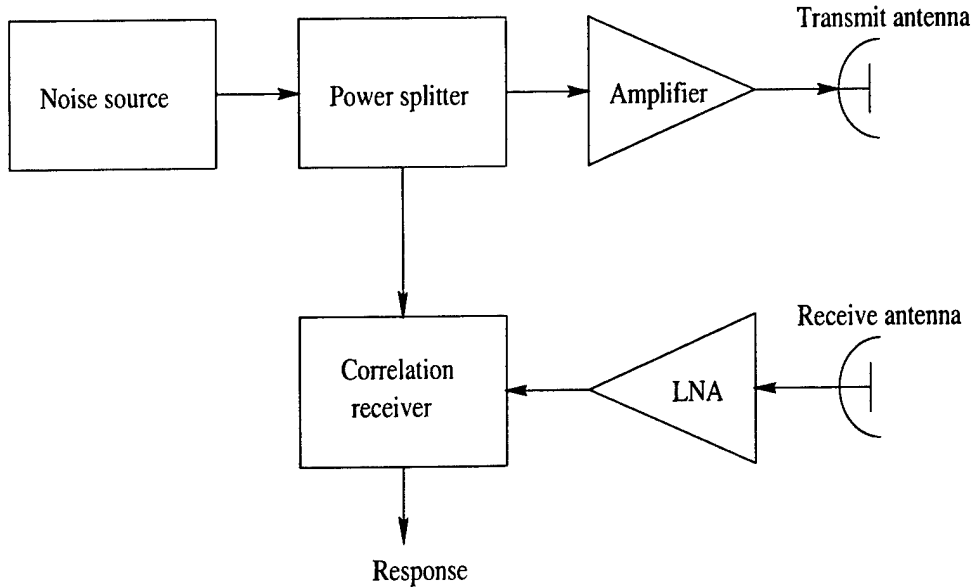


Figure 2.1: Block diagram of a random noise radar system.

Assume that the radar transmits a WSS band-limited Gaussian waveform, $s(t)$, with zero mean. $s(t)$ is also ergodic. The received signal by the receive antenna can be written as

$$r(t) = \int_{-L/2}^{L/2} \rho(\zeta) s(t - \zeta) d\zeta + n(t), \quad (2.17)$$

where $\rho(t)$ is the one-dimensional (1-D) target reflectivity function or range profile; $n(t)$ represents any *additive* noise and/or interference; and L represents the time span of the extended target in down range.

According to random process theory, $r(t)$ is also stationary and ergodic. Therefore, a time cross-correlation can be used to approximate the cross-correlation function between a time-delayed (and conjugated) transmit signal, $s^*(t - \zeta)$, and the received signal, $r(t)$, *i.e.*,

$$g_T(\tau) = \int_{-T/2}^{T/2} \int_{-L/2}^{L/2} \rho(\zeta) s(t - \zeta) s^*(t - \tau) d\zeta dt + \int_{-T/2}^{T/2} n(t) s^*(t - \tau) dt, \quad (2.18)$$

where T is the correlation integration period. For a large integration period T , the second term in Eq.(2.18) is equal to zero for any $n(t)$ which is uncorrelated to the transmit signal $s(t)$. Thus we have

$$g(\tau) = \lim_{T \rightarrow \infty} g_T(t) = \int_{-T/2}^{T/2} \rho(\zeta) p(\tau - \zeta) d\zeta = \rho(\tau) \otimes p(\tau), \quad (2.19)$$

where \otimes denotes convolution, and

$$p(\tau) = \lim_{T \rightarrow \infty} \int_{-T/2}^{T/2} s(t) s^*(t - \tau) dt \quad (2.20)$$

is the auto-correlation function of the transmit random noise waveform.

2.2.2 Implementation

The fact that for two WSS, ergodic random processes, the cross-correlation function can be approximated using their time cross-correlation of the samples, as discussed in afore subsection, allows us to implement a radar correlation receiver by using a mixer followed by a narrow band low-pass filter, as shown in Figure 2.2 [10, 21].

In this implementation, the received signal is mixed with a time-delayed version of the transmit waveform, $s(t - \tau)$. The correlation integration is performed by the low-pass filter (in fact, it performs convolution). The bandwidth of the low-pass filter determines the period

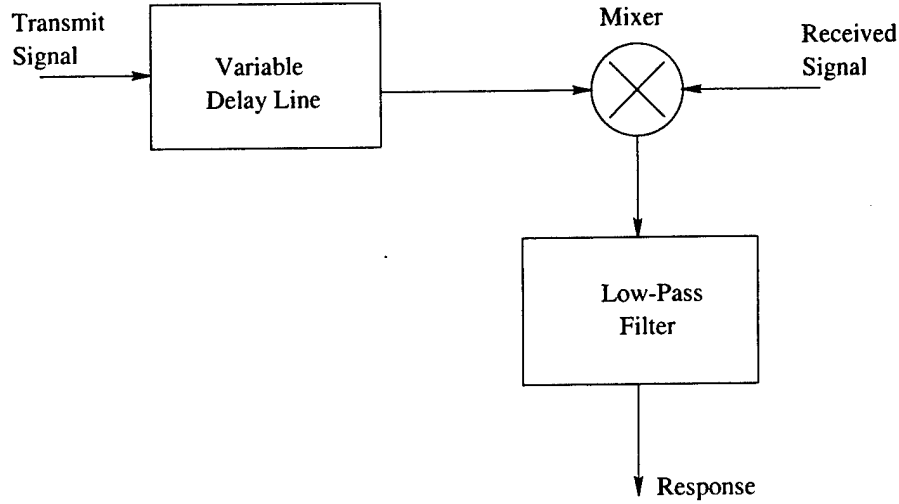


Figure 2.2: Implementation of a time cross-correlation receiver.

of the cross correlation integration, T . Therefore, for a higher accuracy, a very narrow bandwidth of the low-pass filter is preferred.

From the relationships of the Hilbert transform and correlation functions of two random processes, it is also known that the responses at a specified time delay can be demodulated using an in-phase and quadrature-phase (I/Q) detector to yield the amplitudes and phases of the received (and correlation processed) target signals.

For random noise radar imaging application, we need to acquire the signals as a function of the two-way delay, $\tau = \frac{2d}{c}$, where d is the distance between the target scattering cell and the radar, and c is the wave propagation speed. This can be implemented by simply using a computer controlled variable delay line.

2.3 Down Range Resolution

It is seen from Eq.(2.19) that the received target response, $g(\tau)$, is a convolution between the target range profile, $\rho(\tau)$, and the auto-correlation function of the radar transmit waveform, $p(\tau)$. This means that the down range resolution is determined by the auto-correlation function in Eq.(2.20), which in turn, is determined by the bandwidth and the shape of the power spectrum of the transmit waveform. We consider two types of the frequency spectral

shapes, the rectangular and the Gaussian shaped power spectra, as shown in Figure 2.3.

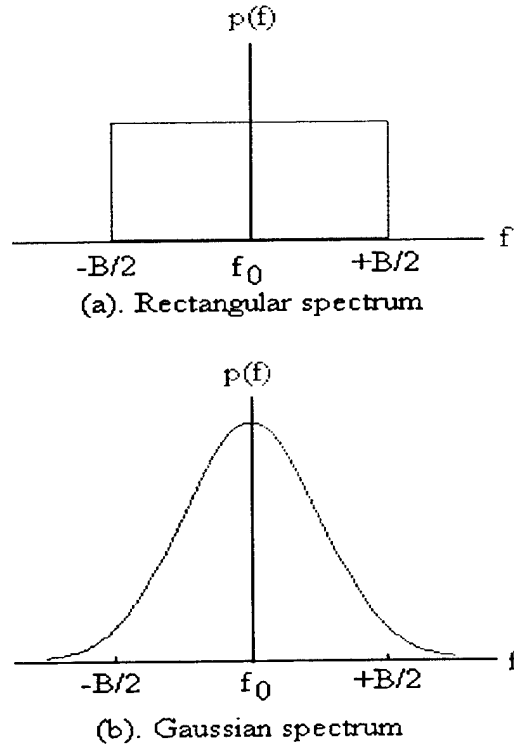


Figure 2.3: Rectangular (a) and Gaussian (b) power spectral densities.

Consider that the radar transmit waveform is a band-limited Gaussian noise with central frequency f_0 , bandwidth B , and with a rectangular shape of the power spectral density, i.e.,

$$P_{\Pi}(f) = A_0 \Pi_{[f_0 - B/2, f_0 + B/2]}(f) \quad (2.21)$$

where Π_F is a rectangular function of the set F . Correspondingly, the auto-correlation function is given by

$$p(\tau) = A_0 \text{sinc}(B\tau) e^{j2\pi f_0 \tau} = p_0(\tau) e^{j2\pi f_0 \tau}, \quad (2.22)$$

where

$$p_0(\tau) = A_0 \text{sinc}(B\tau), \quad (2.23)$$

and $\text{sinc}(t) = \frac{\sin(\pi t)}{\pi t}$.

Equations (2.22) and (2.23) state that for radars which use band-limited Gaussian noise as the transmit waveform, its auto-correlation function, $p(\tau)$, is a sinc pulse modulated by a carrier frequency f_0 . In the correlation receiver, however, it is possible that the modulated central frequency f_0 be demodulated using appropriate hardware or through signal processing. Therefore, function $p_0(\tau)$ determines the time resolution (*i.e.*, down range resolution) of the radar system. It is observed that the mainlobe width of $p_0(\tau)$ is determined by the transmit signal bandwidth B , *i.e.*,

$$\delta_R = \frac{c}{2B} \quad (2.24)$$

which determines the time (or down range) resolution of the imaging radar system.

The major drawback of the rectangular spectrum signal is that it results in an auto-correlation function with very high sidelobes that also spread to infinity in time domain, which are undesirable in a practical random noise radar imaging system. To overcome this drawback, the spectrum of the transmit noise waveform can be shaped using a bandpass filter with desired frequency response, so that the undesirable high sidelobes of the sinc function are suppressed. One of the choices is a Gaussian shaped spectrum, as shown in Figure 2.3b. We consider that the random signal has a Gaussian spectral shape, with a 3-dB bandwidth B and centered at frequency f_0 , *i.e.*,

$$P_G(f) = A_0 e^{-\frac{(f-f_0)^2}{B^2}}, \quad (2.25)$$

The auto-correlation can then be found to be

$$p_G(\tau) = A_0 B \sqrt{\pi} e^{-(\pi \tau B)^2} e^{j2\pi f_0 \tau} = \frac{A_0 \sqrt{\pi}}{\tau_B} e^{-(\frac{\pi \tau}{\tau_B})^2} e^{j2\pi f_0 \tau} \quad (2.26)$$

where $\tau_B = 1/B$. It is seen that a wide enough bandwidth B of the random signal provides fast decay of correlation. Therefore, in this case, the resolution is still determined by the transmit signal bandwidth.

Eqs.(2.22) and (2.26) also tell us that a UWB random noise radar can be modeled as a UWB short-pulse radar which transmits a short pulse and receives the returned signal using

an ideal sampler at specified time delays.

2.4 Doppler Resolution

Consider a point target with amplitude ρ_0 and initial phase ϕ_0 , which is at a distance R and is moving with a radial velocity v with respect to the radar. At time t the delay caused by the two-way distance can be expressed as

$$\tau = \frac{2R}{c} + \frac{2v}{c}t. \quad (2.27)$$

Using the representation of the transmit signal in Eq. (2.16), the received target signal can be expressed as

$$r(t - \tau) = \frac{1}{2}\rho_0 e^{-j\phi_0} [s_c(t - \tau)e^{j2\pi f_0(t-\tau)}] + s_c^*(t - \tau)e^{-j2\pi f_0(t-\tau)}. \quad (2.28)$$

This received signal is correlated with a delayed replica of the transmit signal $s(t - \tau_d)$, *i.e.*,

$$g_c(\tau, \tau_d) = \int_{-T/2}^{T/2} r(t - \tau) s^*(t - \tau_d) dt. \quad (2.29)$$

When using I and Q demodulator in the correlation receiver, assuming $\tau_d = 2R/c$ and denoting the delay rate by $\alpha = 2v/c$, from Eq. (2.29) the responses of the I and Q channels are [22], respectively,

$$\begin{aligned} g_I(\alpha) &= \frac{\rho_0}{2} \int_{-T/2}^{T/2} p_0(\alpha t) \cos[2\pi\alpha f_0 t - \phi_0] dt, \\ g_Q(\alpha) &= \frac{\rho_0}{2} \int_{-T/2}^{T/2} p_0(\alpha t) \sin[2\pi\alpha f_0 t - \phi_0] dt. \end{aligned} \quad (2.30)$$

where

$$p_0(\alpha t) = \frac{\sin(\pi\alpha Bt)}{\pi\alpha Bt}. \quad (2.31)$$

Therefore, the final response of the correlation receiver is

$$g_c(\alpha) = g_I(\alpha) + jg_Q(\alpha) = \rho_0 \int_{-T/2}^{T/2} p_0(\alpha t) e^{j(2\pi\alpha f_0 t - \phi_0)} dt. \quad (2.32)$$

When $T \leq \frac{1}{2\alpha B}$, we have $p_0(\alpha t) \simeq 1$, and the integration in Eq. (2.32) results in a sinc function. On the other hand, in the limit of $T \rightarrow \infty$, the integration in Eq. (2.32) results in a rectangular pulse, with the pulse width being dependent on αB . Therefore, in random noise radar imaging, the Doppler resolution is determined by the integration time T as well as the bandwidth of the transmitted random noise waveform B .

2.5 Range-Doppler 2-D resolution

In the above analysis, the Doppler resolution can be obtained in different ways, e.g., when a stationary radar illuminates on moving targets, a moving radar illuminates on stationary targets, or both the radar and the targets are moving, while the down range resolution is achieved through a wideband noise signal waveform. This is virtually the same as that in conventional SAR and ISAR. As a consequence, a refinement of the conventional SAR and ISAR techniques is usually applicable for random noise radar range-Doppler two-dimensional (2-D) imaging.

As an illustrative example of the 2-D resolution capability of UWB random noise radar, Figure 2.4(a)-(d) [22] demonstrates the 2-D ambiguity function with integration time $T = 50$ and 10 msec for transmit waveform bandwidth $B = 1$ GHz and $B = 100$ MHz, respectively. It is worthy to note that, in addition to its inherent covertness and anti-jamming characteristics, random noise radar also has another promising property: It has a nearly ideal 2-D thumbtack ambiguity function, i.e., unlike conventional radar waveforms, there is no range ambiguity and relatively small impact of the signal bandwidth on the Doppler resolution when random noise waveform is used. This can be clearly seen in Figure 2.4.

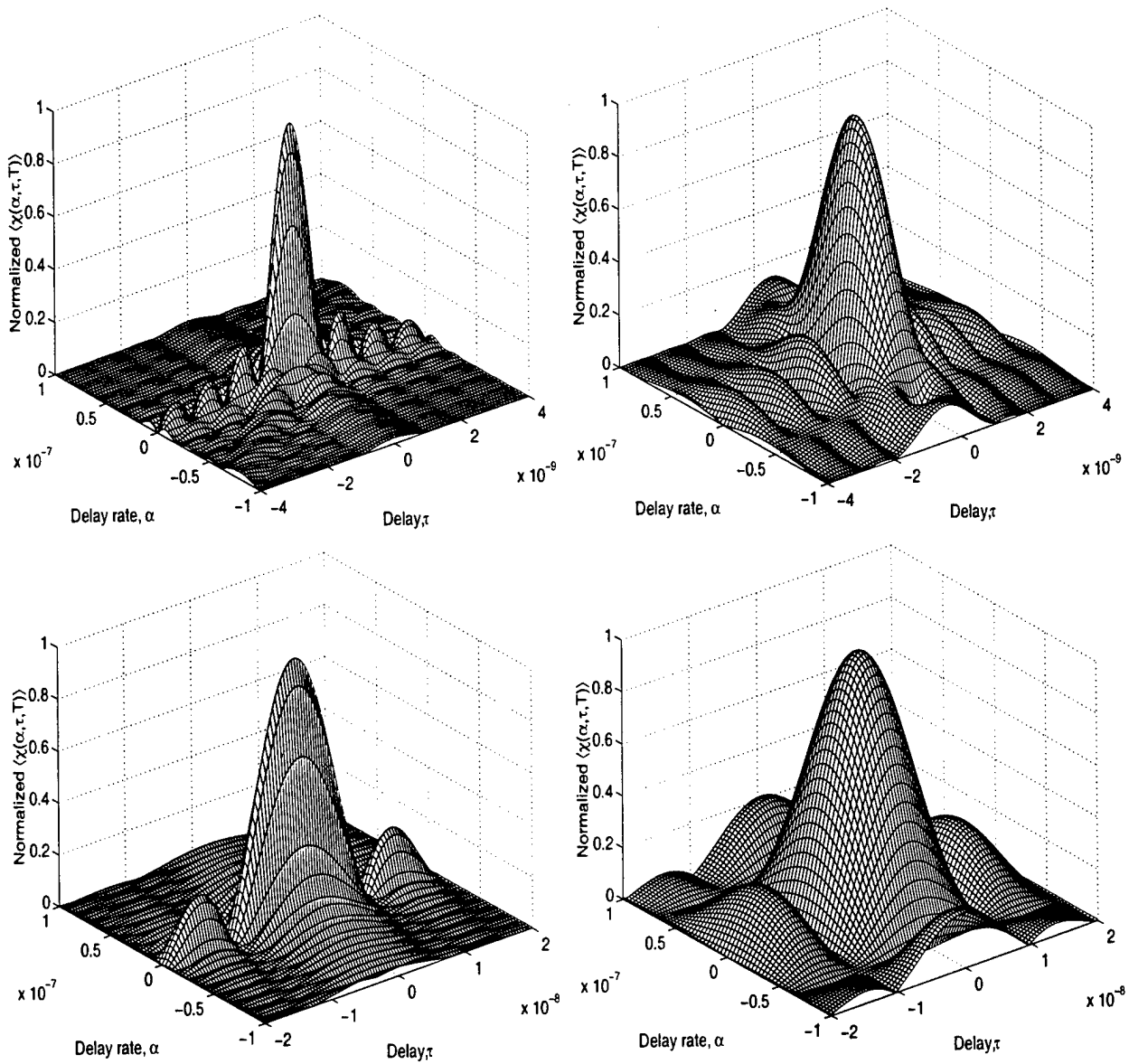


Figure 2.4: Average ambiguity function for UWB noise radar.

Chapter 3

RANGE SIDELOBE SUPPRESSION FOR UWB RANDOM NOISE RADAR IMAGING

3.1 Background

UWB random noise radar that transmits a band-limited random waveform had been found to be very useful in high resolution imaging [21],[23]-[25]. However, the system suffers from high range sidelobes resulting in images with reduced dynamic range, due to the effect of the bandpass and random characteristics of the transmitted noise signals. This in turn affects target detection and identification, especially in foliage and/or ground penetration applications, where received signal levels depend on the attenuation of the lossy media, as well as the radar cross section of the targets [4, 26]. To improve the dynamic range, it is required to suppress these sidelobes using signal processing algorithms.

It is known that in radar imagery, a point-like scatterer within the scene will have a complex image representation given by the impulse response, or the point spread function (PSF) of the imaging system. For a rectangular window function, the PSF is a *sinc* function, where the largest sidelobe is about 13 dB below the peak of the mainlobe. The range sidelobes have traditionally been reduced by applying an amplitude weighting function to

the frequency domain data prior to forming the range profiles by performing fast Fourier transform (FFT). This process is called spectral weighting or windowing. A variety of taper window functions have been developed for such applications [27].

The spectral weighting method requires that the PSF of the imaging radar system have a *sinc* kernel. This cannot be always the case in various practical radar imaging operation. Examples for such exceptional cases are radar imaging with spectrally thinned wideband waveforms [28], or with randomly thinned large antenna arrays [29]. In these applications, some image domain deconvolution procedures are developed [30]. Among them, the well-known CLEAN technique [31, 32] is one such image processing algorithm for sidelobe reduction applications. The CLEAN algorithm is an iterative procedure that successively picks out the strongest point in the image, assumes it is a true scatterer with the corresponding magnitude, and removes its point spread response from the image so that the effect of the sidelobes can be greatly reduced. The CLEAN technique was proved to be very effective in sidelobe reduction in radar imaging. However, this technique requires that the brightest spot in the image be a true scatterer to guarantee the success of this procedure. This, in turn, requires that the mainlobe of the PSF have a single peak.

In UWB random noise radar imaging, the range profiles are obtained by direct time domain sampling through changing the time-delay in the correlation receiver. It is then ready to find that the spectral weighting technique cannot be directly applied to the image processing. As will be shown later, the PSF of a practical UWB random noise radar system, which transmits bandpass-limited random noise signals and receives the target returns by using a correlation receiver, neither has a simple *sinc* PSF, nor can the brightest spot in the image guarantee to represent the exact position of a true scatterer. Thus, an image domain deconvolution method such as CLEAN technique seems not a good choice. Furthermore, even if it is possible to apply other image domain deconvolution procedures, it is preferable to find an alternate technique for the sidelobe suppression, as an image domain deconvolution procedure not only is usually noise sensitive, but also requires time-consuming iterations, thus making real-time image processing difficult or even impossible.

In this chapter, we investigate the range sidelobe suppression technique for the coherent UWB random noise radar. An image domain filtering technique, which combines apodiza-

tion filtering and median filtering, is proposed. The term apodization filtering is used to distinguish this technique from the conventional spectral weighting and image domain deconvolution. A mathematical representation of the random noise radar system is presented in Section 3.2. In Section 3.3, an image domain apodization filtering procedure for range sidelobe suppression is developed based on the performance analysis of the PSF. Both computational and experimental results of image processing by using the apodization filtering technique are presented in Section 3.4. Finally, Section 3.5 provides a summary of the work and some conclusions.

3.2 Mathematical Representation of a Practical UWB Noise Radar System

A simplified representation of the random noise radar system was shown in Figure 2.1. As discussed in Chapter 2, when the random noise signal source generates a zero-mean band-limited WSS Gaussian random process, with variance σ_n^2 , for an ideal point target, the output of the radar correlation receiver can be expressed as

$$P(\tau) = \rho(\tau) \otimes p(\tau), \quad (3.1)$$

where \otimes denotes convolution, and

$$p(\tau) = \lim_{T \rightarrow \infty} \int_{-T/2}^{T/2} s(t) s^*(t - \tau) dt \quad (3.2)$$

is the auto-correlation function of the transmit random noise waveform.

In Eqs.(3.2) and (3.2) the response of the transmit and receive antennas was not included. Suppose that the transmit and the receive antennas have impulse responses $A_t(t)$ and $A_r(t)$, respectively. Then the PSF of the imaging radar system can be written as [33]

$$P(\tau) = A_t(\tau) \otimes A_r(\tau) \otimes p(\tau). \quad (3.3)$$

This PSF accounts for all the effects of the transmitter channel, receiver channel, and the bandpass-limited random noise signal, on the down range resolution performance of the

radar system.

3.3 Sidelobe Suppression Technique

3.3.1 Performance Analysis of the PSF

The down range resolution mainly depends on the PSF of the radar system, $P(\tau)$. Returning to Eq.(3.3), if both of the transmit and receive channels of the radar system are ideal in their operation bandwidths, so that their transfer functions are $A_t(\tau) = A_r(\tau) = \delta(\tau)$, then we have

$$P(\tau) = p(\tau). \quad (3.4)$$

In this case, the PSF $P(\tau)$ is essentially determined by the impulse response of the bandpass filter, or by the auto-correlation function of the transmit waveform $p(\tau)$. For a uniform spectral shape, this is given by Eq.(2.22), or in its real signal form

$$p(\tau) = \text{sinc}(2\pi B\tau) \cos(2\pi f_0\tau). \quad (3.5)$$

where B is the bandwidth, and ω_0 is the central angular frequency of the bandpass filter.

Figure 3.1(a) illustrates an example of the PSF represented by Eq.(3.5), where the radar parameters are as follows: central frequency $f_0 = 1.5$ GHz, bandwidth $B = 1.0$ GHz, sampling time interval $\Delta\tau = 0.156$ ns.

The kernel of the PSF is a *sinc* function modulated by a *cosine* function, with the former having a variable $2\pi B\tau$ and the latter having a variable $2\pi f_0\tau$. In conventional radar operation, where $f_0 \gg B$, the effect of this *cosine* modulation in the PSF is eliminated by the demodulation in the radar receivers. However, for a UWB random noise radar which transmits and receives bandpass-limited noise signals, and where f_0 and B are comparable in magnitude, the effect of the *cosine* modulation cannot be simply eliminated. This is because the returned signals are received and directly sampled in time domain and the sampling frequency may be several times higher than the radar central frequency.

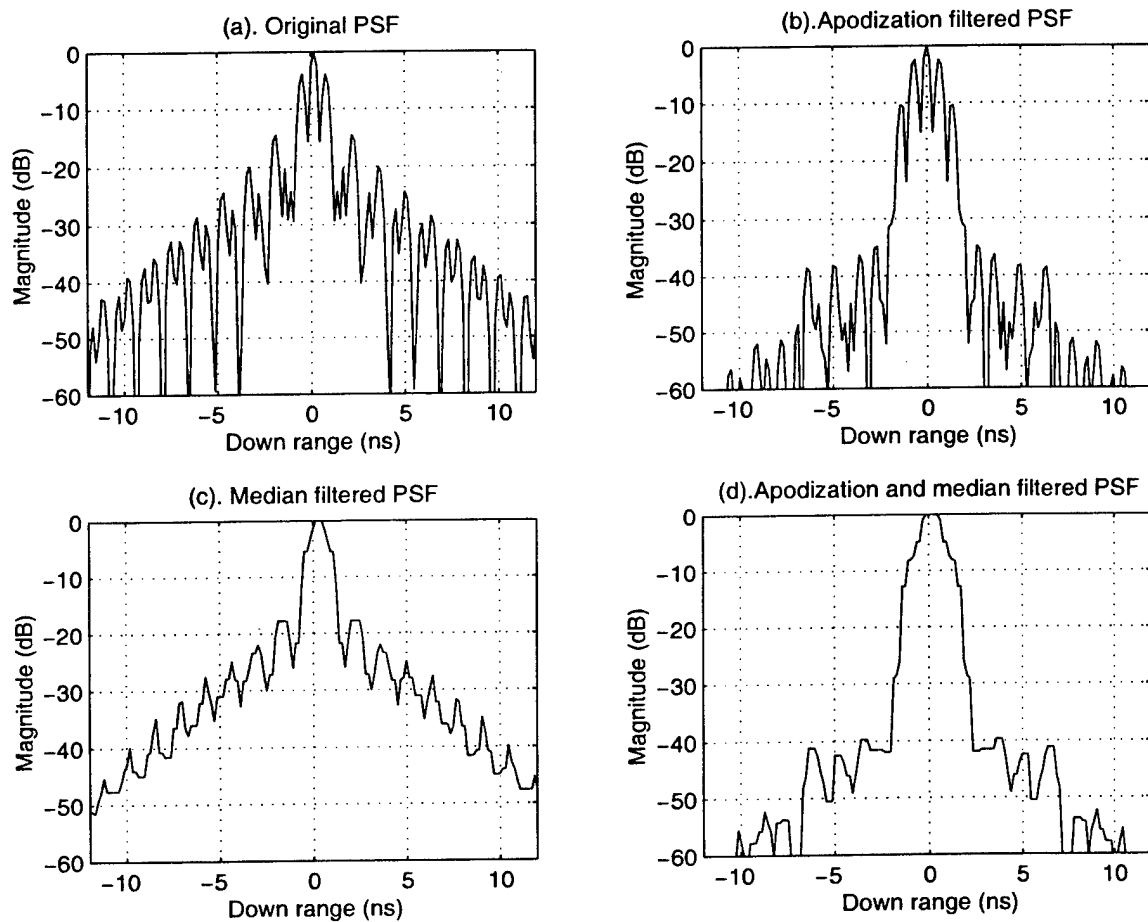


Figure 3.1: PSFs before and after filtering.

As a consequence, the PSF of the UWB random noise radar has the following unique characteristics: Instead of a smooth mainlobe with a single peak like the *sinc* function, this PSF has a mainlobe with multiple peaks resulting from the modulation of $\cos(\omega_0\tau)$. This mainlobe, when affected by the the transmit random noise signals, will become uncharacteristic. As a result, the brightest pixel in the image is not necessarily at the exact location of the scatterer, if the image is left unprocessed.

3.3.2 Sidelobe Suppression by Apodization Filtering

From the above section, it is shown that in UWB random noise radar imaging, the high range sidelobes cannot be reduced either by simply spectral weighting using conventional window functions, due to the direct sampling in time domain, or by the CLEAN algorithm due to the uncharacteristic mainlobe shape of the PSF.

However, noticing that a spectral weighting in the frequency domain is equivalent to a convolution in image domain (time domain), an image domain filtering technique can be developed. This technique is called apodization filtering. By apodization filtering, we mean that, we are going to find a special image domain filtering function, such that by convolving the image domain data with this filtering function, a new response with much lower sidelobes is obtained. Thus, our objective is to find such a filtering function, $T(\tau)$, so that the filtered PSF, $P_T(\tau)$, given by

$$P_T(\tau) = P(\tau) \otimes T(\tau) \quad (3.6)$$

has much lower sidelobes than the original one.

It is easy to understand that, when viewed in spectral domain, this filtering operation is equivalent to shape the spectral data using a special window function which is the Fourier transform of the filter function $T(\tau)$. This is very similar to the sidelobe control by aperture apodization as in an optical imaging system. Thus, we call the present image domain processing technique as apodization filtering.

3.3.3 Filter Coefficients Solution

The digitized version of Eq.(3.6) is a set of linear equations and can be written in matrix form as

$$\mathbf{A}\mathbf{F} = \mathbf{G} \quad (3.7)$$

where

$$\mathbf{A} = \begin{bmatrix} a_{11} & a_{12} & \cdots & a_{1N} \\ a_{21} & a_{22} & \cdots & a_{2N} \\ \cdots & & & \\ a_{M1} & a_{M2} & \cdots & a_{MN} \end{bmatrix},$$

$$\mathbf{F} = \begin{bmatrix} f_1 \\ f_2 \\ \cdots \\ f_N \end{bmatrix} \text{ and}$$

$$\mathbf{G} = \begin{bmatrix} g_1 \\ g_2 \\ \cdots \\ g_M \end{bmatrix},$$

$f_j = T((j-1)\Delta\tau)$ ($j = 1, 2, \dots, N$) are the coefficients of the filter to be obtained, $g_i = P_{Ti}((i-1)\Delta\tau)$ ($i = 1, 2, \dots, M$) are the samples of the desired PSF, and a_{ij} ($i = 1, 2, \dots, M, j = 1, 2, \dots, N$) are determined by $a_{ij} = P[(i-1+j)\Delta\tau]$, with $\Delta\tau$ being the time domain sampling interval, and $P(\tau)$ being the practical PSF of the radar system.

Given a practical radar system, it is always possible to obtain its true PSF, or a_{ij} ($i = 1, 2, \dots, M, j = 1, 2, \dots, N$) and other operational parameters. Therefore, the solution of the apodization filter coefficients, f_j ($j = 1, 2, \dots, N$) consists of three steps:

- (a). Determining the desired PSF, $g_i = P_{Ti}((i-1)\Delta\tau)$ ($i = 1, 2, \dots, M$);
- (b). Determining the filter length, N ; and
- (c). Applying iterative algorithm to find the filter coefficients f_j ($j = 1, 2, \dots, N$).

The first two steps will be discussed in the following section by combining into detailed computational examples. In this section, we concentrate on how to find the filter coefficients.

The set of linear equations in Eq.(3.7) represents an ill-posed system which makes a direct solution practically inapplicable. We have to find a robust algorithm to solve Eq.(3.7). The projection method has been proved to be very effective, yet robust, for solving ill-posed problems [34, 35]. The major advantage of this method is that it always converges for any given parameters. We use this method to solve our problem.

The projection method can be best described from a geometrical point of view as follows [35]. We denote

$$\mathbf{A}_i = [a_{i1}, a_{i2}, \dots, a_{iN}] \cdot \quad (3.8)$$

Consider \mathbf{F} as a point in an N -dimensional space. Each equation $\mathbf{A}_i \mathbf{F} = g_i$ ($i = 1, 2, \dots, M$) represents a hyperplane. Let the initial guess solution of \mathbf{F} be $\mathbf{F}^{(0)} = [f_1^{(0)}, f_2^{(0)}, \dots, f_N^{(0)}]$. Then the next solution $\mathbf{F}^{(1)}$ is the projection of the point $\mathbf{F}^{(0)}$ on the hyperplane $\mathbf{A}_1 \mathbf{F} = g_1$, that is

$$\mathbf{F}^{(1)} = \mathbf{F}^{(0)} - \frac{\mathbf{F}^{(0)} \cdot \mathbf{A}_1 - g_1}{\mathbf{A}_1 \cdot \mathbf{A}_1} \mathbf{A}_1 \quad (3.9)$$

where \cdot denotes the usual dot product. Then we take the projection of $\mathbf{F}^{(1)}$ on the hyperplane $\mathbf{A}_2 \mathbf{F} = g_2$, and successively obtain $\mathbf{F}^{(2)}$, $\mathbf{F}^{(3)}$, ..., until we get $\mathbf{F}^{(M)}$ which satisfies the last equation $\mathbf{A}_M \mathbf{F} = g_M$. At this point, we complete the first cycle of iterations. We then start from the first equation in Eq.(3.7) again: take the projection of $\mathbf{F}^{(M)}$ on $\mathbf{A}_1 \mathbf{F} = g_1$, call it $\mathbf{F}^{(M+1)}$, ..., until we obtain $\mathbf{F}^{(2M)}$, thus we complete the second cycle of iterations.

It can be shown [34] that if we continue our iteration in this manner, the vector sequence $\mathbf{F}^{(0)}, \mathbf{F}^{(M)}, \mathbf{F}^{(2M)}, \dots$, always converges for any given M, N and A_{ij} , i.e.,

$$\lim_{k \rightarrow \infty} \mathbf{F}^{(kM)} = \mathbf{F}. \quad (3.10)$$

If Eqs.(3.7) have a unique solution, \mathbf{F} is equal to that solution; and if Eqs.(3.7) have infinitely many solutions, \mathbf{F} is the solution that minimizes the norm $\|\mathbf{F} - \mathbf{F}^{(0)}\|^2$. Therefore, in the latter case, we can expect to obtain an optimal solution if we start with a good initial guess $\mathbf{F}^{(0)}$.

3.4 Computational and Experimental Results

In this section, we present some examples of image enhancement by a combination of apodization and median filtering. It is seen that median filtering serves to improve and smooth the uncharacteristic mainlobe of the PSF. When 1-D range profiles are to be processed, a 3-point median filter is applied. When 2-D images are to be processed, a 2-D 3×3 median filter is used. In all the cases, the noise radar parameters are selected to be the same as the 1-2 GHz UWB random noise radar built at University of Nebraska-Lincoln [10], i.e., central frequency $f_0 = 1.5$ GHz, bandwidth $B = 1.0$ GHz, and the sampling time interval $\Delta\tau = 0.156$ ns.

3.4.1 Computational Results

For practical applications, the desired PSF is usually expected to have a mainlobe similar to that of the *sinc* function while the sidelobe being zero. However, in the process of finding the filter coefficients by projection method, it is found that, with such a desired PSF, the iterative algorithm hardly converges to a desired solution. To overcome this problem, the desired PSF is selected as follows: determine a desired mainlobe width, set the amplitude of all the sidelobe points to be 0, set the amplitude of the central point of the mainlobe to be 1, and leave the amplitude of the mainlobe other than the central point to be unconstrained. It is seen that the number of the unconstrained points essentially determine

To see how the choice of the mainlobe width and the filter length impacts on the sidelobe suppression performance, we use the integrated sidelobe ratio (ISLR) and the peak sidelobe level (PSL) of the PSF as the metrics of the imaging performance. ISLR is defined as the ratio of the total sidelobe energy to the mainlobe energy of the PSF. PSL is defined as the maximum level among all the sidelobe peaks of the PSF. We study the ISLR and PSL as the functions of filter length and the mainlobe width normalized by the nominal down range resolution of the radar system. The nominal down range resolution $d = \frac{1}{2B}$, where B is the radar bandwidth. For example, for the current radar parameters, the nominal resolution is $d=1$ ns and occupies 6.41 points when the sampling time interval $\Delta\tau = 0.156$ ns.

A computational example for sidelobe reduction by a combination of apodization and median filtering is demonstrated in Figure 3.1. In this example, the normalized mainlobe

width is 2, and the normalized filter length is 14. The initial values of the filtering coefficients are selected all to be 1. Figure 3.1(a) shows the PSF before apodization filtering; Figure 3.1(b) shows the PSF after apodization filtering. As a comparison, we also provide with the PSFs after median filtering in Figure 3.1(c), and after apodization and median filtering in Figure 3.1(d). This example shows that, after apodization filtering together with median filtering, there is a great suppression of the range sidelobes, and an essential improvement of the uncharacteristic mainlobe of the original PSF.

Figure 3.2 demonstrates the reduction in the PSL and ISLR as the functions of the normalized filter length, with a fixed normalized mainlobe width 2. As the normalized filter length varies from 2 to 20, the corresponding PSL decreases from about -21 dB to -43 dB, and the ISLR decreases from -18 dB to -30 dB.

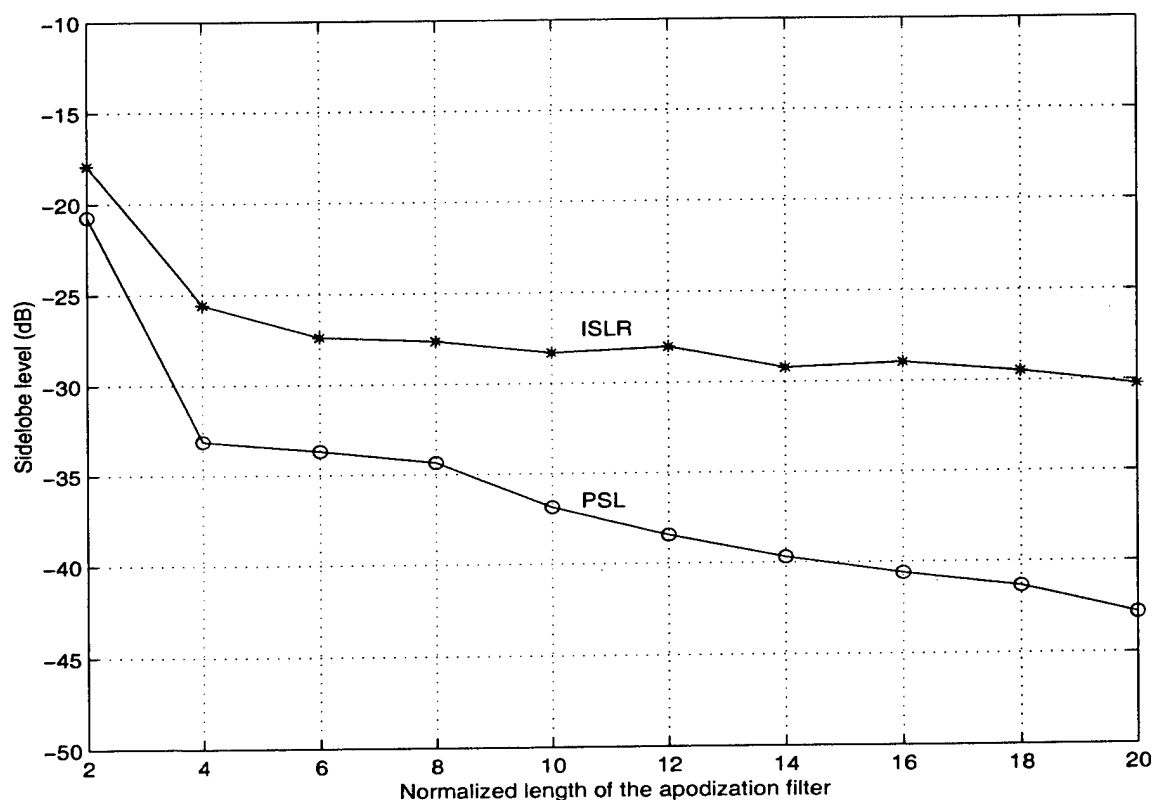


Figure 3.2: PSL and ISLR as functions of the normalized filter length.

In Figure 3.3, the PSL and ISLR as the functions of the normalized mainlobe width of the desired PSF is illustrated. Here the normalized filter length is 14. With the normalized mainlobe width changing from 0.94 to 2.96, the corresponding PSL decreases from -23 dB to -54 dB, while the ISLR decreases from -14 dB to -46 dB.

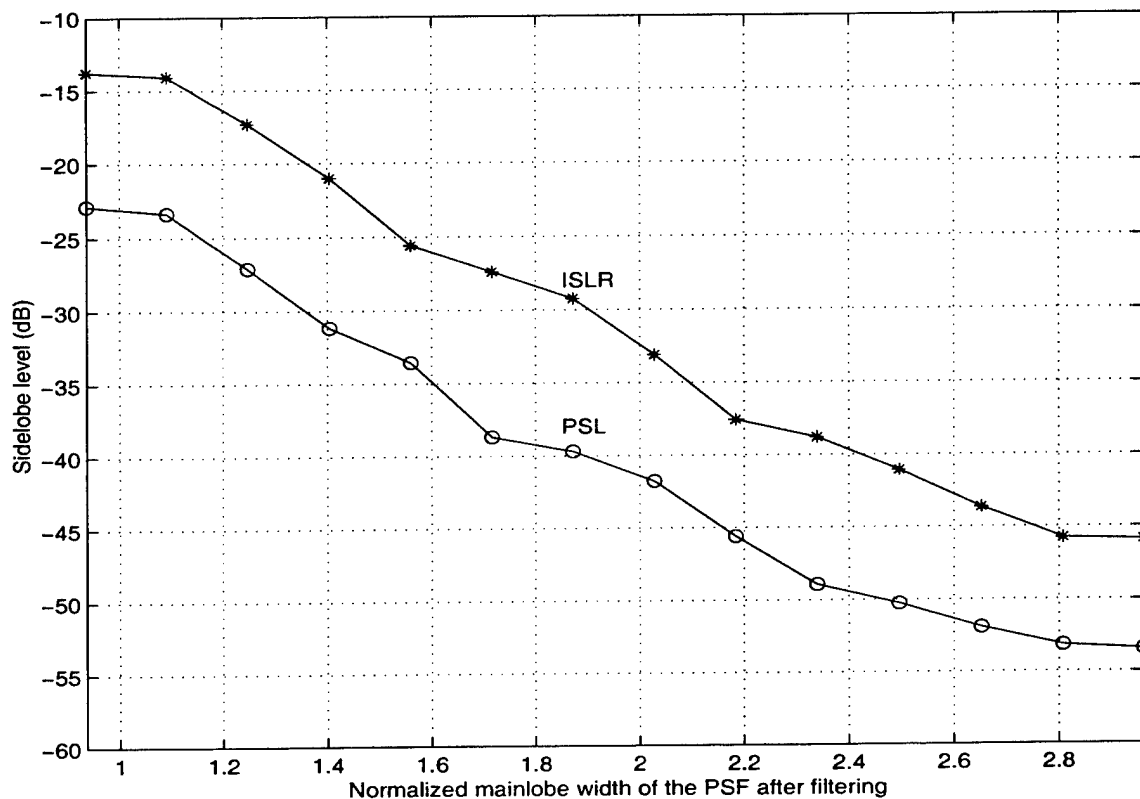


Figure 3.3: PSL and ISLR as functions of the normalized mainlobe width.

As it is expected, the reduction of the sidelobe level is at the cost of increasing either the mainlobe width or the filter length. For practical applications, it is possible to trade-off between the mainlobe width, the filter length and the sidelobe level.

3.4.2 Application to Ground Penetration Noise Radar Data

The apodization filtering technique was also applied to the polarimetric processing of the 1-2 GHz ground penetration noise radar data for image enhancement. We present one of the examples here. The interested reader can find more details in [21].

Figure 3.4 illustrates the real PSFs of the coherent UWB random noise radar system before and after apodization filtering, where: (a) is the PSF before apodization filtering; (b) is the PSF after median filtering; (c) is the PSF after apodization filtering; and (d) is the PSF after apodization and median filtering. It can be seen that, by using an apodization filter with normalized filter length of 10 and normalized mainlobe width 1.56, there is a sidelobe level improvement of about 10 dB compared to the original PSF.

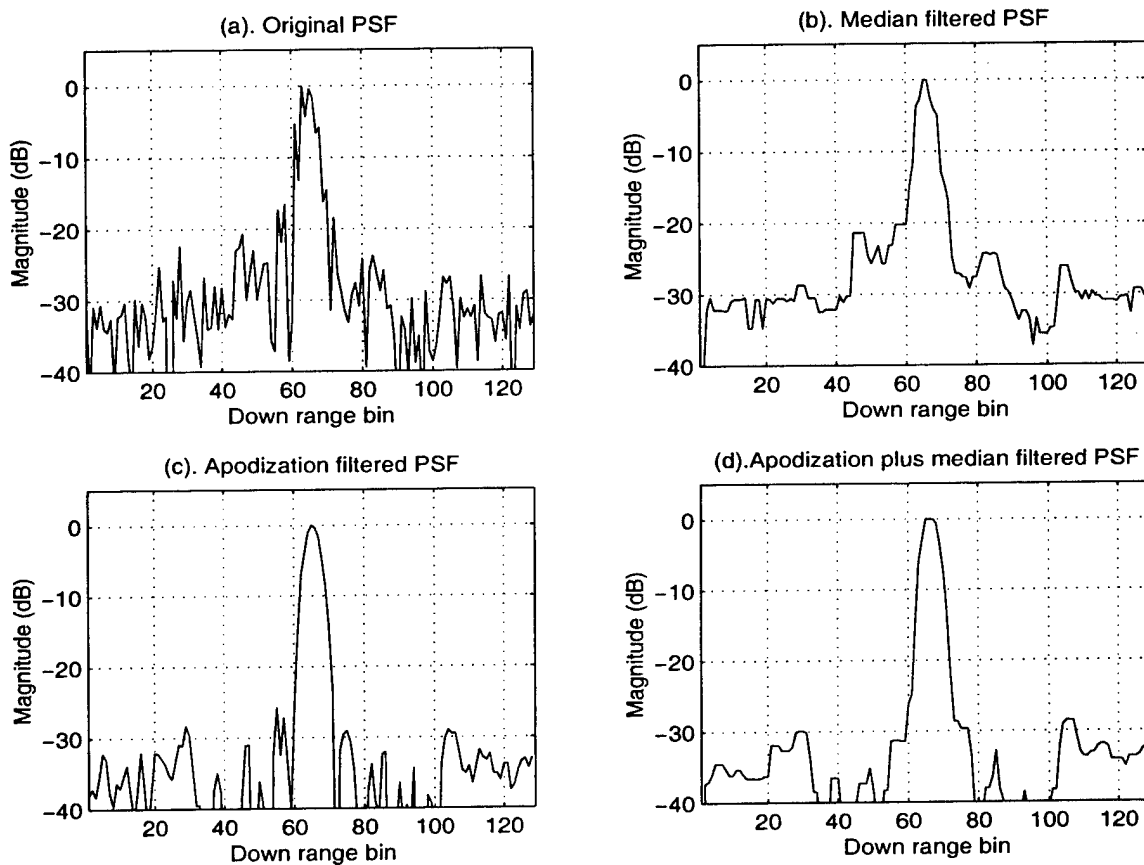


Figure 3.4: True PSFs of the ground penetration noise radar before and after filtering.

Figure 3.5 demonstrates an example for the application of the apodization filtering to 2-D image processing of the ground penetration random noise radar. In Figure 3.5, the objects to be detected are two metal plates, one round and the other square, buried in dry soil at depths of 17.8 cm and 43.2 cm, respectively, with a horizontal separation of 25.4

cm. This figure shows the co-polarization images, where (a) is the original image; (b) is the median filtered image; (c) is the apodization filtered image; and (d) is the apodization and median filtered image. It is obvious that a much better target-to-background contrast is obtained after combined apodization and median filtering of the raw image.

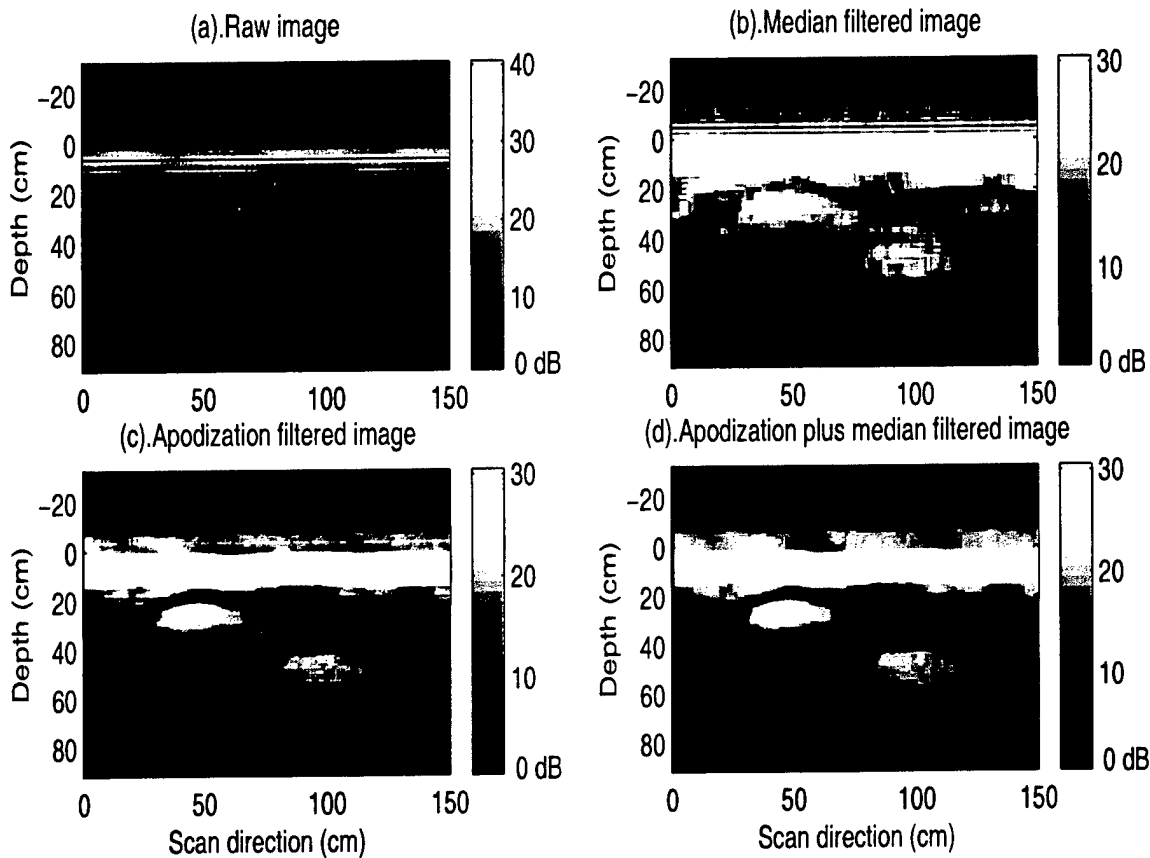


Figure 3.5: Comparison of ground penetration radar images before and after filtering processing.

3.5 Summary

A linear image domain apodization filtering technique is introduced which, when combined with median filtering, suppresses the down range sidelobes effectively in UWB random noise radar imagery. Sidelobe reductions of greater than 20 dB are possible using this technique.

The method is adaptable to practical radar systems and is applicable for real-time image processing. The potential applications of this technique exist where the PSFs of the imaging systems are known. Note that the present procedure is an approximate filtering method. The limitation is that the sidelobe envelope of the PSF to decrease rapidly. When the sidelobe decreases too slowly, the length of the apodization filter may become too long to be realistic.

Chapter 4

IMPACT OF FOLIAGE OBSCURATION ON SAR IMAGES

4.1 Background

The detection and identification of targets that are obscured by foliage are topics of great current interest. Several experimental developments of such ultra-wideband (UWB) radars have been reported. By operating at the VHF and UHF frequency bands and using either LFM or step-frequency waveforms, these radars have demonstrated promising images of terrain and man-made objects obscured by dense foliage [36] - [42].

As is known, when using a SAR to image targets under dense foliage, the foliage obscures the target images in three major ways [2]:

- (a) The foliage attenuates the energy both incident to and scattered from the target, resulting in a lower signal to noise ratio;
- (b) The foliage forms strong backscatter clutter, reducing the target-to-background contrast in the image; and
- (c) The amplitude and phase fluctuation of the foliage distorts the SAR images of the target.

The first and the second issues relate to the mean attenuation and the backscatter, respectively, while the third relates to the amplitude and phase fluctuations of the foliage.

Radar backscatter from forest and vegetation canopy has been the subject of intensive

study in the past two decades. Various electromagnetic scattering models of forest have been proposed. Based on the theory of electromagnetic wave scattering in random media, these models typically calculate the backscatter coefficients and/or the average attenuation, according to the geometry and biophysical properties of forest components and the radar operation and observation parameters. Some typical models include the Michigan microwave canopy scattering model (MIMICS) [45, 46], the models developed at the Wave Scattering Research Center (WSRC) of UTA [47, 48], etc. (e.g., [49, 50]).

Recent advancements in foliage penetration SAR imaging have opened new insights into this problem. It is believed that the amplitude and phase fluctuations have the most severe impact on the FOPEN SAR images, as these fluctuations destroy the coherence of the signals, thereby obscuring the target images in a very complicated way. As a consequence, a better understanding of the coherent interaction of electromagnetic wave with the forest is required. Many experimental as well as theoretical studies for this purpose have been conducted by a number of researchers in recent years.

In an experimental study, Sheen *et al.* [3] constructed a ground-based UWB SAR system and measured the backscatter and transmission characteristics of typical foliage. A linear model was proposed to describe the observations of foliage mean attenuation, SAR resolution broadening, and the integrated sidelobe ratio (ISLR) of the synthetic pattern as a function of frequency, depression angle, and forest biomass, for both HH and VV polarizations. The research groups from USAFRL [4], MIT [1, 40, 2, 51], and JPL [52, 53] have reported the results of several foliage penetration experiments, using the NASA/JPL UHF, L and C band fully polarimetric SAR imaging over forested areas. These results include the observed foliage transmission and backscatter statistics, the measurement-fitted two-way mean attenuation model, analysis of the foliage-induced synthetic pattern distortion, and so on.

Some theoretical and simulation studies have also been published [54, 55, 56]. Hsu *et al.* [54] developed a theoretical model to calculate the mean foliage attenuation as well as the amplitude and phase fluctuations. In this model, the mean attenuation is obtained from the sum of absorption and scattering losses, the amplitude fluctuation is calculated from the bistatic scattering coefficients using the radiative transfer theory, while the phase fluctuation is obtained from the amplitude fluctuation assuming the phase of the fluctuating field has an

uniform density over $[-\pi, \pi]$. More recently, Sarabandi and Lin [55, 56] developed a coherent scattering model for tree canopy based on a Monte Carlo simulation of scattering from fractal-generated tree structures. This model is capable of preserving the absolute phase of the backscatter as well as accounts for coherent effects due to the inhomogeneous extinction experienced by a coherent wave propagating through the random collection of foliage components, and thus has the potential to simulate the amplitude and phase fluctuation characteristics of foliage.

Past work on radar penetration imaging had mainly focused on UWB LFM and step-frequency waveforms, although some comparative results were obtained by Walton *et al.* [43, 44], among an impulse radar, a noise radar and a step-frequency radar, for the case of concrete wall penetration. In this chapter, a comparative study of the radar images using step-frequency and random noise waveforms helps demonstrate the suitability of the UHF band UWB random noise radar for foliage penetration (FOPEN) surveillance applications. The objectives of the present work include:

- (a) Development of a statistical-physical model to simplify the simulation for foliage transmission characteristics, based on the experimental observations and foliage scattering and absorption phenomenologies;
- (b) Analysis of the foliage obscuring pattern to better understand the foliage-induced SAR image distortion by means of the technique of paired echoes; and
- (c) Demonstration of the feasibility of the coherent random noise radar for foliage penetration surveillance applications, through a comparative study of the FOPEN SAR imaging using ultra-wideband step-frequency and random noise radar waveforms.

The remainder of this chapter is organized as follows. Section 4.2 describes a simplified FOPEN SAR imaging system model. In section 4.3, a statistical-physical model for foliage transmission is developed. This is followed by section 4.4 in which a detailed analysis of the foliage obscuring pattern in FOPEN SAR images is presented. In section 4.5, the simulation results for a comparative study of FOPEN SAR imaging using ultra-wideband step-frequency and random noise radar waveforms are presented. We summarize the chapter in section 4.6.

4.2 FOPEN Radar Imaging System Model

To simplify the radar imaging signal model, we consider the spotlight mode SAR imaging geometry in Figure 4.1. The radar-carrying aircraft flies along a circular arc path at a constant height of h_0 . The slant distance between the radar and the center of the spotlighted target area is R_0 , and the radius of the target area is L . The two-dimensional scattering function of the target area is denoted by $g(x, y)$.

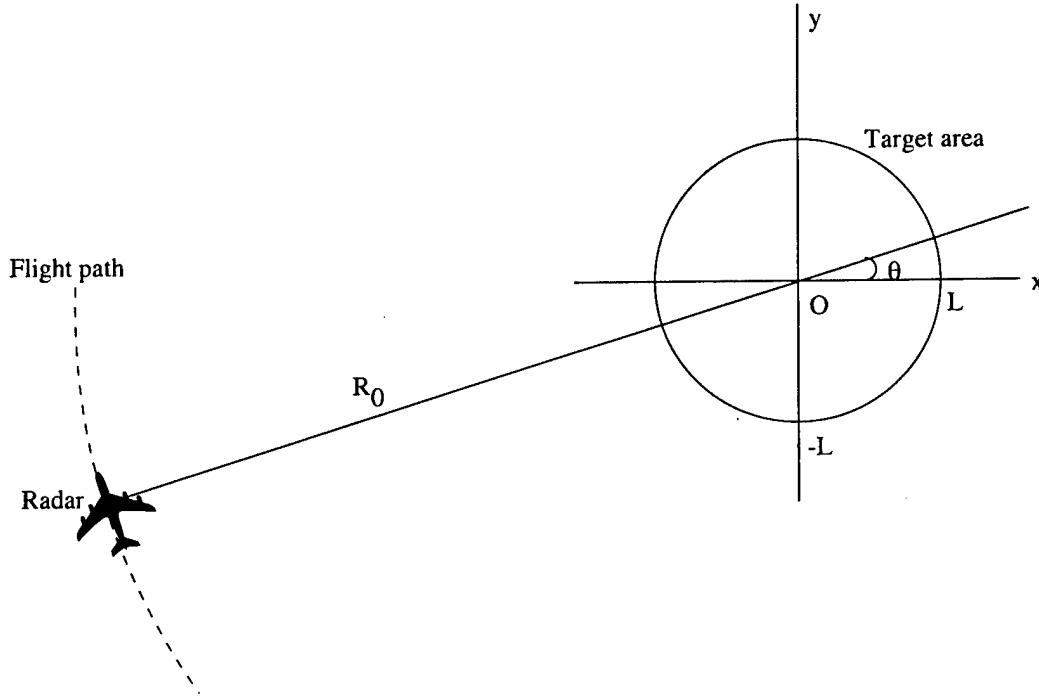


Figure 4.1: Spotlight mode SAR imaging geometry.

When the radar transmits a series of signals $s(t)$ at different flight path position (or azimuthal angle) θ , the corresponding received target returns can be expressed as

$$g_s(t, \theta) = \int_{-L}^L \int_{-L}^L g(x, y) s\left[t - \frac{2R(x, y, \theta)}{c}\right] dx dy \quad (4.1)$$

where c is the speed of light, and

$$R(x, y, \theta) = \sqrt{(x - R_0 \cos \gamma \cos \theta)^2 + (y - R_0 \cos \gamma \sin \theta)^2 + h_0^2} \quad (4.2)$$

where

$$\gamma = \sin^{-1} \frac{h_0}{R_0} \quad (4.3)$$

is the radar depression angle.

The Fourier transform of the signal $g_s(t, \theta)$ with respect to time, t , is

$$G_s(\omega, \theta) = S(\omega) \int_{-L}^L \int_{-L}^L g(x, y) \exp[-j \frac{2\omega}{c} R(x, y, \theta)] dx dy = S(\omega) G(\omega, \theta), \quad (4.4)$$

where $S(\omega)$ is the Fourier transform of the signal $s(t)$, and

$$G(\omega, \theta) = \int_{-L}^L \int_{-L}^L g(x, y) \exp[-j \frac{2\omega}{c} R(x, y, \theta)] dx dy. \quad (4.5)$$

Eqs. (4.1) and (4.4) are the general signal model for spotlight mode SAR imaging without consideration of the foliage transmission characteristics. For FOPEN SAR imaging, it is necessary to include the effects of the foliage obscuration on the transmitted and received signals. In the frequency domain, this FOPEN radar imaging system model can be simplified as shown in Figure 4.2, where we denote foliage propagation characteristics for the transmitted signal and the target scattered signal as $F_T(\omega, \theta)$ and $F_R(\omega, \theta)$, respectively, and the received foliage obscured signal as $G_F(\omega, \theta)$. The Fourier transform of the received foliage obscured target signature can then be expressed as

$$G_F(\omega, \theta) = S(\omega) F_T(\omega, \theta) G(\omega, \theta) F_R(\omega, \theta) = G_s(\omega, \theta) F(\omega, \theta) \quad (4.6)$$

where

$$F(\omega, \theta) = F_T(\omega, \theta) F_R(\omega, \theta) \quad (4.7)$$

represents the frequency and azimuth dependent two-way foliage transmission at specific radar polarization and depression angle.

4.3 Foliage Transmission Modeling

In this section, we develop a statistical-physical model to simplify the simulation of the foliage transmission characteristics. The model is based on the experimental observations

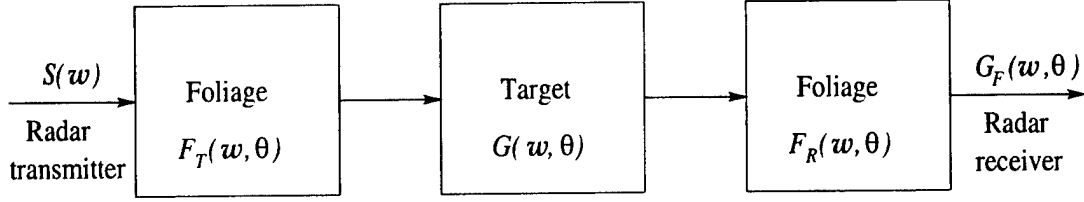


Figure 4.2: System model for FOPEN radar imaging.

and theoretical studies by researchers at USAFRL [4], MIT [1, 2, 51, 54] and ERIM [3].

4.3.1 Proposed statistical-physical model

From the viewpoint of a nonlinear system, the impact of foliage transmission on the transmitted and the target scattered signals can be represented by a system transfer function. Typically, this transfer function has both nonlinear amplitude characteristics and nonlinear phase characteristics. At a specific radar polarization, this transfer function can be expressed as

$$F(\omega, \theta, \gamma) = A(\omega, \theta, \gamma) \exp[j\Phi(\omega, \theta, \gamma)] \quad (4.8)$$

where $A(\omega, \theta, \gamma)$ and $\Phi(\omega, \theta, \gamma)$ represent the nonlinear amplitude characteristics and phase characteristics of the foliage transmission, respectively. Both A and Φ are functions of the radar frequency ω , the flight path θ , and radar depression angle γ .

The amplitude characteristics can be considered to be composed of two components: the mean attenuation and the amplitude fluctuation, and can be expressed as

$$A(\omega, \theta, \gamma) = A_0(\omega, \gamma)[1 + \delta_A(\omega, \theta, \gamma)] \quad (4.9)$$

where $A_0(\omega, \gamma)$ and $\delta_A(\omega, \theta, \gamma)$ are the mean attenuation and the normalized amplitude fluctuation, respectively.

Similarly, the phase characteristics can also be considered to consist of two components: the linear phase and the phase fluctuation, i.e.

$$\Phi(\omega, \theta, \gamma) = -P_0\omega + \delta_\Phi(\omega, \theta, \gamma) \quad (4.10)$$

where $P_0\omega$ is the linear phase term, and $\delta_\Phi(\omega, \theta, \gamma)$ represents the phase fluctuation. The negative sign before the linear phase term implies that there is a mean time delay after the wideband electromagnetic wave propagates through the foliage.

The model in Eqs. (4.8)-(4.10) reflects the following foliage transmission characteristics: the mean attenuation, the mean propagation delay, the amplitude fluctuation and the phase fluctuation. To make the foliage transmission model applicable for foliage transmission simulation, we need to relate the model parameters to the geometry and biophysical properties of the forest as well as to the statistics of the measured data for specific forest truth.

Mean attenuation

Following Davis [4], the mean amplitude attenuation of the foliage can be expressed as

$$A_0(\omega, \gamma) = \beta f^\alpha (\sin 45^\circ / \sin \gamma) \quad (4.11)$$

where A_0 is in dB, $f = \frac{\omega}{2\pi}$ is the radar frequency in MHz, γ is the depression angle, and α and β are two constants. The values of α and β can be determined through model-fitting to the measured data for specific forest conditions.

Amplitude fluctuation

The normalized amplitude fluctuation, $\delta_A(\omega, \theta, \gamma)$, can be expressed as

$$\delta_A(\omega, \theta, \gamma) = \delta_\omega(\omega, \gamma) \delta_\theta(\theta) \quad (4.12)$$

where $\delta_\omega(\omega, \gamma)$ and $\delta_\theta(\theta)$ represent the frequency and depression angle dependent, and flight path dependent amplitude fluctuations, respectively.

The frequency and depression angle dependent amplitude fluctuation, $\delta_\omega(\omega, \gamma)$, is modeled by a random process, such that the random variable

$$x = A_0(\omega, \gamma)[1 + \delta_\omega(\omega, \gamma)]$$

has Log-Gamma probability density, i.e., when the random variable x is expressed in dB, it has a Gamma density, given by

$$p(x, a, b) = \frac{1}{b^a \Gamma(a)} x^{a-1} e^{-x/b} \quad (4.13)$$

where a and b are two constants to be determined. Note that the mean and variance of the Gamma distribution are $\mu = ab$ and $\sigma^2 = ab^2$, respectively. These two parameters a and b can then be determined by the mean attenuation and the variance statistics of the measured amplitude fluctuation.

The rationale for selecting the Log-Gamma density can be made as follows: from the optical theorem, the total attenuation can be related to the extinction cross-section σ_e by an exponential function, where the extinction cross-section σ_e is proportional to the imaginary part of the forward scattering amplitude. The foliage is considered to be a sparse multi-layer random medium with each layer consisting of different types of scattering components. The scattering resulting from the interaction of the electromagnetic waves with each layer can be considered to have Rayleigh density, since the Rayleigh probability distribution is the result of the noncoherent scattering from a reasonable number of scatterers approximately equal in size, whose scattering phases are randomly distributed [57]. The total scattering of the multi-layer foliage can then be considered to have a Gamma density [58]. Thus, the total amplitude attenuation statistics can be modeled by a random variable having Log-Gamma density.

The flight path dependent amplitude fluctuation $\delta_\theta(\theta)$ is modeled as

$$\delta_\theta(\theta) = \exp[\eta_H(\Delta\theta)] \quad (4.14)$$

where $\eta_H(\Delta\theta)$ is a fractional Brownian motion (fBm) process. An fBm is a two-parameter random process. The first is the Hurst exponent H ; $H \simeq 0.4$ for vegetation cover [59]. The second is $\Delta\theta$, which is related to the synthetic aperture size or the flight path length.

The idea for utilizing an fBm process in Eq. (4.14) is borrowed from the scattering model of dielectric random fractal surfaces [60], and is based on the following assumption: the flight path dependent amplitude fluctuation can be considered to be the result of the variation of the equivalent foliage propagation path length, which is directly related to the integration of the forest truth over the beamwidth of the radar antenna. An fBm process has been proven

to represent one-dimensional (1-D) profiles of natural surfaces very well, thus is reasonable to use it to model the variation of such an equivalent propagation path length.

Phase characteristics

The parameter P_0 in the linear phase term in Eq. (4.10) represents the mean propagation delay, and is related to the average propagation path length and the equivalent dielectric constant of the foliage. It is easy to understand that, from the viewpoint of SAR imaging, this linear phase merely produces a linear shift of the overall image, as will be shown in the next section. Therefore, the choice of P_0 is immaterial.

According to [54], the phase fluctuation characteristics can be derived from the amplitude fluctuation, by assuming that the phase of the incoherent field is uniformly distributed from $-\pi$ to π , i.e. using

$$\delta_\Phi(\omega, \theta, \gamma) = \tan^{-1} \left[\frac{\delta_A(\omega, \theta, \gamma) \sin \psi}{1 + \delta_A(\omega, \theta, \gamma) \cos \psi} \right] \quad (4.15)$$

where ψ has an uniform density over $[-\pi, \pi]$.

4.3.2 Validation of the foliage transmission model

To ensure that the model is suitable for foliage transmission simulation applications, a number of model validation experiments were conducted. Some typical results are illustrated in Figure 4.3 and Figure 4.4.

Figure 4.3 shows the cumulative probability distribution of the two-way attenuation fluctuation generated by the model, with comparisons to the foliage penetration experiment data published in [1, 4]. In this example, the radar central frequency is 440 MHz, and the bandwidth 38 MHz. For the measured data statistics, the parameters for the mean attenuation were given as follows: For HH polarization, the median attenuation corresponds to $\alpha = 0.79$ and $\beta = 0.044$, and the 90 percentile attenuation corresponds to $\alpha = 0.79$ and $\beta = 0.077$; for VV polarization, the median attenuation corresponds to $\alpha = 0.427$ and $\beta = 0.61$, and the 90 percentile attenuation corresponds to $\alpha = 0.61$ and $\beta = 0.36$. For the model simulated statistics, for HH polarization, we take $\alpha = 0.79$, $\beta = 0.05$; and for

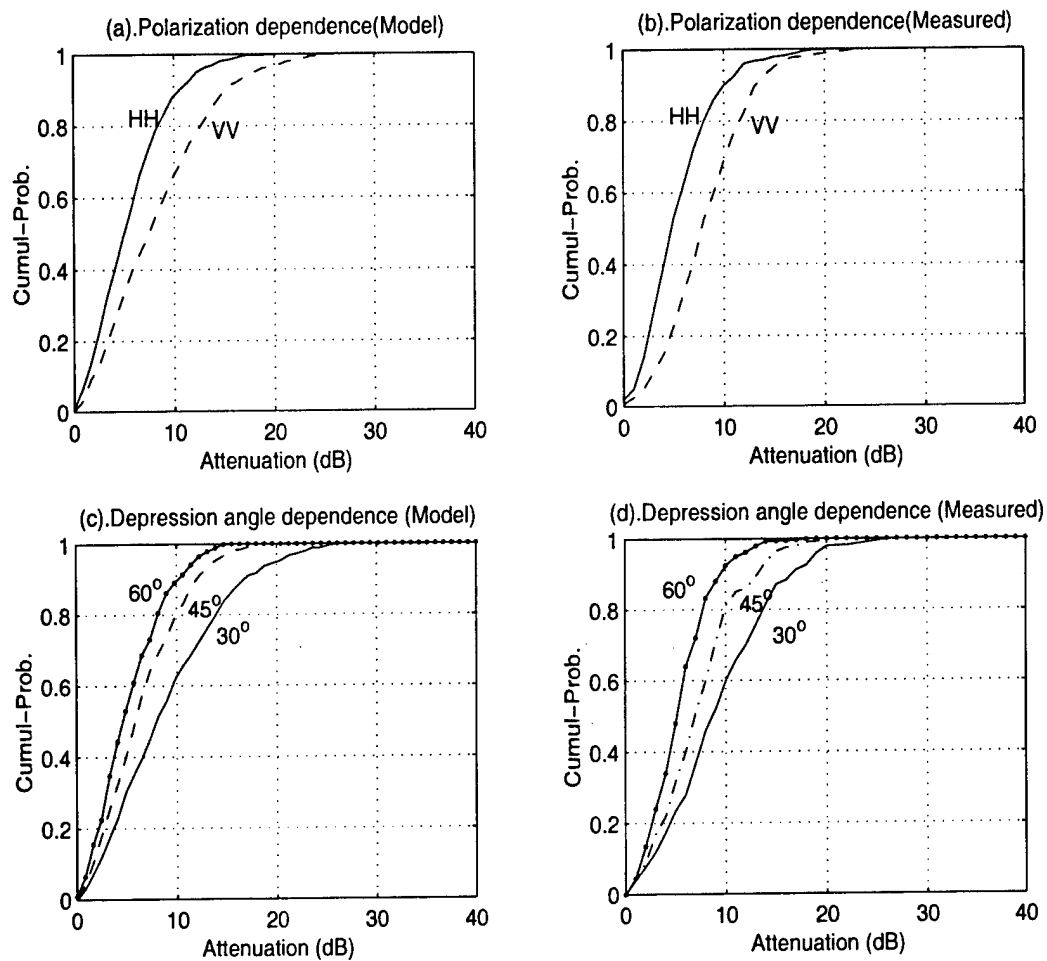


Figure 4.3: Comparison of the cumulative probability distributions.

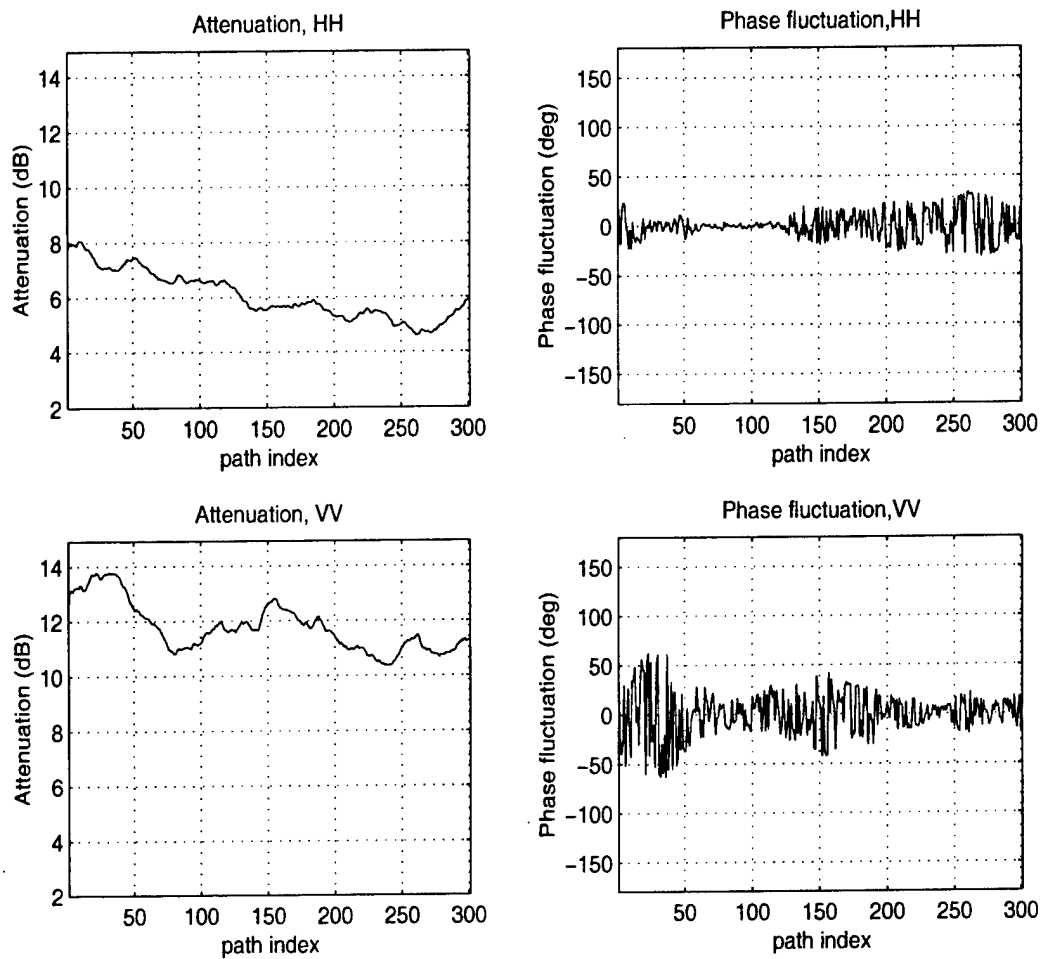


Figure 4.4: Simulated amplitude and phase fluctuation vs. flight path.

VV polarization, $\alpha = 0.5$, $\beta = 0.45$. In both cases, the parameters correspond to the mean attenuation. As clearly observed from Figure 4.3, our model results show good consistency with the experimental measurement statistics.

Figure 4.4 demonstrates the simulated flight path dependent amplitude fluctuations and the corresponding phase fluctuations for both HH and VV polarizations at specific radar frequency and depression angle. We find that the trends are coincident with published experimental observations [2, 3].

In summary, the usefulness of the above statistical-physical foliage transmission model lies in the fact that it not only considers the frequency, polarization, depression angle and flight path dependent characteristics, but also reflects almost all the major observations of foliage transmission experiments [1, 2, 3, 51, 52, 54], such as

- (a) Both the mean attenuation, and the amplitude and phase fluctuations increase as the radar operates at a higher frequency band;
- (b) The amplitude characteristics shows rapid fluctuation as a function of radar frequency, and shows slow fluctuation as a function of flight path;
- (c) The phase fluctuation depends more on the amplitude fluctuation than on the mean attenuation, and it tends to increase as the mean attenuation increases, as the variance of amplitude fluctuation is proportional to the mean attenuation;
- (d) For both amplitude and phase fluctuations, the correlation lengths decrease as the variances of fluctuations increase; and so on.

4.4 Foliage Obscuration Pattern Analysis

A FOPEN SAR usually acquires the target signature as a function of frequency and flight path (or azimuthal angle) at specific depression angle and radar polarization. By coherent processing of the acquired data, the two-dimensional images are formed. For simplicity and without loss of generality, in the following we mainly concentrate on the analysis of the distortion pattern resulting from the frequency-dependent foliage obscuration. Extension of our conclusions to the flight path dependent foliage obscuration is straightforward.

At a fixed azimuthal angle, depression angle and specific radar polarization, the fo-

liage transmission characteristics is a function of the radar angular frequency, ω . From Eqs. (4.8)-(4.10), the amplitude and phase characteristics of the foliage transmission can then be simplified as

$$A(\omega) = A_0(\omega)[1 + \delta_A(\omega)] \quad (4.16)$$

and

$$\Phi(\omega) = -P_0\omega + \delta_\Phi(\omega) \quad (4.17)$$

respectively. The amplitude characteristics $A(\omega)$ and phase characteristics $\Phi(\omega)$ can be expanded in a Fourier series representation, i.e.

$$A(\omega) = a_0 + \sum_{n=1}^{\infty} a_n \cos(nc_0\omega + \alpha_n), \quad (4.18)$$

$$\Phi(\omega) = -b_0\omega + \sum_{m=1}^{\infty} b_m \sin(mc_0\omega + \beta_m), \quad (4.19)$$

where the two summation terms represent the amplitude and phase fluctuation, respectively, $a_n, \alpha_n, b_m, \beta_m$ and c_0 are constants. Note that c_0 has unit of time, and is given by $c_0 = \frac{2\pi}{\Delta\omega}$, where $\Delta\omega$ is the UWB system bandwidth. The above representation assumes that $A(\omega)$ and $\Phi(\omega)$ are periodic in ω , with period $\Delta\omega$. While this is not strictly valid, it simplifies the analysis as long as our results are not extended outside the intended frequency range. The frequency-dependent foliage transmission function, $F(\omega)$, can then be rewritten as

$$F(\omega) = F_0(\omega) \prod_{m=1}^{\infty} F_m(\omega) \quad (4.20)$$

where

$$F_0(\omega) = e^{-jb_0\omega} [a_0 + \sum_{n=1}^{\infty} a_n \cos(nc_0\omega + \alpha_n)] \quad (4.21)$$

and

$$F_m(\omega) = \sum_{k=-\infty}^{\infty} J_k(b_m) \exp[jk(mc_0\omega + \beta_m)] \quad (4.22)$$

Correspondingly, from Eq. (4.6) the foliage obscured frequency dependent target signature can be simplified as

$$G_F(\omega) = G_s(\omega)F_0(\omega) \prod_{m=1}^{\infty} F_m(\omega) \quad (4.23)$$

where $G_s(\omega)$ is the unobscured target signature.

Eq. (4.23) states that the foliage obscured signature can be considered to be the output of a nonlinear system, where the input of the system is the unobscured signature. The system itself is composed of infinite numbers of subsystems connected in series. The first subsystem, having the characteristics $F_0(\omega)$, includes the effect of the amplitude characteristics and the linear term of the phase characteristics. The following subsystems correspond to the components of the phase characteristics in the order of their amplitudes.

4.4.1 Distortion induced by amplitude fluctuations

The distortion induced by the amplitude fluctuations can be found by analyzing the output of the first subsystem having characteristics $F_0(\omega)$. In the image domain (time domain), this output can be expressed as

$$g_0(t) = a_0 g_s(t - b_0) + \frac{1}{2} \sum_{n=1}^{\infty} a_n [g_s(t - b_0 - nc_0)e^{-j\alpha_n} + g_s(t - b_0 + nc_0)e^{j\alpha_n}] \quad (4.24)$$

which is a sum of the weighted and time-delayed version of the same echoes as the unobscured target signature. This follows from the theory of paired echoes.

According to the theory of paired echoes [61, 62], the image domain output consists of three terms: the first term is the principal component, which has the weighting constant a_0 , basically representing the average attenuation of the foliage transmission, and the time-delay constant b_0 , basically representing the linear phase term of the foliage phase characteristics; the second and third terms represent the summations of various leading echoes and lagging echoes resulting from the nonlinearity of the subsystem, with the weighting coefficients being determined by the amplitude fluctuation characteristics.

4.4.2 Distortion induced by phase fluctuations

The impact of the phase fluctuations on the image is determined by all the subsystems having transfer function $F_m(\omega)$, $m = 1, 2, \dots$. The distortion pattern can be analyzed as follows.

When the amplitude-distorted signal $g_0(t)$ is input to the next subsystem having the characteristics $F_1(\omega)$, the output is

$$g_1(t) = J_0(b_1)g_0(t) + \sum_{k=1}^{\infty} [J_{-k}(b_1)g_0(t - kc_0)e^{-jk\beta_1} + J_k(b_1)g_0(t + kc_0)e^{jk\beta_1}]. \quad (4.25)$$

In this way, the above process can be repeated until all of the b_m 's are considered. At the m th subsystem, the output can be expressed in terms of the output of the $(m - 1)$ th subsystem, $g_{m-1}(t)$, given by

$$g_m(t) = J_0(b_m)g_{m-1}(t) + \sum_{k=1}^{\infty} [J_{-k}(b_m)g_{m-1}(t - kmc_0)e^{-jk\beta_m} + J_k(b_m)g_{m-1}(t + kmc_0)e^{jk\beta_m}]. \quad (4.26)$$

For each subsystem, the output is a sum of the weighted and time delayed version of the same echoes as the input signal, with the weighting coefficients being determined by the constant b_m .

It is now easy to recognize that the distortion induced by phase fluctuation is much more complicated than that induced by the amplitude fluctuation. As a consequence, the impact of the phase fluctuation on SAR imaging is much more severe than the amplitude fluctuation. Fortunately, for FOPEN SAR applications, the radar usually operates at lower frequencies, such as at VHF and UHF bands. At these frequency bands, the standard deviation of the observed phase fluctuation is typically less than 30° (or about 0.5 radians), thus the coefficients b_m 's are typically small in quantity. Note that

$$J_k(b) = \frac{b^k}{2^k} \sum_{i=0}^{\infty} \frac{(-1)^i b^{2i}}{2^{2i} \Gamma(k + i + 1)}. \quad (4.27)$$

For small b 's, the effects of the higher order terms are typically negligible. Thus, the essential distortion induced by the phase fluctuation will mainly result from the first leading and the

first lagging echoes (corresponding to $k = 0$ and $k = \pm 1$) at the first several subsystems $F_m(\omega)$, ($m = 1, 2, \dots$).

From the above analysis, it is seen that the amplitude fluctuation leads to distortion resulting from the translational symmetrical positive paired echoes, while the phase fluctuation leads to distortion resulting from the translational skew-symmetrical negative paired echoes. As a result, the combination of the amplitude and phase fluctuations leads to increased sidelobes of the images; and the quantities of the coefficients of the Fourier series a_n 's and b_m 's in Eqs. (4.18) and (4.19) determine how severe will be the sidelobes. Note that both the amplitude fluctuation and the phase fluctuation can be considered to be random processes to some extent, a_n 's and b_m 's being directly proportional to the variances of the fluctuations. Therefore, the more fluctuations the amplitude and phase of the foliage show, the greater the integrated sidelobe level will be.

The conclusion about the 1-D distortion pattern can be directly extended to the 2-D SAR imaging case. As a consequence of the combined frequency dependent and flight path dependent foliage obscuration, the 2-D image of an ideal point target (or the 2-D point spread function (PSF)) will exhibit more artifacts over the entire 2-D imaging plane. However, the most severe impact will be the much higher sidelobes along the down range and cross range axes across the point target than the unobscured version, as will be further discussed in the following section.

4.5 Comparative Study of Step-Frequency and Random Noise SAR Using Simulation

Step-frequency waveform has been considered to be an ideal candidate for UWB FOPEN SAR applications. In this section, through a comparative study of FOPEN SAR imaging, using UWB step-frequency and random noise waveforms, we demonstrate the suitability of a coherent random noise radar to be also used as a FOPEN SAR.

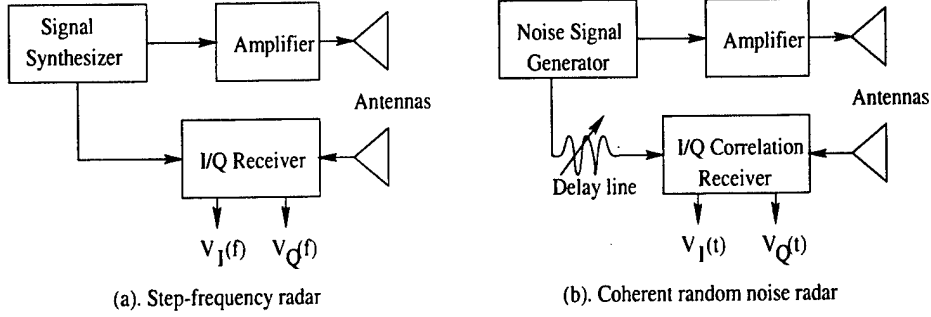


Figure 4.5: Simplified diagrams of the two radar systems.

4.5.1 Brief description of the two systems

Simplified system diagrams of the two kinds of radar systems are shown in Figure 4.5. The step-frequency radar transmits CW signal and measures the amplitude and phase of the backscattered signals. The frequency of the transmit waveform is stepped through a set of discrete frequencies over the operating bandwidth. The noise radar transmits a truly random noise signal within the desired frequency range and processes the target echoes by employing a heterodyne correlation receiver. Thus, both systems can obtain the I and Q signals of the scattering echoes. The major difference is that the step-frequency radar obtains the frequency-domain samples, while the noise radar obtains samples of the I and Q signals in time-domain.

The radar parameters for this study are selected the same as the UWB random noise FOPEN radar being built at UNL [63], i.e., the central frequency 375 MHz, bandwidth 250 MHz. The foliage model parameters are selected the same as described in Section 3. Note that in all the following examples, the backscatter clutter of the foliage was not considered, as this clutter is basically an additive noise, thus does not have an impact on the major aspects of our conclusions.

4.5.2 Comparison of the Ideal PSFs

We first compare the ideal point spread functions (PSFs) in down range for the two radar systems. In these simulations, in order to suppress the sidelobes of the PSFs for the step-frequency radar, a Hamming window is utilized, while for the random noise radar, an apodiza-

tion filter is applied, with both having maximum sidelobe levels of about -42 dB.

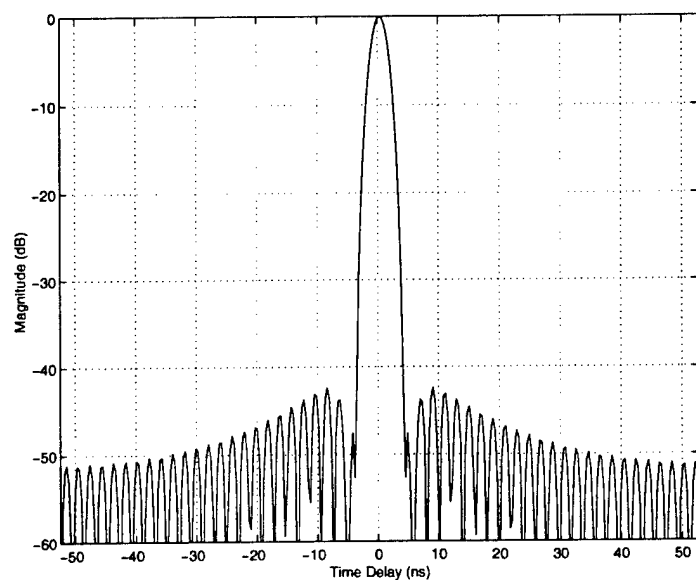
We use the integrated sidelobe ratio (ISLR) and the peak sidelobe level (PSL) of the PSF as the radar imaging performance measuring parameters. ISLR is defined as the ratio of the total sidelobe energy to the mainlobe energy of the PSF, where the mainlobe includes all energy contained within the first nulls of the PSF. PSL is defined as the maximum sidelobe level among all the sidelobe peaks of the PSF.

The ideal PSFs for the step-frequency and the random noise radar systems are shown in Figure 4.6(a) and (b), respectively. Note that for the random noise radar, due to the randomness of the waveform, in order to improve the uncharacteristic mainlobe and reduce sidelobe levels in the PSF, it is necessary to perform an integration of a series of target echoes at each range cell. In this example, the number of integration samples is 512.

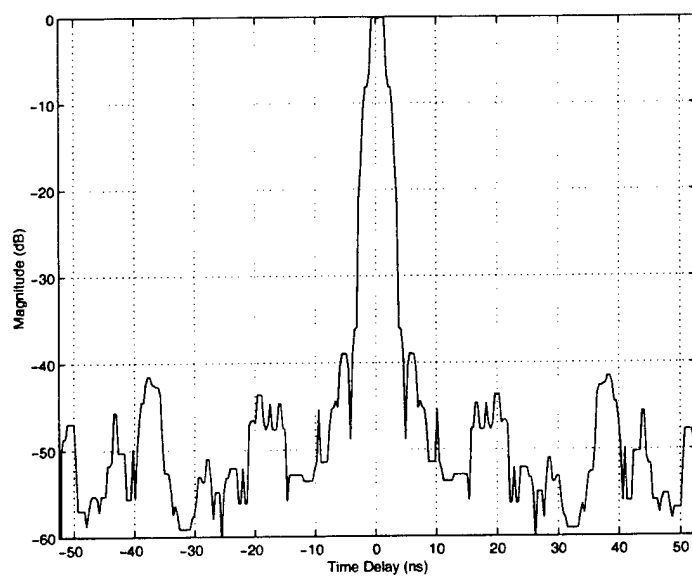
Figure 4.7(a) and (b) illustrate the variation of the ISLR and PSL of the ideal PSF as a function of the number of integration samples for noise radar. For comparison, the ISLR and PSL of several commonly used window functions are also illustrated. These include rectangular, Hamming and Kaiser ($\beta = 4$ and $\beta = 5$) windows. It can be seen that, when the number of integration samples is greater than 8, 512, and 4096, both the ISLR and the PSL of the PSF for noise radar are lower than those of the step-frequency radar with rectangular window, the Kaiser window with $\beta = 4$, and the Hamming window, respectively. This shows that with an adequate number of integration samples, it is possible for the noise radar to obtain images of quality as good as the step-frequency radar.

4.5.3 Comparison of Anti-RFI Performance

To achieve the very good foliage penetration capability, a FOPEN SAR has to operate at the lower frequency bands, i.e., VHF and UHF bands. Unfortunately, the VHF-UHF portion of the spectrum is already in heavy use by other services, such as television, FM radio stations, mobile communications, and so on. The ultrawide bandwidth required to achieve very high resolution creates a situation where the radar must share its band with the above mentioned emitters and receivers. Even in remote locations, the radio frequency interference (RFI) power often exceeds receiver noise by many dB, severely degrading the SAR images. As a consequence, the anti-RFI performance is one of the most important specifications for

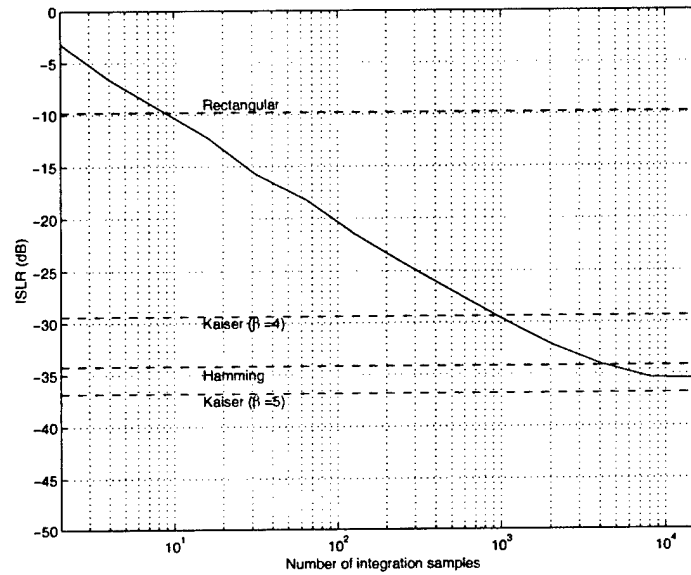


(a) Down range PSF of step-frequency radar.

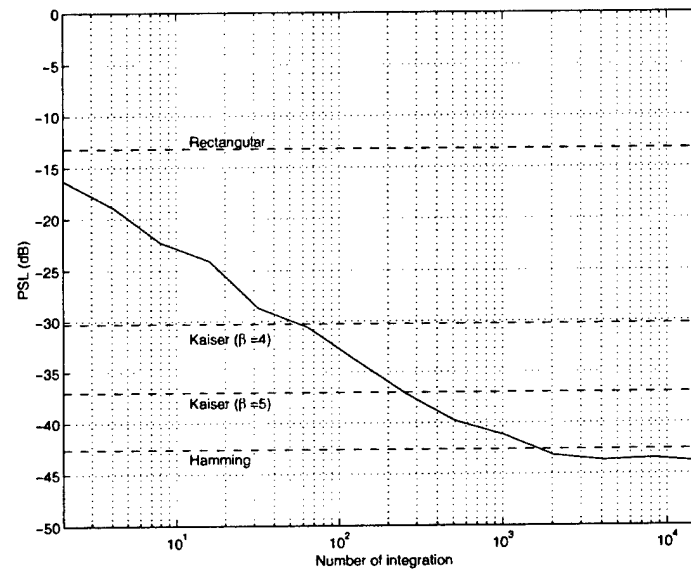


(b) Down range PSF of the random noise radar.

Figure 4.6: Ideal PSFs of the two radar systems.



(a) ISLR versus number of integration samples.



(b) PSL versus number of integration samples.

Figure 4.7: ISLR and PSL as functions of the number of integration samples. The solid line shows the noise radar, while the dashed lines show the step-frequency radar with appropriate taper window.

FOPEN applications.

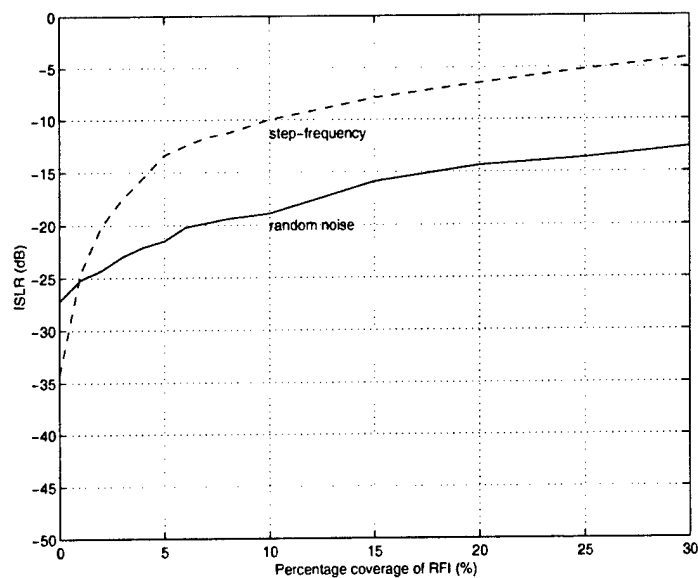
To investigate the anti-RFI performance of the FOPEN UWB random noise radar with comparison to a UWB step-frequency radar, the RFI is modeled as a superposition of single sinusoidal “tone”. We are only considering RFI picked up by the receive antenna. The amplitudes of the RFI signals are assumed to be constant during the radar integration processing. This is basically true as most RFI has a modulation time of 5-10 μ s [64, 65]. The distribution of the various RFI signals are assumed uniformly random within the radar operation band.

In step-frequency radar, we assume that the source of the RFI and its frequency band are known, and that a notch filter is applied to block the RFI. The result of this process is that the signal spectrum has gaps or deep notches, thus resulting in increased ISLR and PSL. On the other hand, in the noise radar case, the correlation receiver has a non-zero output only when a delayed replica of the transmitted waveform is received. Thus, we assume that the RFI is automatically reduced by the correlation-integration process within the receiver, due to the fact that the RFI is completely uncorrelated with the radar transmit noise waveform. However, due to the limited number of integration samples, we expect that the ISLR and PSL will be increased when RFI exists.

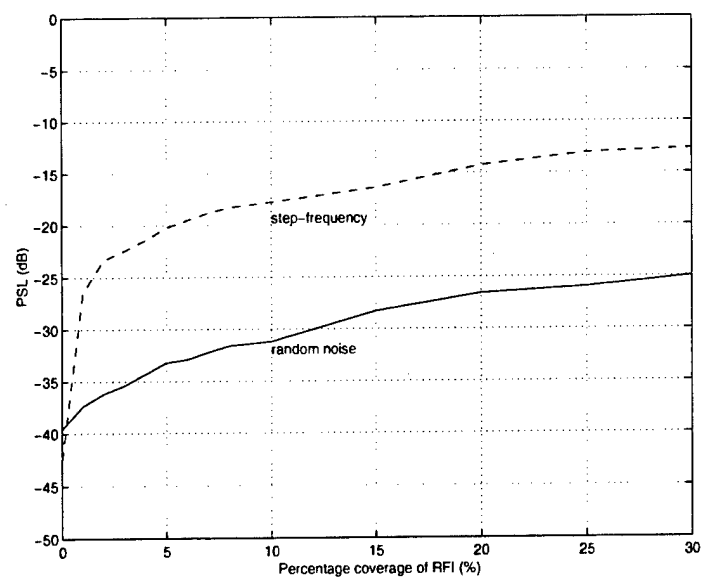
Figures 4.8 illustrates the ISLR and PSL versus the percentage bandwidth coverage of the RFI, for step-frequency and random noise radars, respectively, where the RFI-to-signal ratio is 20 dB. For noise radar, the number of integration samples is 512. Note that in the sense of anti-RFI performance improvement, there is no advantage to increase the integration number for step-frequency radar, if the positions and amplitudes of the RFI are fixed. From this figure it can be seen, when the percentage bandwidth coverage of the RFI exceeds about 1 percent, the random noise radar always performs much better than the step-frequency radar.

4.5.4 Comparison of the Foliage Obscured PSFs

The foliage obscured PSFs in down range for the step-frequency radar and for the random noise radar can be seen in Figure 9(a) and (b), respectively. The unobscured PSFs are also shown (dashed lines). It is seen that the PSFs of the two systems, when affected by the



(a) ISLR versus percentage bandwidth coverage of RFI.



(b) PSL versus percentage bandwidth coverage of RFI.

Figure 4.8: ISLR and PSL as functions of the percentage bandwidth coverage of RFI.

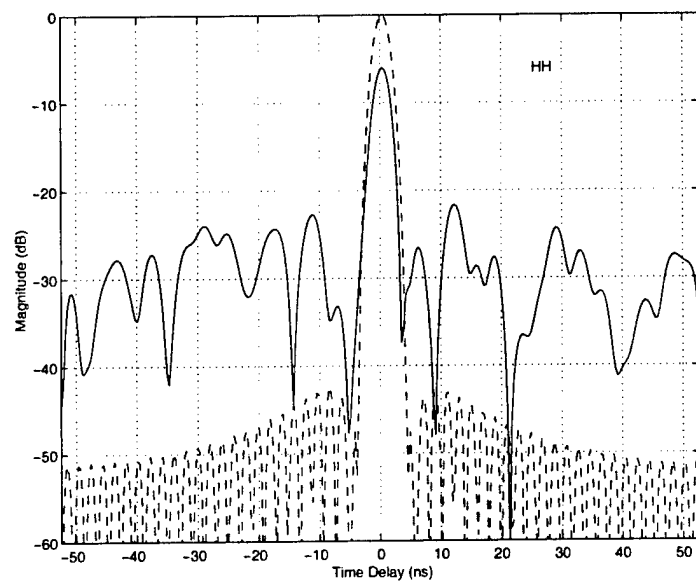
foliage, behave in a similar manner: the energy of mainlobe is attenuated, while the levels of the sidelobes are increased. A statistical analysis of the ISLR and PSL for 100 runs shows that, the ISLR of the random noise radar is always about 3 dB lower than that of the step-frequency radar, while the PSLs for both radar systems are almost at the same level.

To study how the foliage obscures an ideal point target in its 2-D image, Figure 10 illustrates the unobscured and the foliage obscured 2-D PSFs for the step-frequency radar (Figure 10(a) and (b)) and for random noise radar (Figure 10(c) and (d)), respectively. Notice that in order to observe the obscuring pattern clearer, here we have a 58-dB dynamic range for all the images. These images pertaining to the 2-D PSFs support the conclusion about the foliage distortion pattern analysis in the foregoing section.

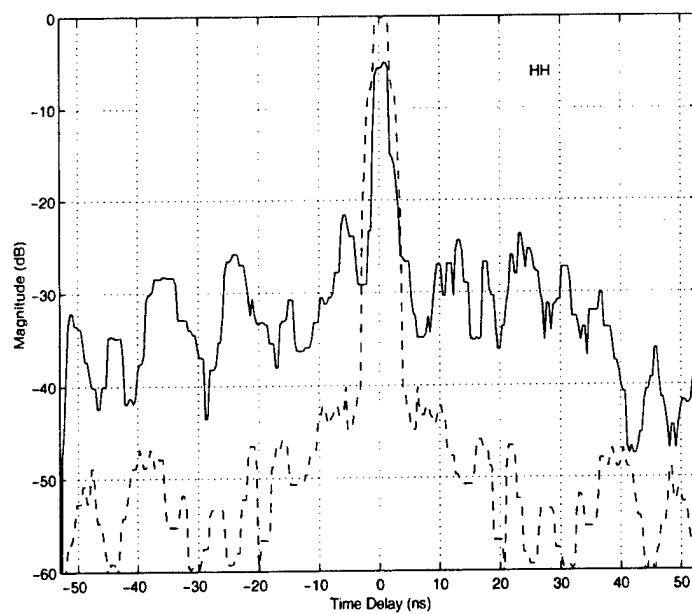
4.5.5 Comparison of the 2-D images for complex target

The measured signature data of a scaled target model were used in the simulation, as the FOPEN noise radar system is still under development and full-size target data are unavailable at the moment. The signature data were acquired in an anechoic chamber using a step-frequency radar at Beijing Institute of Environmental Features (BIEF). The physical size of the model is approximately $0.85 \text{ m} \times 0.65 \text{ m}$, measured at a central frequency of 10 GHz with a bandwidth of 6 GHz. When scaled to UHF band by a scale factor of 26.67, the equivalent central frequency is 375 MHz with a bandwidth of 225 MHz, and the full size of the target is $22.7 \text{ m} \times 17 \text{ m}$. The equivalent integration angle for aperture synthesis is 28° .

In the foliage obscured image simulation, for step-frequency radar, the model in Figure 4.2 is directly applied, i.e., the measured data are taken as the ideal target response, the two-way foliage transmission is generated by the model in Section 4.3. The foliage obscured frequency-domain target signatures are then obtained by the multiplication of the ideal target response with the two-way foliage transmission. The foliage obscured 1-D down range profiles can be formed by applying 1-D fast Fourier transform (FFT). For random noise radar, a band-limited Gaussian random noise signal is also generated. The foliage obscured frequency-domain signatures are multiplied by the spectrum of this noise signal and 1-D FFT is applied to obtain the time-domain version of the noise radar target echoes. The time-domain target echoes are then correlated with the band-limited noise signals to obtain



(a) Foliage obscured PSF for step-frequency radar.



(b) Foliage obscured PSF for the random noise radar.

Figure 4.9: Foliage obscured down range PSFs of the two radar systems.

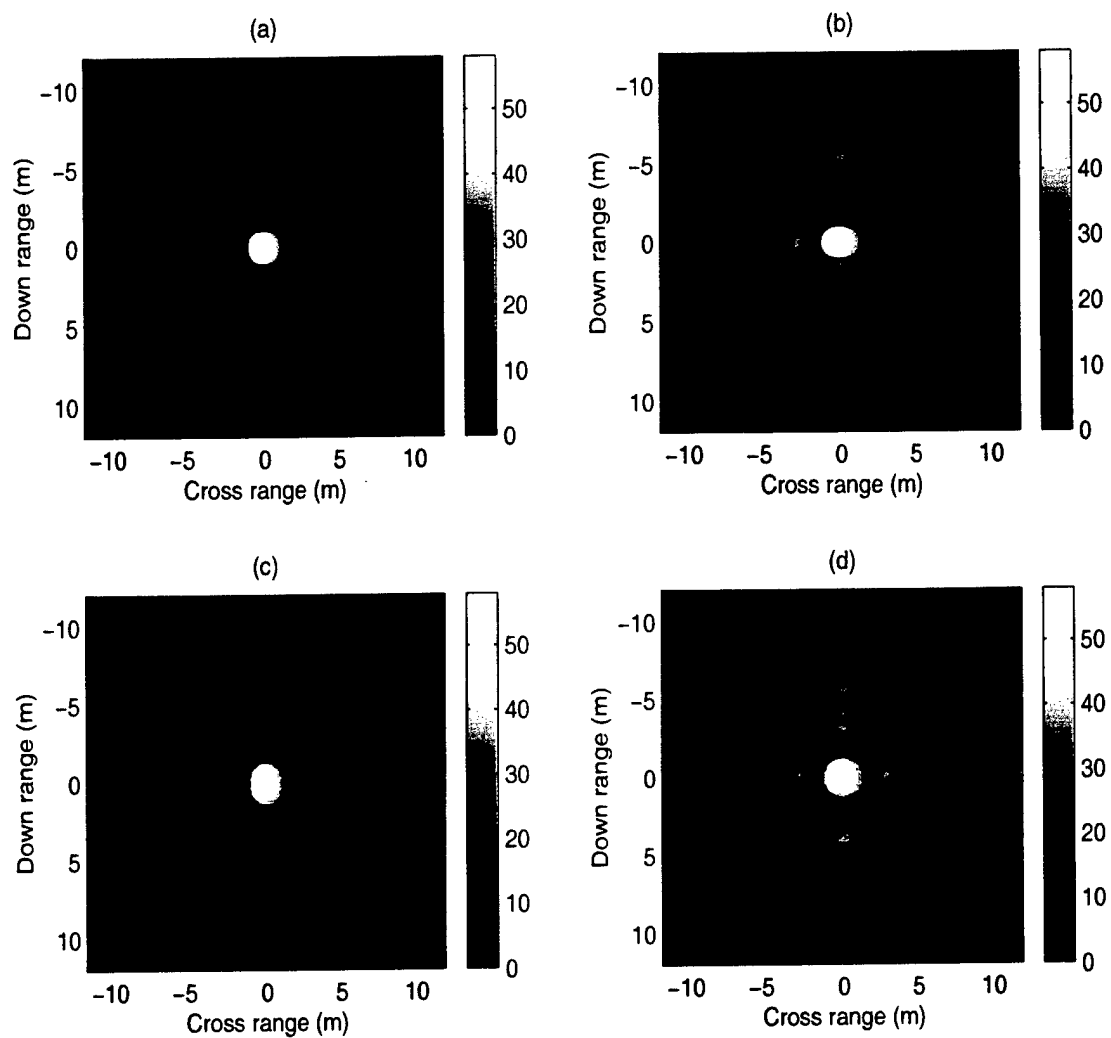


Figure 4.10: Comparisons of the 2-D PSFs of the two radar systems. (a). Unobscured PSF for step-frequency radar; (b). Foliage obscured PSF for step-frequency radar; (c). Unobscured PSF for random noise radar; and (d). Foliage obscured PSF for random noise radar.

the 1-D down range profiles. A back-projection algorithm is then used to form the 2-D images for both radar systems.

The two-dimensional (2-D) images of the above target for the step-frequency radar are illustrated in Figure 4.11, and the images for the random noise radar with different integration numbers of 32, 128 and 512, respectively, are shown in Figures 4.12 through 4.14. Note that much more obscured images are obtained for VV polarization in these figures. This results from the following two facts: First, at UHF band and for VV polarization, the foliage is more fluctuating in its amplitude and phase characteristics in comparison to the case of HH polarization. Second, in this particular example, the target has a special strong scatterer at VV polarization, which is *dispersive* along the cross range axis; this horizontal-bar-like image of the scatterer, when obscured by foliage in the way as discussed in the former section, is greatly blurred along the down range dimension over the whole frame of the image.

From Figures 4.11 through 4.14, it can also be seen that, whether the target is or not obscured by foliage, the 2-D images of the noise radar are very similar to that of the step-frequency radar. However, for the noise radar images, some low-level noise background can be found when the integration numbers are small, although at large integration numbers, the noise radar images are comparable to the step-frequency radar. This suggests that the random noise radar system must ensure adequate averaging in order to achieve comparable performance to the step-frequency system.

4.6 Summary

In this chapter, we have developed a statistical-physical model of foliage transmission for FOPEN radar simulation applications. The foliage distortion pattern was analyzed by means of the method of paired echoes. With the proposed model, we have compared the behavior of a step-frequency radar and a random noise radar for FOPEN imaging applications. It can be seen that the two radar systems are nearly identical in the quality of images either without or with obscuring foliage, provided in the noise radar case we achieve adequate integration of the target returns at each range cell. In a realistic scenario, this is not a problem. Our results demonstrate the ability of the UWB random noise radar to be used as a FOPEN

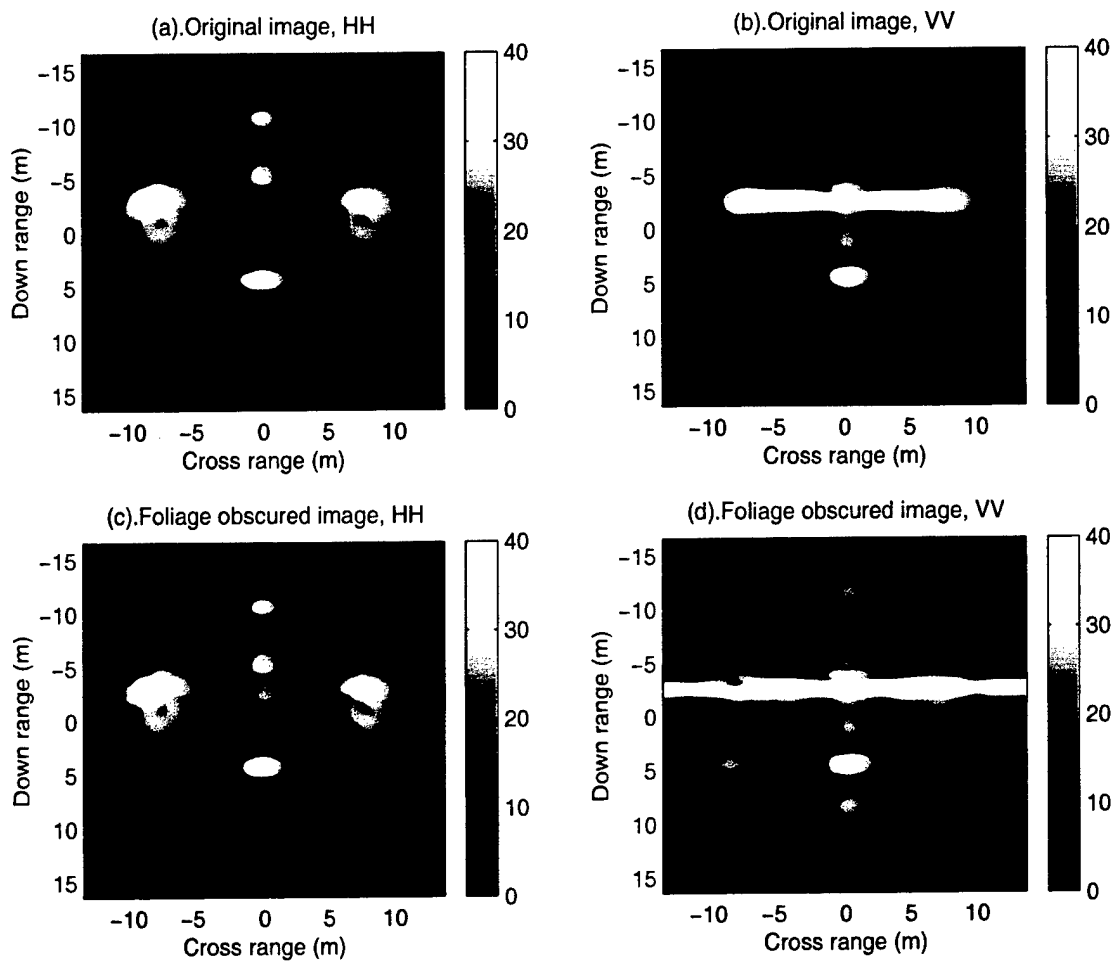


Figure 4.11: 2-D images of step-frequency SAR.

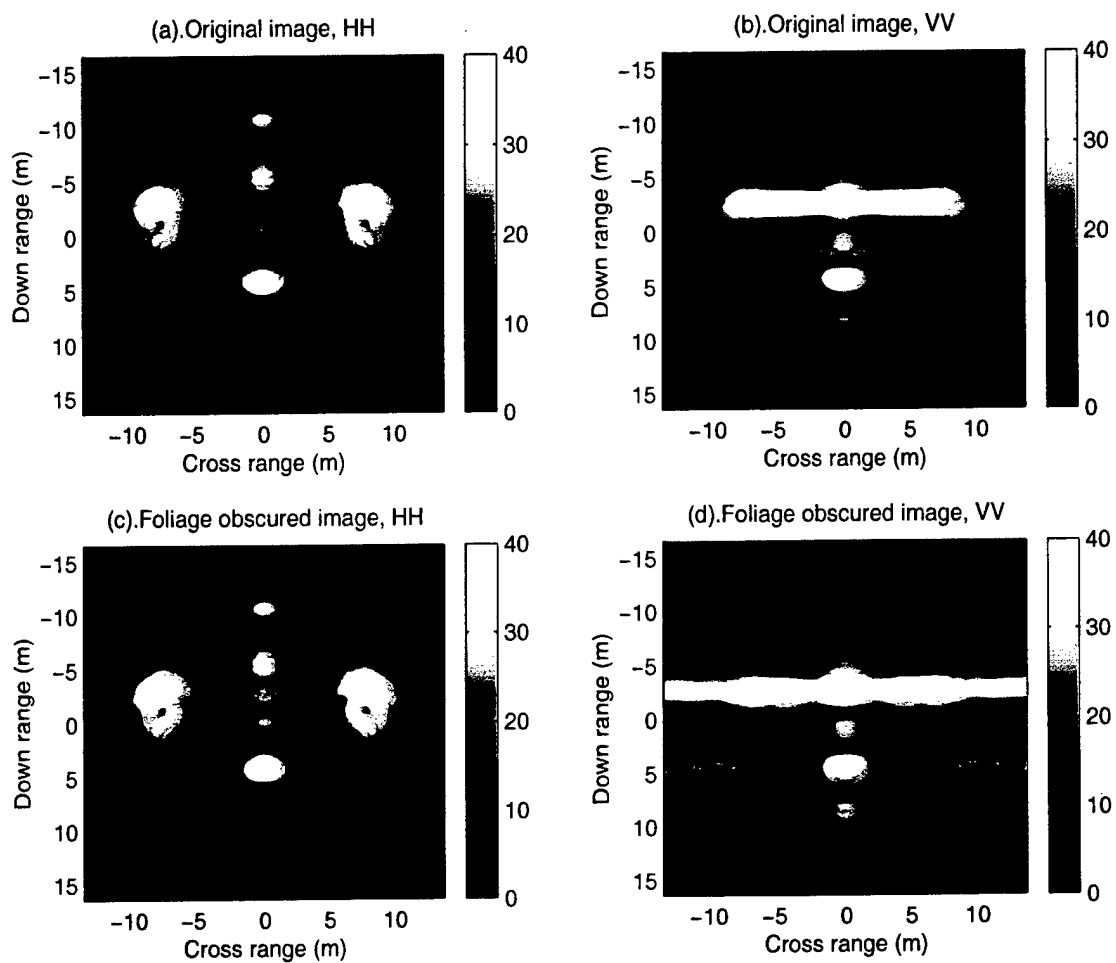


Figure 4.12: 2-D images of random noise SAR, integration number 32.

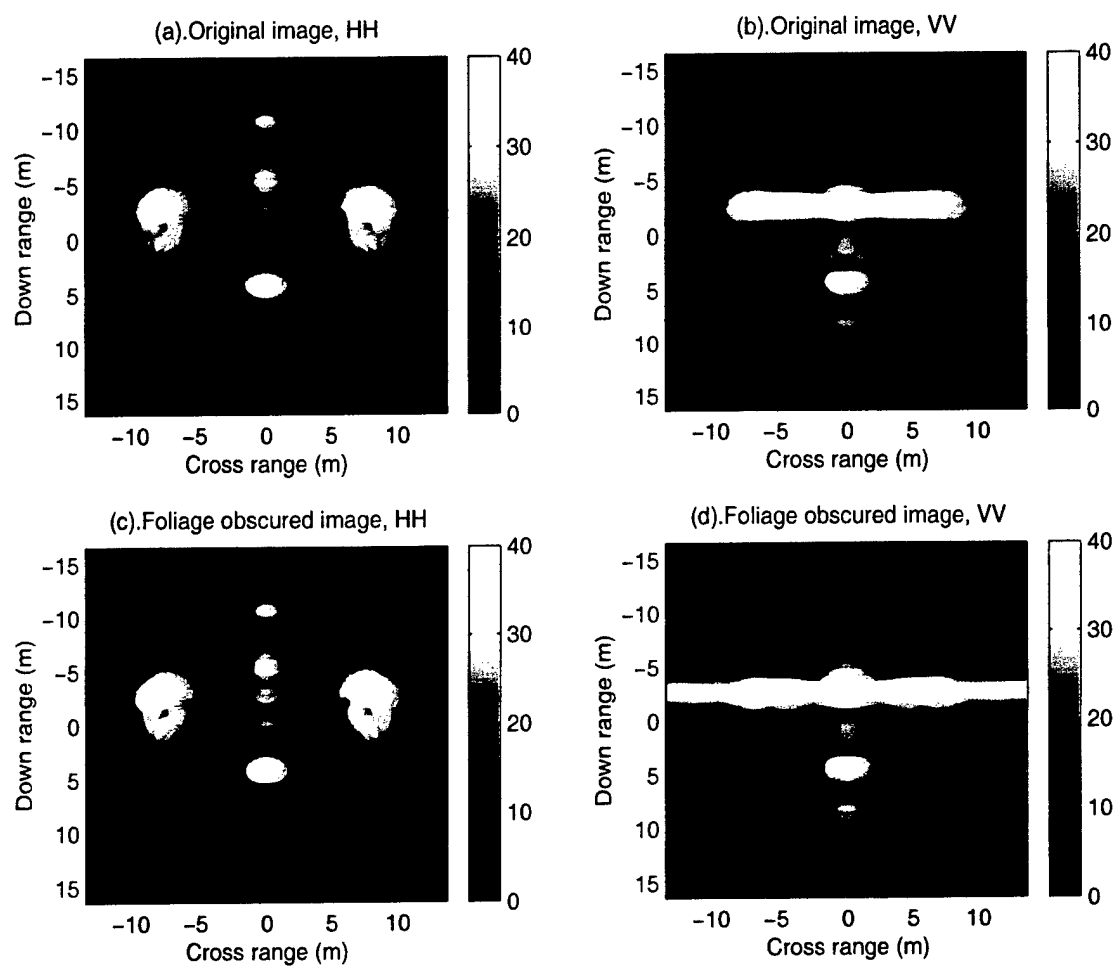


Figure 4.13: 2-D images of random noise SAR, integration number 128.

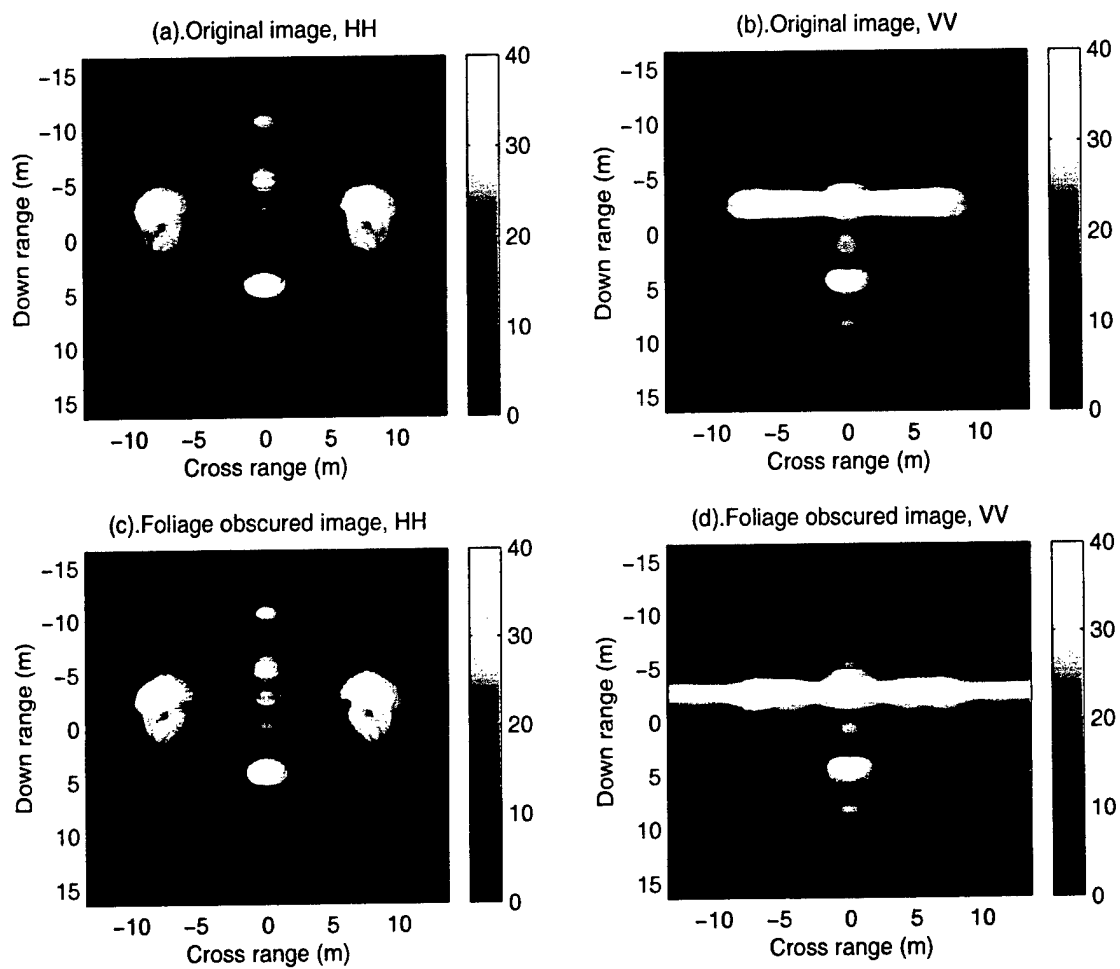


Figure 4.14: 2-D images of random noise SAR, integration number 512.

SAR, with relative immunity from interference and detection.

Chapter 5

FOPEN UWB RANDOM NOISE SAR IMAGE FORMATION

5.1 Background

FOPEN and ground penetration (GPEN) UWB SARs are one of the latest generations of high resolution imaging radars. Such a radar system usually has two unique features:

- (a) It operates at a lower frequency band such as VHF and UHF bands; and
- (b) It usually has exceptionally large fractional bandwidth and antennas with wide angular beamwidths that span tens of degrees.

One example of such UWB radar systems is the Army Research Laboratory (ARL) Boom SAR, which transmits an impulse waveform in the frequency band 20 MHz - 1.1 GHz [66], with a fractional bandwidth of 200% and the beamwidths of the antennas larger than 90°. This kind of imaging radars are grouped as the ultra-wide band, wide angle (UWBWA) SARs [67]. In contrast to the signal processing of conventional SARs, different processing algorithms must be adopted for UWBWA SARs, because many of the simplifying assumptions made in conventional SAR imaging are no longer valid [68]. A set of analytical models for the ARL Boom SAR was first developed by Rau and McClellan [67].

In Chapter 2, a model of the UWB coherent random noise radar system was established, where it is pointed out that a UWB random noise radar can be modeled as a UWB short-pulse radar which transmits a pulse waveform and receives the returned pulses using an

ideal sampler at specified time delays. In this chapter, we first develop a time-domain radar response model for FOPEN UWB random noise radar imaging. The 2-D FOPEN SAR imaging model for a generalized near-field bistatic UWBWA SAR imaging configuration using the random noise radar system are then developed. This is followed by a description of the image formation and processing techniques. Finally, the impact of the frequency and azimuthal angle dependent target radar cross section (RCS) on the UWBWA SAR images is discussed.

5.2 1-D Time Domain Radar Response Model

By considering that the random noise radar transmitter transmits a short-pulse waveform $p(t)$, while the receiver performs as an ideal sampler $\delta(t - \frac{R_u}{c})$, the 1-D time domain response of the FOPEN UWB random noise radar can be represented as in Figure 5.1, where

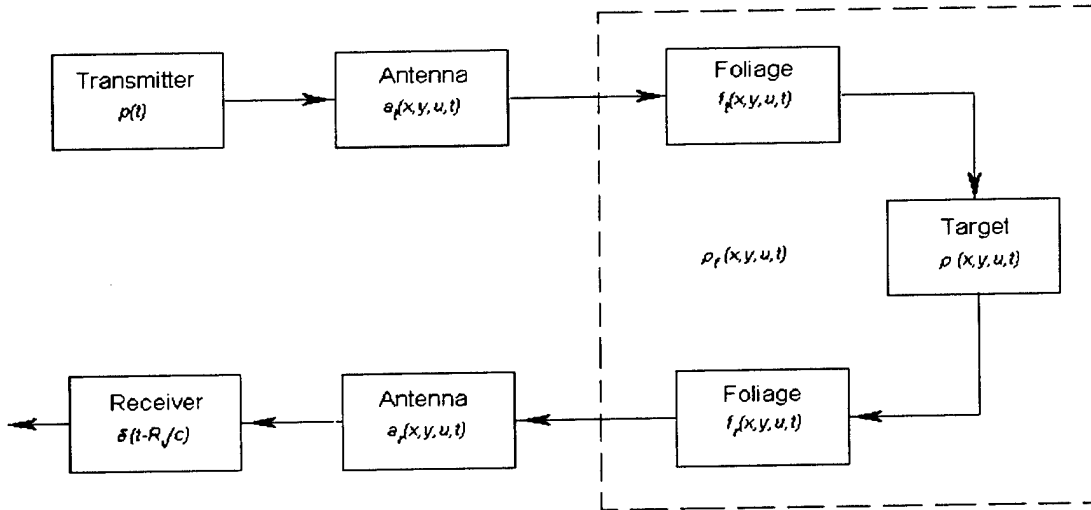


Figure 5.1: 1-D FOPEN random noise radar response model

- $p(t)$ =transmitter short-pulse waveform,
- $\delta(t - \frac{R_u(x, y, u)}{c})$ =receiver response as an ideal sampler,
- $a_t(x, y, u, t)$ =characteristics of the transmit antenna,
- $a_r(x, y, u, t)$ =characteristics of the receive antenna,
- $\rho(x, y, u, t)$ =target reflectivity function,

$f_t(x, y, u, t)$ =foliage transmission in the transmit channel,

$f_r(x, y, u, t)$ =foliage transmission in the receiving channel, (u, v) and (x, y) denote the radar coordinate system and target coordinate system, respectively; $R_v(x, y, u)$ is the two-way distance between the radar and the target point (x, y) , as will be defined later.

Note that in the radar coordinate system, we choose that the v -axis coincident with the t -axis. The received signal from target point (x, y) can thus be expressed in the convolution form as

$$g_r(x, y, u, t) = p(t) \otimes a_t(x, y, u, t) \otimes f_t(x, y, u, t) \otimes \rho(x, y, u, t) \otimes f_r(x, y, u, t) \otimes a_r(x, y, u, t) \otimes \delta(t - \frac{R_v(x, y, u)}{c}) \quad (5.1)$$

where \otimes denotes convolution with respect to t . In FOPEN imaging, the foliage transmission responses $f_t(x, y, u, t)$ and $f_r(x, y, u, t)$ serve as obscuring filters of the target reflectivity function $\rho(x, y, u, t)$. A mathematical analysis of the impact of foliage transmission on radar images can be found in Chapter 4. Denote the foliage obscured target reflectivity function by

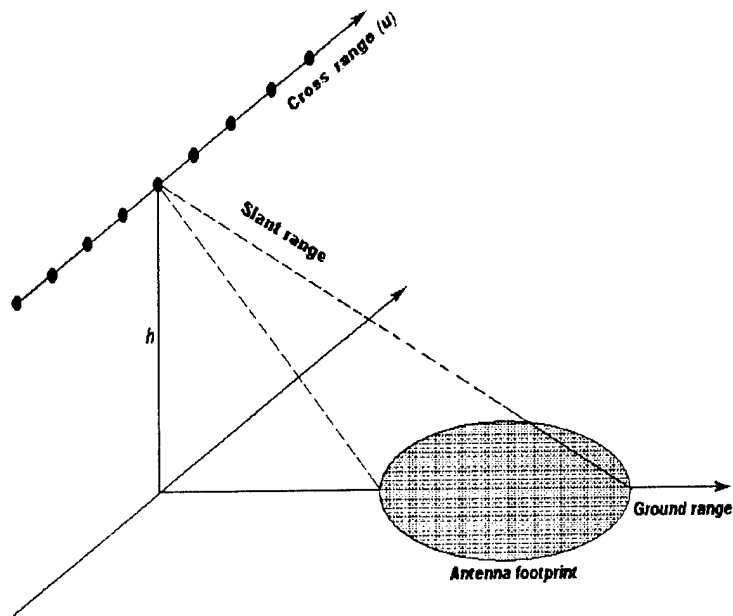
$$\rho_f(x, y, u, t) = f_t(x, y, u, t) \otimes \rho(x, y, u, t) \otimes f_r(x, y, u, t) \quad (5.2)$$

The impact of the foliage transmission is usually inseparable from the true target response. For simplicity, in the following we consider this foliage obscured target response as the "target reflectivity function", thus we have

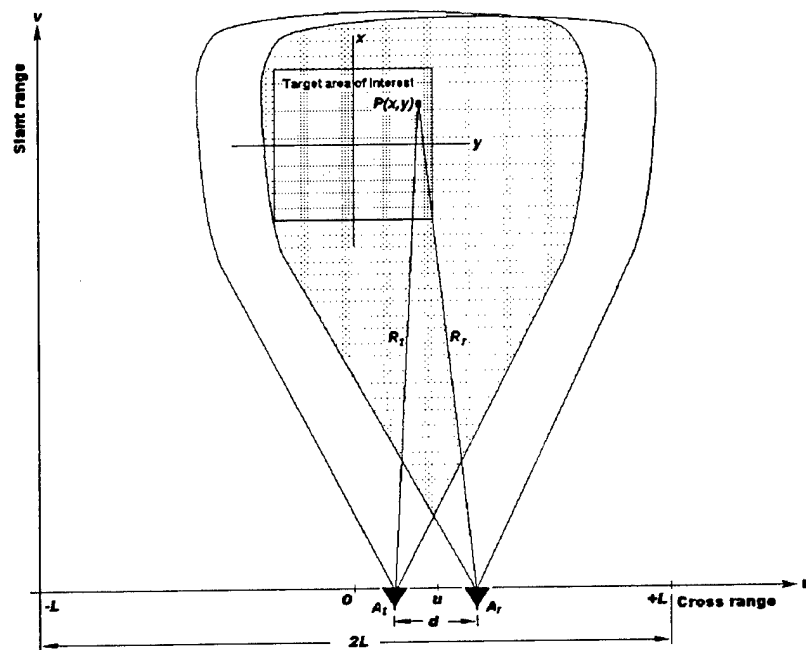
$$g_r(x, y, u, t) = p(t) \otimes a_t(x, y, u, t) \otimes \rho_f(x, y, u, t) \otimes a_r(x, y, u, t) \otimes \delta(t - \frac{R_v(x, y, u)}{c}) \quad (5.3)$$

5.3 2-D FOPEN SAR Imaging Model

Consider a near-field bistatic strip-map SAR imaging scenario. The three-dimensional (3-D) and the equivalent two-dimensional (2-D) data acquisition geometry for the FOPEN random noise SAR imaging are shown in Figure 5.2.



(a) 3-D data acquisition geometry.



(b) Equivalent 2-D imaging plane.

Figure 5.2: The 3-D and the equivalent 2-D imaging geometry for FOPEN random noise SAR.

The radar platform moves along a straight line path at a constant height, h , over the ground plane. In the equivalent 2-D slant-range/cross-range imaging plane, the radar coordinate system is $u - v$ system with zero range reference at O. The distance between the transmit and the receive antennas is d . Thus, at time t , the position of the radar (which refers to the mid-point of the two antennas) can be denoted by $(u, 0)$.

Consider a scattering point P at location (x, y) . The distances between the target point and the transmit and receive antennas are

$$R_t(x, y, u) = \sqrt{(u - \frac{d}{2} - x)^2 + y^2 + h^2}, \quad (5.4)$$

and

$$R_r(x, y, u) = \sqrt{(u + \frac{d}{2} - x)^2 + y^2 + h^2}, \quad (5.5)$$

respectively. Hence, the two-way distance is

$$\begin{aligned} R_v(x, y, u) &= R_t(x, y, u) + R_r(x, y, u) \\ &= \sqrt{(u - \frac{d}{2} - x)^2 + y^2 + h^2} + \sqrt{(u + \frac{d}{2} - x)^2 + y^2 + h^2}. \end{aligned} \quad (5.6)$$

The raw radar imaging data acquired at a specific radar position $(u, 0)$ is the integration of the returned signals from each target point (x, y) , i.e.,

$$d_p(u, t) = \int_{-\infty}^{+\infty} \int_0^{\infty} \frac{1}{R_t(x, y, u)R_r(x, y, u)} g_r(x, y, u, t) dy dx. \quad (5.7)$$

The factor $\frac{1}{R_t R_r}$ in the above equation takes account for the fact that both the incidence and the scattered fields propagate as spherical waves, the amplitude at any point on the wavefronts decrease as $1/R_t$ for the incidence wave and $1/R_r$ for the scattered wave, respectively.

Combining Eq.(5.7) with Eq.(5.4) we then obtain the raw radar data model for 2-D strip-map SAR imaging,

$$d_p(u, t) = \int_{-\infty}^{+\infty} \int_0^{\infty} \frac{1}{R_t(x, y, u)R_r(x, y, u)} p(t) \otimes a_t(x, y, u, t) \quad (5.8)$$

$$\begin{aligned}
& \otimes \rho_f(x, y, u, t) \otimes a_r(x, y, u, t) \otimes \delta(t - \frac{R_v(x, y, u)}{c}) dy dx \\
& = p(t) \otimes \int_{-\infty}^{+\infty} \int_0^{\infty} \frac{1}{R_t(x, y, u) R_r(x, y, u)} a_t(x, y, u, t) \\
& \quad \otimes \rho_f(x, y, u, t) \otimes a_r(x, y, u, t) \otimes \delta(t - \frac{R_v(x, y, u)}{c}) dy dx \\
& = p(t) \otimes d(u, t),
\end{aligned}$$

where

$$\begin{aligned}
d(u, t) &= \int_{-\infty}^{+\infty} \int_0^{\infty} \frac{1}{R_t(x, y, u) R_r(x, y, u)} a_t(x, y, u, t) \\
& \quad \otimes \rho_f(x, y, u, t) \otimes a_r(x, y, u, t) \otimes \delta(t - \frac{R_v(x, y, u)}{c}) dy dx.
\end{aligned} \tag{5.9}$$

For a better understanding of the above model, we make a few comments of the notations used.

In conventional 2-D SAR imaging, the target reflectivity function is usually modeled using a 2-D function $\rho(x, y)$, i.e., a weak scattering, isotropic and frequency-independent approximation [69] of the target scatterers is assumed. This approximation is sufficient when the radar operates at a higher frequency, and both the fractional bandwidth and the aspect angle span of the synthetic aperture are small. However, in FOPEN SAR imaging, it cannot be the case. In contrast, a FOPEN SAR usually operates at a lower bandwidth, with a very large fractional bandwidth, and need a very large aspect angle span of the synthetic aperture for a higher resolution. As a consequence, the target reflectivity is not only a function of the position (x, y) , but also a function of the radar frequency and the aspect angle, i.e., the target reflectivity is a 4-D function. A frequency dependent target can also be expressed as a time dependent target (as can be seen in Section 5), and an aspect dependent target is equivalent to a radar position dependent target. Thus, the 4-D target reflectivity can be represented using a function $\rho(x, y, u, t)$.

The characteristics of the antenna for a UWB radar is usually a function of the frequency, azimuth and elevation angles. Based on the similar reasons to the above and for a uniform representation, the characteristics of the transmit and receive antennas are modeled as two 4-D functions, $a_t(x, y, u, t)$ and $a_r(x, y, u, t)$, respectively.

As a last comment, note that the present imaging geometry is a near-field bistatic imaging configuration. This means that the aspect angle between the target and the transmit antenna, θ_t , and that between the target and the receive antenna, θ_r , are different. However, for a practical imaging configuration, this bistatic angle is small. According to the bistatic equivalent theorem [70], therefore, the 4-D target reflectivity function model is still valid.

5.4 SAR Image Formation

The objective of image formation is to reconstruct the target reflectivity function $\rho(x, y, u, t)$ by inverting the linear system defining the data acquisition in a way as exact as possible. In FOPEN imaging, we are going to reconstruct the foliage obscured target reflectivity $\rho_f(x, y, u, t)$. It is ready to find that, the target reflectivity is a 4-D function, while the SAR imaging scenario is a 2-D data acquisition configuration. As a consequence, it is impossible to reconstruct the complete 4-D function $\rho_f(x, y, u, t)$ by using the 2-D raw radar data. Instead, our major objective of interest is to reconstruct the 2-D (foliage obscured) target reflectivity function $\rho_f(x, y)$. This, once again, brings us to the problem of frequency and aspect angle dependent target signatures. The impact of frequency and aspect angle variation of target scattering on the SAR images will be studied later in the following section. We discuss the image formation first.

Rewrite the radar imaging data model in Eqs.(5.9) and (5.10),

$$d_p(u, t) = p(t) \otimes d(u, t), \quad (5.10)$$

and

$$d(u, t) = \int_{-\infty}^{+\infty} \int_0^{\infty} \frac{1}{R_t(x, y, u) R_r(x, y, u)} a_t(x, y, u, t) \otimes \rho_f(x, y, u, t) \otimes a_r(x, y, u, t) \otimes \delta\left(t - \frac{R_v(x, y, u)}{c}\right) dy dx. \quad (5.11)$$

By denoting

$$g(x, y, u, t) = a_t(x, y, u, t) \otimes \rho_f(x, y, u, t) \otimes a_r(x, y, u, t), \quad (5.12)$$

we have

$$d(u, t) = \int_{-\infty}^{+\infty} \int_0^{\infty} \frac{1}{R_t(x, y, u) R_r(x, y, u)} g(x, y, u, t) \otimes \delta(t - \frac{R_v(x, y, u)}{c}) dy dx. \quad (5.13)$$

Recall that our acquired radar imaging raw data is $d_p(u, t)$, which is a blurred version of $d(u, t)$ by the transmit pulse $p(t)$. However, due to the fact that we have equation (5.10) which defines the relationship between $d(u, t)$ and $d_p(u, t)$, we will consider the problem of image formation from “data” $d(u, t)$ first. As can be seen later, $d(u, t)$ can be recovered from the blurred signal $d_p(u, t)$ by using an equalization filter, if the radar transmit waveform $p(t)$ is known.

As stated at the beginning of this section, instead of trying to obtain the 4-D target reflectivity function $\rho_f(x, y, u, t)$, we must make a tradeoff between the acceptable images and the available radar imaging data, i.e., our purpose is to reconstruct the 2-D target function $\rho_f(x, y)$. Eqs.(5.12) and (5.13) tell us that, in a direct way of system inversion, we can at most obtain an good estimation of the antenna characteristics blurred reflectivity function, $g(x, y)$, from the radar data $d(u, t)$, if we use a back-projection algorithm, i.e.,

$$g(x, y) = \int_{-\infty}^{\infty} \int_{-\infty}^{\infty} R_t(x, y, u) R_r(x, y, u) d(u, t) \delta(t - \frac{R_v(x, y, u)}{c}) du dt, \quad (5.14)$$

The factor $R_t R_r$ is used for compensation of the R-loss of the incidence and the scattered fields.

We now come to the ideal sampler function $\delta(t - \frac{R_v(x, y, u)}{c})$ in the radar receiver. From equation (5.13), at a fixed radar aperture position $(u, 0)$, the radar receiver takes samples of the returned signals at time

$$\tau = \frac{R_v(x, y, u)}{c}, \quad (5.15)$$

which is the two-way propagation delay along the transmit antenna-target- receive antenna path. Thus, at radar position $u = u_i$, data $d(u_i, \tau)$ represents a slant range profile of the target area under imaging. In this range profile, the value at each time delay τ represents

an integrated returns along the parabola path $\tau = \frac{R_v(x,y,u_i)}{c}$. On the other hand, from Eq.(5.14), in the system inversion, we are going to back-project the range profile to the 2-D target (image) space (x, y) pixel by pixel, along the same parabola path specified by Eq.(5.15).

The desired information in SAR imaging is the target reflectivity function $\rho_f(x, y)$. The problem now is to determine how good an estimation of the target reflectivity function $\rho_f(x, y)$ we can obtain from $g(x, y)$.

Taking the Fourier transform of $g(x, y, u, t)$ in Eq.(5.12) with respect to t , we have

$$\begin{aligned} G_t(x, y, u, \omega) &= A_t(x, y, u, \omega) \rho_f(x, y, u, \omega) A_r(x, y, u, \omega) \\ &= H(x, y, u, \omega) \rho_f(x, y, u, \omega), \end{aligned} \quad (5.16)$$

where

$$H(x, y, u, \omega) = A_t(x, y, u, \omega) A_r(x, y, u, \omega), \quad (5.17)$$

is the combined transmit-receive antenna radiation pattern. Note that in our strip-map imaging geometry, u and x have the same directions, thus Eq.(5.17) can be rewritten as

$$H(x, y, u, \omega) = A_t(x - u, y, \omega) A_r(x - u, y, \omega), \quad (5.18)$$

With a reasonably long distance, Eq.(5.18) can be further approximated by [71]

$$H(x, y, u, \omega) = A_t(\theta_t, \omega) A_r(\theta_r, \omega), \quad (5.19)$$

where

$$\theta_t = \frac{2\omega(x - u - d/2)}{cR_t(x, y, u)}, \quad (5.20)$$

and

$$\theta_r = \frac{2\omega(x - u + d/2)}{cR_r(x, y, u)}, \quad (5.21)$$

For practical FOPEN radar imaging system, we have $\theta_t \simeq \theta_r = \theta$ if the transmit and the receive antennas are not too far apart. When two antennas with the same characteristics are used, we have

$$H(x, y, u, \omega) \simeq A^2(\theta, \omega), \quad (5.22)$$

where $A(\theta, \omega)$ is the antenna radiation pattern. Thus, with known antenna radiation pattern, the target reflectivity function $\rho_f(x, y)$ can be approximately recovered from $g(x, y)$ by applying an equalization filter $A^2(\theta, \omega)$ in the Fourier domain.

In summary, to reconstruct the (foliage obscured) target reflectivity function $\rho_f(x, y)$ from the raw radar data $d_p(u, t)$, the following procedure can be used.

Step-1: Fourier transform the raw data $d_p(u, t)$ and the radar transmit pulse $p(t)$ with respect to t ; obtain $D_p(u, \omega)$ and $P(\omega)$, respectively;

Step-2: In the Fourier domain, apply a bandpass filter which is corresponding to the radar operating frequency band, to $D_p(u, \omega)$ and to $P(\omega)$, and perform equalization filter to $D_p(u, \omega)$ using $P(\omega)$; obtain $D(u, \omega)$;

Step-3: Inverse Fourier transform $D(u, \omega)$, obtain the recovered data $d(u, t)$;

Step-4: Apply a back-projection algorithm to obtain $g(x, y)$ from the data $d(u, t)$;

Step-5: Fourier transform $g(x, y)$ with respect to y , obtain $G(x, \omega)$; Perform equalization filtering on $G(x, \omega)$ using the antenna radiation pattern $A^2(\theta, \omega)$, obtain the Fourier domain version of the target reflectivity function, $\Gamma(x, \omega)$;

Step-6: Inverse transform to the equalized data $\Gamma(x, \omega)$, obtain the approximately recovered final image $\rho_f(x, y)$.

Other processing can also be plugged into the above procedure for further improvement of the quality of reconstructed images.

5.5 2-D Image Sidelobe Reduction

5.5.1 Slant Range Apodization Filtering

As stated in the above procedure, the first step is to recover the data $d(u, t)$ from the radar raw data $d_p(u, t)$. Note that $d_p(u, t)$ can be considered to be a filtered version of $d(u, t)$ by a bandpass filter of impulse response $p(t)$, the equivalent transmit pulse of the random noise radar system. From Eq.(5.10), $d(u, t)$ can be recovered by performing a deconvolution on the raw data $d_p(u, t)$, or equivalently, by performing an equalization filtering in the Fourier domain.

As an example, Figure 5.3 illustrates the equivalent transmit short-pulse and the corresponding frequency spectrum for the 250-500 MHz FOPEN random noise radar built at UNL.

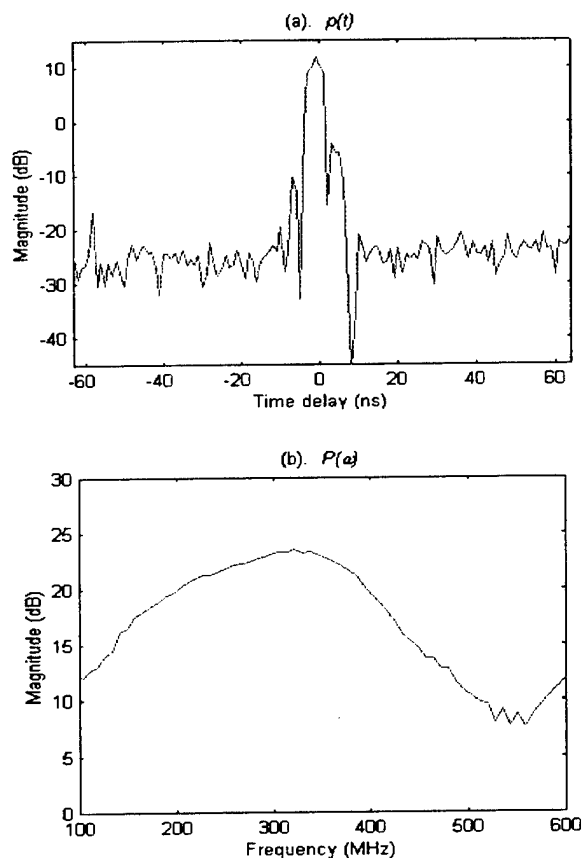


Figure 5.3: The equivalent transmit pulse and its frequency spectrum

In practical implementation, the above processing can be combined with other filtering operation for the compensation of other distortions in the imaging system and for the reduction of the slant range sidelobes. For example, a frequency domain apodization filter can be applied to the Fourier transform of the raw data. This filter has the form of

$$H_s(\omega) = \frac{W_s(\omega)e^{j\phi(\omega)}}{P(\omega)}, \quad (5.23)$$

where $P(\omega)$ is the Fourier transform of $p(t)$, $\phi(\omega)$ is a filtering function used to compensate the phase distortion in the system, and $W_s(\omega)$ is a window function for range sidelobe reduction.

5.5.2 Cross Range Sidelobe Reduction

In strip-map SAR imaging, the spectral region of support (ROS) of the focused image is a circular sector [71]. In conventional SAR imaging, this spectral ROS can be approximated as a rectangular region. Thus, a 2-D separable window function on rectangular grid can be applied for image sidelobe reduction. In UWB SAR imaging, however, this circular sector of spectral ROS can be no longer to be approximated as a rectangular region, due to the fact that a very large fractional bandwidth and a large aspect angle for synthetic aperture are used.

The slant range sidelobe can be reduced by applying a prescribed apodization filter to the Fourier domain data. To suppress the cross range sidelobes, another window function can be applied to the slant range apodization filtered data along the circular trellis of each slant range cell, as shown in Figure 5.4.

Figure 5.5 demonstrates the effectiveness of the 2-D image sidelobe reduction of a point target by using the filtering technique discussed above, where in both slant range and cross range, Taylor windows with -40 dB sidelobes are applied. Note that the dynamic range for all the images is 50 dB in the figure. It is seen that, when the aspect angle span of the synthetic aperture is not too large (e.g., 60°), the proposed sidelobe reduction method works very well. However, with the increase of the aspect angle span, the sidelobes close to the mainlobe start to obscure the images.

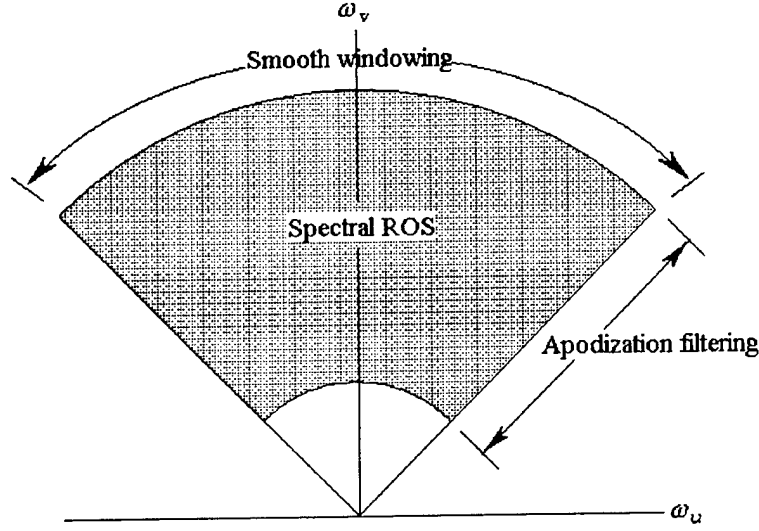


Figure 5.4: The spectral ROS of the focused SAR image.

5.6 Impact of Frequency and Azimuth Dependent Target RCS

In conventional SAR image processing, it is usually assumed that the target scattering is weak, isotropic and frequency independent. For conventional SAR imaging, where the target scattering lies in the optical region, the radar fractional bandwidth is small, and the required aspect angle span for aperture synthesis is relatively small. However, for FOPEN UWBWA radar imaging, where the radar operates at a lower frequency band, the fractional bandwidth is very large, and the required aspect angle span is also large, these assumptions are no longer satisfied. In this case, the frequency and azimuth variations of the target radar cross section (RCS) must be taken into account.

In the development of the SAR imaging model, the target reflectivity is modeled as a 4-D function $\rho(x, y, u, t)$. According to the image geometry in Figure 5.7 and the discussion in the former section, in Fourier domain, this is equivalent to a 4-D function $\Gamma(x, y, u, \omega)$. Note that ω and u correspond to the radar frequency and to the radar position or the target aspect angle, respectively. Thus we have in fact modeled the target reflectivity at position (x, y) as a frequency and aspect angle dependent function.

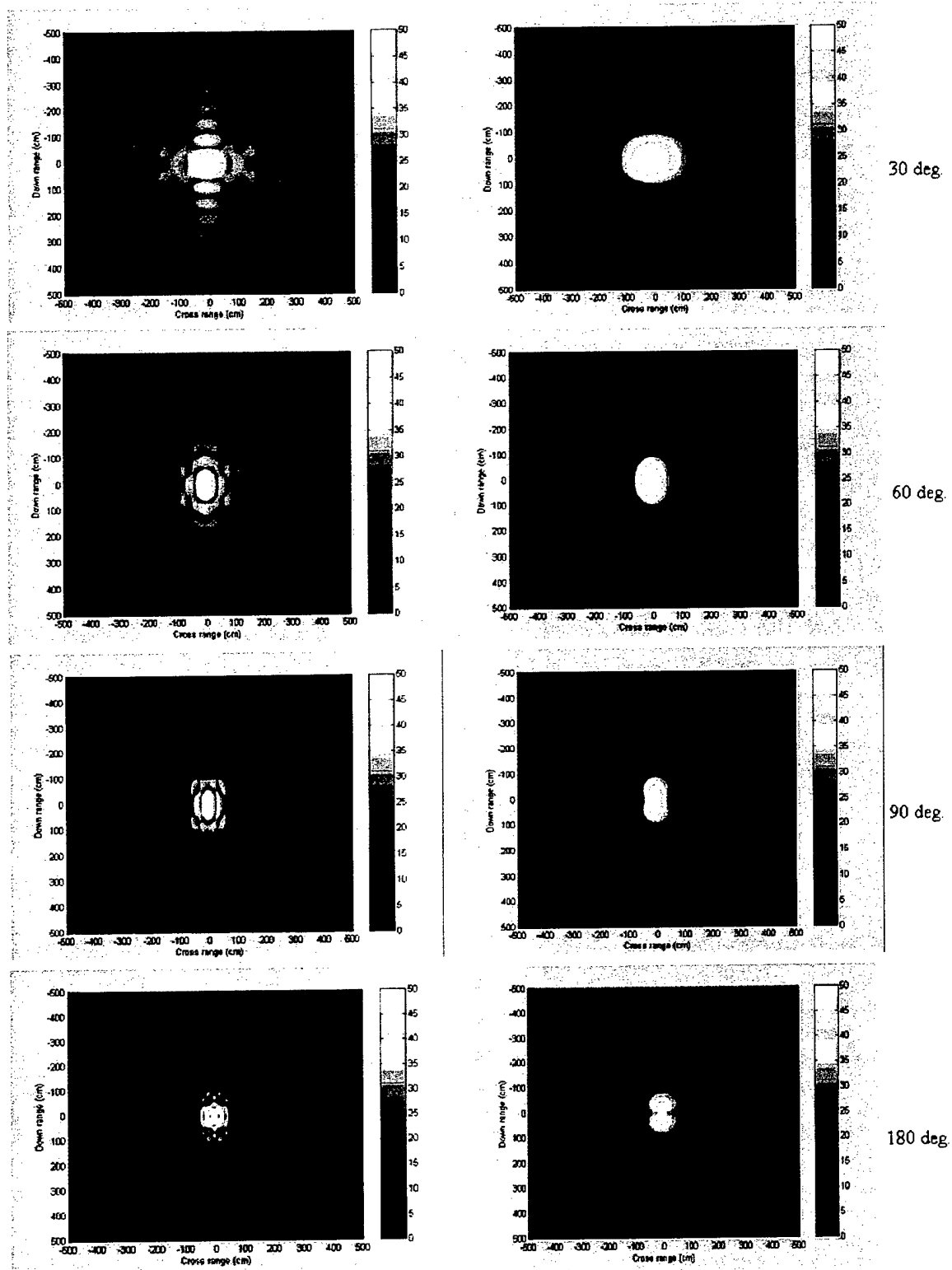


Figure 5.5: Images of a point target with different synthetic aperture angles.

The problem is that, in the image formation processing, instead of reconstructing a 4-D function $\rho(x, y, u, t)$ (or equivalently, $\Gamma(x, y, u, \omega)$ in Fourier domain), we can only reconstruct a 2-D function $\rho(x, y)$ (and for FOPEN imaging, the foliage obscured version, $\rho_f(x, y)$). It turns out that we must face to such a problem: What is the impact of the frequency and aspect angle dependent target RCS on the UWBWA SAR images?

Due to the fact that in the real world, the target scattering of interest is highly complicated, a generalized theoretical analysis is too difficult to be practical. Here we only consider two typical targets, namely, a conducting sphere and a circular plate. We then compare the images obtained by a UHF band UWBWA SAR with those obtained by a conventional SAR.

In all the images, for the UHF band UWB radar, the central frequency and bandwidth is assumed to be 375 MHz and 500 MHz, respectively, with a fractional bandwidth 1.33. For the conventional SAR, the central frequency is assumed to be 10 times higher than the UHF band UWB radar, i.e., 3.75 GHz, while the bandwidth is also 500 MHz, hence with a fractional bandwidth of 13%. It is therefore seen that, when with the same cross range resolution, the required aspect angle span of the synthetic aperture for the UWBWA SAR must be 10 times of that in the conventional SAR imaging.

5.6.1 Images of a Conducting Sphere

A conducting sphere with a radius of the same order as the radar wavelength exhibits an oscillating frequency response. However, its response is independent of the observation angle.

The Mie solution for the exact backscattering field of a perfectly conducting sphere can be expressed as [72]

$$\sqrt{\frac{\sigma}{\pi a^2}} e^{i\psi} = \frac{j}{ka} \sum_{n=1}^{\infty} (-1)^n (2n+1) (b_n - a_n) \quad (5.24)$$

where

$$a_n = \frac{J_n(ka)}{H_n^{(2)}(ka)} \quad (5.25)$$

$$b_n = \frac{ka J_{n-1}(ka) - n J_n(ka)}{ka H_{n-1}^{(2)}(ka) - n H_n^{(2)}(ka)} \quad (5.26)$$

where $H_n^{(2)}(ka) = J_n(ka) - jY_n(ka)$ is the Hankel function of the second kind, and $J_n(ka)$ and $Y_n(ka)$ are the Bessel functions of the first kind and the second kind, respectively; $k = \frac{2\pi}{\lambda}$, λ is the wavelength and a is the radius of the sphere. The phase reference point is at the center of the sphere.

Figure 5.6 shows the frequency response of a conducting sphere of radius 150 cm. The RCS oscillates around the geometric optics value (πa^2 or 8.5 dBsm), with damped excursions as the radar frequency increases. The damped interference pattern is due to a creeping wave that circles the rear of the sphere and is launched back in the direction of the radar. This creeping wave thus travels an additional distance of $(2 + \pi)a$ with reference to the specular reflection.

As a consequence of this particular scattering phenomena, the 2-D SAR images for the UHF band UWB radar and for a conventional wideband radar are very different, which are illustrated in Figure 5.7. In this figure, the images on the left are for the UWBWA SAR, while the images on the right side are for the conventional SAR. In this example, the aspect angle for aperture synthesis is 45° for the UWB radar (and thus 4.5° for the conventional SAR). It is seen that, for the UWB SAR, the 2-D SAR image of the conducting sphere includes two major components, the specular wave (physical optics component) and the creeping wave (resonant component). The arc traces of the two scattering centers are due to the fact that both of them are offset from the phase reference center. In contrast, in the conventional SAR radar image, only one specular scattering center is observable, due to the fact that the creeping wave is too weak to be seen at a higher frequency band.

5.6.2 Images of a Conducting Circular Plate

The backscattering from a large, flat surface is dependent on both frequency and the incidental angle. Specifically, using the physical optics approximation, the backscattering field from a conducting circular plate can be expressed as [73]

$$E(k, \theta) = \frac{\pi a^2 \cos \theta}{\lambda} \frac{J_1(2ka \sin \theta)}{ka \sin \theta} \quad (5.27)$$

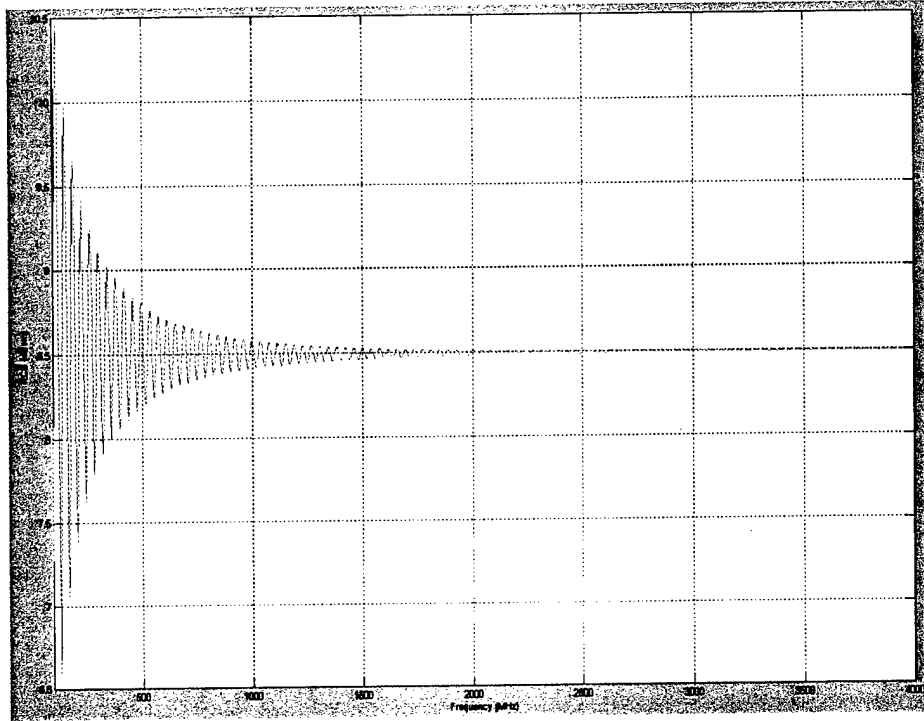


Figure 5.6: The frequency response of a conducting sphere of radius 150 cm.

where $J_1(\cdot)$ is the Bessel function of the first kind, a is the radius of the circular plate, and θ is the angle between the normal of the plate and the backscattering direction.

Figure 5.8(a) shows the RCS of a circular plate of radius 250 cm as a function of frequency and aspect angle. Figure 5.8(b) illustrates the aspect angle variation of the RCS at frequencies 375 MHz and 3750 MHz, respectively. In Figure 5.9, the 2-D images for the UWBWA SAR and for the conventional SAR are demonstrated. In this example, the central incidence aspect angle is 30° to the normal of the plate, and the aspect angle span is 35° for the UWBWA SAR and 3.5° for the conventional SAR, respectively.

From Figure 5.9 it can be seen that, for conventional SAR, the image of the circular plate mainly consists of two point scatterers, corresponding to the two edges separated by a distance equal to the diameter of the plate. However, for UWBWA SAR image, we obtain two radar signatures in the image, each consists of a major scattering mainlobe and dispersive sideband responses along the central radar line of sight (LOS) over the whole image area.

In summary, through two theoretical examples of UWB SAR images we have shown that:

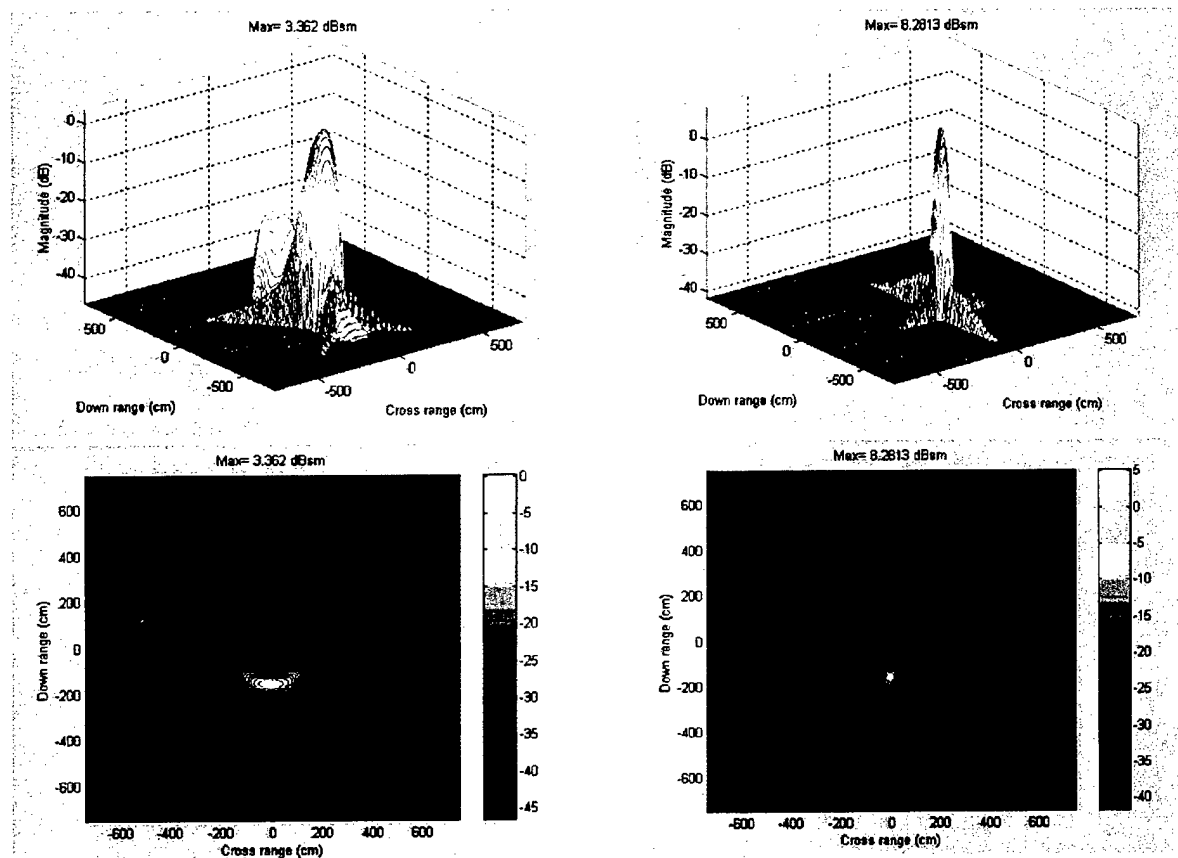
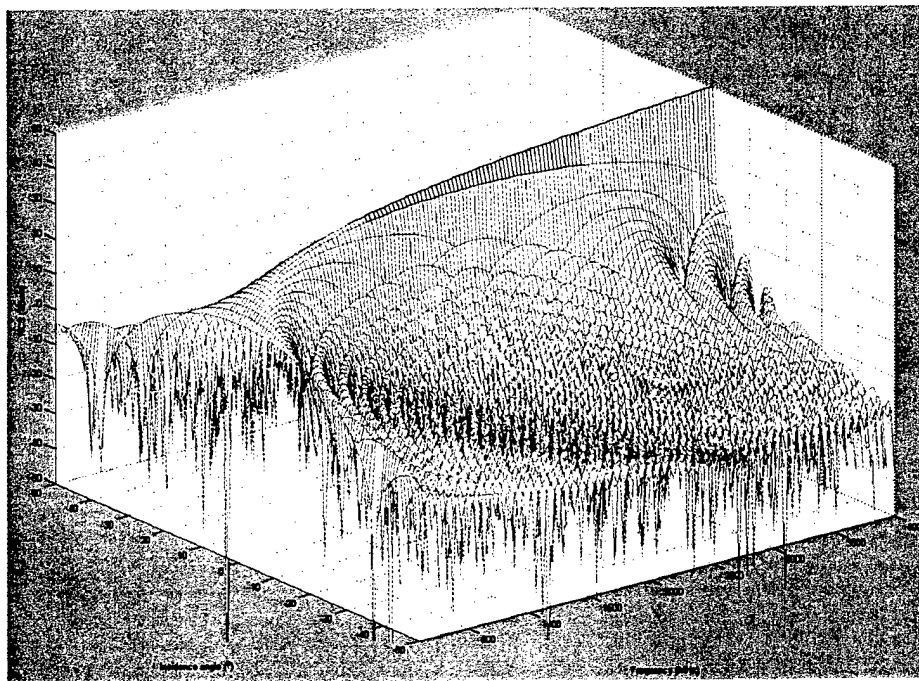
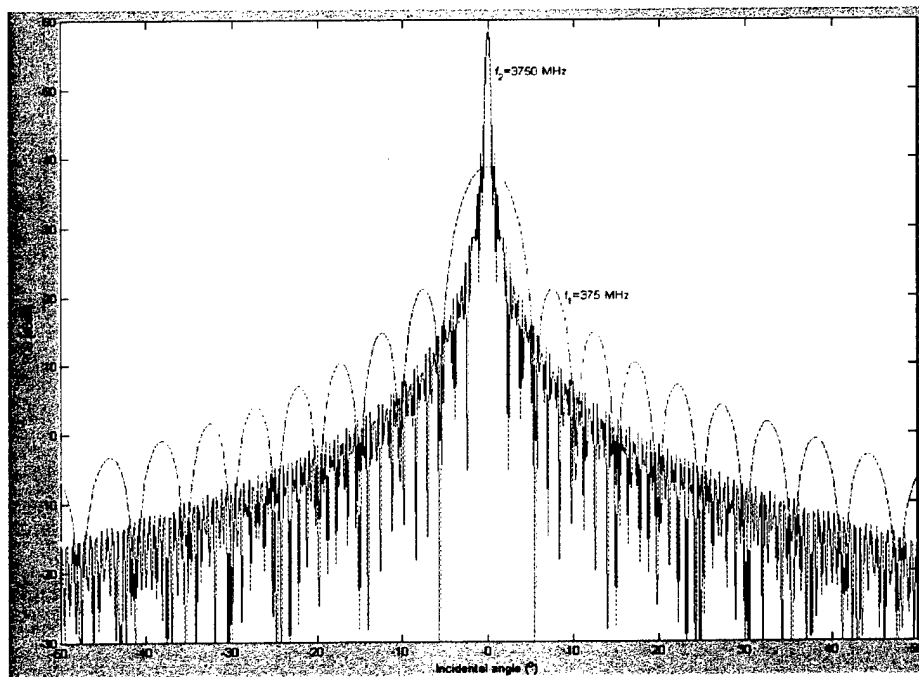


Figure 5.7: The 2-D images of the conducting sphere for the UWB (left) and conventional (right) SAR's.



(a). RCS as a function of frequency and incidence angle.



(b). RCS as a function of incidence angle at 375 MHz and 3750 MHz.

Figure 5.8: The RCS of a conducting circular plate of radius 150 cm.

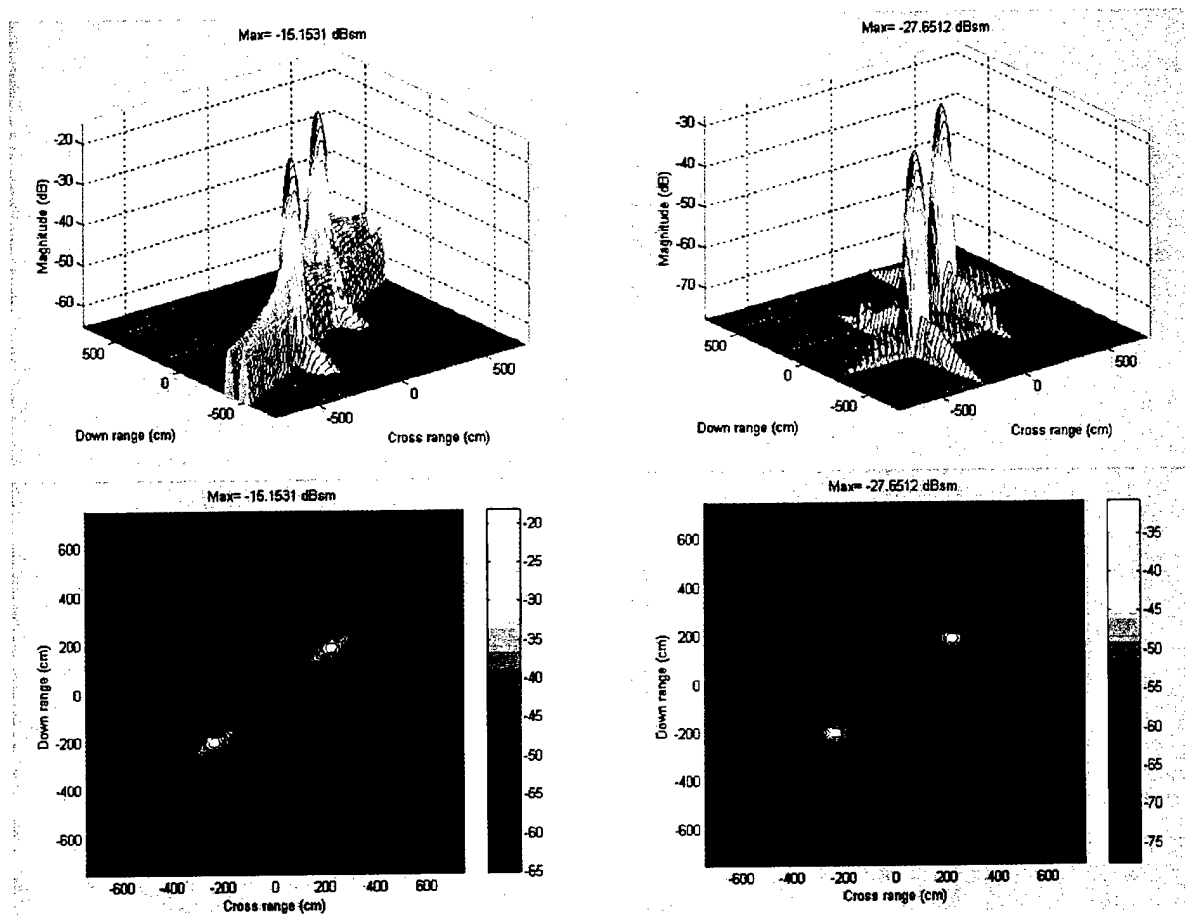


Figure 5.9: The 2-D images of the conducting circular plate at a 30° incidence angle for the UW (left) and conventional (right) SAR's.

(a) The weak, isotropic and frequency independent scattering model used in conventional SAR imaging is no longer valid for UWB SAR imaging;

(b) When a 2-D target reflectivity image $\rho(x, y)$ is obtained, instead of obtaining a 4-D target reflectivity function $\rho(x, y, u, t)$ due to the data acquisition limitation, we introduced image artifacts in the form of sideband responses in the resulting image;

(c) The UWBWA SAR images contain more information about the targets, thus are useful for radar target identification. However, these information usually appear as low level sideband responses. On the other hand, unlike in conventional SAR imaging where a 2-D separable window function can be applied to the (approximately) rectangular spectral ROS, it is more difficult to suppress the processing sidelobes in UWBWA SAR imaging. As a consequence, special image focusing and sidelobe reduction algorithms must be developed to suppress the processing sidelobes to a level as low as possible, such that the target signatures in the form of sideband responses can be exactly obtained.

Chapter 6

THREE-DIMENSIONAL INTERFEROMETRIC ISAR IMAGING TECHNIQUE

6.1 Background

High resolution imaging of radar targets is useful for target identification [74]-[77], target scattering modeling [78]-[80], as well as diagnostic studies of target scattering mechanisms [81]-[83]. A 2-D SAR or inverse SAR (ISAR) image represents the magnitude and locations in both down-range and cross-range of each scattering center on a complex radar target.

A major shortcoming of such a 2-D image is that it cannot provide information on the positions in altitude of the scattering centers. In contrast, a three-dimensional (3-D) image has the advantage of providing the exact position of each scattering center on a complex target in altitude as well as in down-range and cross-range. This problem has motivated the development of various configurations of 3-D ISAR imaging systems to measure the coherent backscattering signals of a target as a function of frequency, azimuthal and elevation angles [71, 83, 84]. The formation of accurate and coherent 3-D images typically requires dedicated signal processing in all the three dimensions. Thus, such conventional 3-D imaging configurations result in much greater burden on both signature data acquisition and image

formation computation. As a consequence, some simplified data collection and 3-D image formation techniques are preferred. Interferometric image processing is one such candidate technique.

Interferometric processing has long been applied in 3-D terrain-mapping using SAR. This technique, called interferometric SAR (IF-SAR), was firstly proposed and used to reconstruct the digital elevation model of the observed terrain scene by Graham [85]. Its rationale consists of imaging the same area from two different angles, thus providing a stereoscopic vision [86].

Interferometry was also introduced in inverse synthetic aperture radar processing (called IF-ISAR), with applications to motion determination of airborne sensors [87] and automatic aircraft landing [88]. Although IF-SAR and IF-ISAR share the same basic principles, in contrast to the long and widely applied IF-SAR in 3-D topographic terrain mapping, IF-ISAR has had only very limited applications to date, mainly in change detection but not altitude imaging.

There are several aspects which restrict the applications of IF-ISAR. First, a real-world complex man-made target usually appears highly fluctuating in its radar signature. The phase scintillation, known as target glint [69, 89], destroys the application of phase-coherent interferometry between two measurements. Second, for ISAR imaging, the objects to be imaged are usually small, with comparison to the terrain patch to be mapped as in IF-SAR. It requires much higher resolution and thus much more dedicated data acquisition and signal processing to obtain quality IF-ISAR images of such small-sized targets. Third, in practical applications, IF-ISAR runs into great difficulties in exact 2-D phase unwrapping required for altitude image formation. As is known, phase unwrapping is one of the most important steps in 3-D interferometric image processing. The wrapped phase can only be exactly recovered from its principal values if the following two conditions are satisfied:

- (a) the phase difference between two adjacent pixels in the 2-D ISAR images must be in the range of $(-\pi, \pi)$; and
- (b) the absolute values of the complex image must be nonzero everywhere, so that the phase is well defined everywhere.

The first condition can be satisfied by simply increasing the sampling rate. However, for man-made target imaging, the second condition is problematic. Unlike terrain mapping

where the images are continuous, real ISAR images of man-made targets do not exhibit such contiguous structures; instead, they typically consist of a collection of localized strong scatterers known as scattering centers. Thus, the phase unwrapping techniques developed in IF-SAR continuous terrain mapping can not be readily applied to IF-ISAR altitude image formation.

It is noteworthy to point out in the above that the first aspect is related to the second. The higher the radar resolution, the less the impact of the target glint. Therefore, with the development of wideband and ultra-wideband radar and digital signal processing techniques, those two restrictions can now be overcome. What is left is then the issue of phase unwrapping. However, if the targets to be imaged by IF-ISAR are relatively small in size, it is physically realizable to appropriately configure the two receiving antennas of the imaging radar, so as to overcome the ambiguity in unwrapping the phase difference between adjacent pixels. This then makes it possible to obtain 3-D high resolution images of complex targets by using interferometric image processing. The rationale for such a 3-D imaging technique is much similar to that of the differential IF-SAR mapping [89, 90].

In this chapter, we present an interferometric image processing technique for target 3-D altitude image formation. The 2-D ISAR images are obtained from the signature data acquired as a function of frequency and azimuthal angle. A 3-D IF-ISAR altitude image is then derived from two 2-D images reconstructed from the measurements by antennas at different altitudes. This chapter is arranged as follows. In Section 6.2, a generalized bistatic interferometric imaging system geometry is established. A brief description of the 2-D ISAR image reconstruction is made in Section 6.3. In Section 6.4, detailed mathematics for 3-D IF-ISAR image processing is developed. Some image formation issues are discussed in Section 6.5. In Section 6.6, IF-ISAR altitude image formation examples from both indoor and outdoor test range measurements are demonstrated. We finish the chapter in Section 6.7 with some conclusions and discussion.

6.2 3-D Imaging System Geometry

Consider a generalized bistatic interferometric ISAR imaging system geometry illustrated in Figure 6.1. The aperture is synthesized by target rotation with the rotation axis being the z -axis. Figure 6.1(a) shows the 3-D imaging geometry, while Figure 6.1(b) shows the detailed 2-D geometry when the target is rotated by an azimuthal angle θ . $O - uvz$ and $O - xyz$ are two coordinate systems fixed on the radar and on the target, respectively. Both coordinate systems have the same z -axis and original point, O , which is also the target rotation center. In the target coordinate system, y represents the down-range, x represents the cross-range in azimuthal dimension, and z denotes target altitude.

To characterize the electromagnetic scattering distribution in 3-D space of a target, we define a generalized 3-D target scattering density function $f(x, y, z)$. At high frequencies, this function also represents a collection of discrete scattering centers distributed in 3-D space.

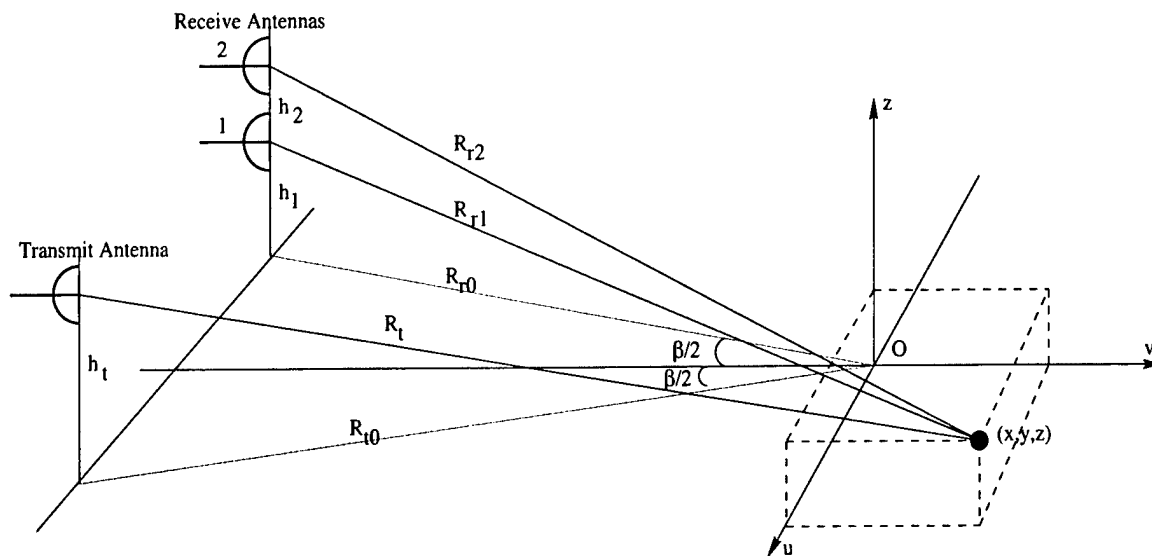
The transmit antenna is located at a distance R_t from the rotation center, O , with its coordinate $(R_{t0} \sin \frac{\beta}{2}, -R_{t0} \cos \frac{\beta}{2}, h_t)$, where β is the angle between the base of the transmit and the receive antennas, as subtended at the rotating center. The two receive antennas are located at $(-R_{r0} \sin \frac{\beta}{2}, -R_{r0} \cos \frac{\beta}{2}, h_1)$ and $(-R_{r0} \sin \frac{\beta}{2}, -R_{r0} \cos \frac{\beta}{2}, h_2)$, respectively. For simplicity, we assume that the transmit and receive antenna patterns are all constant over the illuminated target so that the effects of the antenna patterns can be ignored. The scattered fields can be measured over a range of frequency and rotating azimuth angle (f, θ) , where $f_{min} \leq f \leq f_{max}$ and $-\theta_{max}/2 \leq \theta \leq +\theta_{max}/2$. By weak-scatter approximation, the scattered fields measured by the i th receiving antenna can be expressed as

$$E_{si}(f, \theta) = C_0 \int \int \int_{D^3} f(x, y, z) \exp[-j \frac{2\pi}{\lambda} (R_t + R_{ri})] dx dy dz \quad (6.1)$$

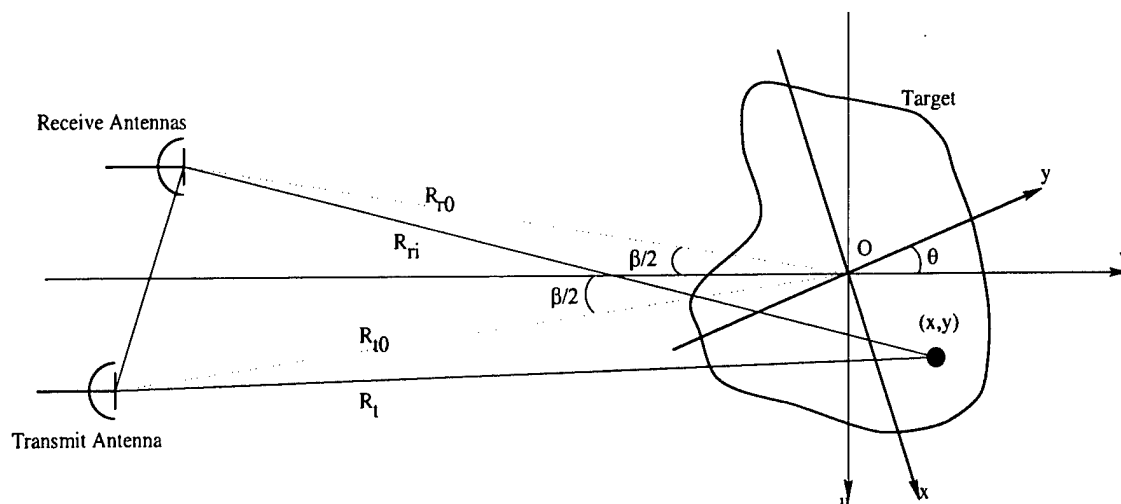
where $i = 1, 2$, C_0 is a complex constant, and D is the maximum extent of the target. Also,

$$R_t(x, y, z, \theta) = \sqrt{(u - R_{t0} \sin \frac{\beta}{2})^2 + (v + R_{t0} \cos \frac{\beta}{2})^2 + (z - h_t)^2}, \quad (6.2)$$

$$R_{ri}(x, y, z, \theta) = \sqrt{(u + R_{r0} \sin \frac{\beta}{2})^2 + (v + R_{r0} \cos \frac{\beta}{2})^2 + (z - h_i)^2}, \quad (6.3)$$



(a). 3-D imaging system geometry



(b). Detailed 2-D geometry when target rotating by an angle θ

Figure 6.1: 3-D interferometric ISAR imaging geometry.

and

$$\begin{aligned} u &= x \cos \theta + y \sin \theta, \\ v &= y \cos \theta - x \sin \theta. \end{aligned} \quad (6.4)$$

Combining Eq.(6.4) into Eqs.(6.2) and (6.3), we have

$$R_t(x, y, z, \theta) = \sqrt{R_{t0}^2 + x^2 + y^2 + (z - h_t)^2 - 2R_{t0}[x \sin(\theta + \frac{\beta}{2}) - y \cos(\theta + \frac{\beta}{2})]}, \quad (6.5)$$

$$R_{ri}(x, y, z, \theta) = \sqrt{R_{r0}^2 + x^2 + y^2 + (z - h_i)^2 - 2R_{r0}[x \sin(\theta - \frac{\beta}{2}) - y \cos(\theta - \frac{\beta}{2})]}. \quad (6.6)$$

6.3 2-D Image Reconstruction

We first consider the problem of 2-D ISAR image reconstruction at the plane $z = 0$. By neglecting the constant C_0 , the mathematical representation of the received fields in Eq.(6.1), for 2-D imaging, can be expressed as

$$E_s(f, \theta) = \int \int_{D^2} f_z(x, y) g(f, \theta, x, y) dx dy \quad (6.7)$$

where $f_z(x, y)$ can be considered to be the 2-D target scattering function which is the axis-integrated version of a 3-D scattering function $f(x, y, z)$ [69, 86], i.e.

$$f_z(x, y) = \int_D f(x, y, z) dz, \quad (6.8)$$

and $g(f, \theta, x, y)$ is the ISAR imaging system shift-variant impulse response which can be expressed as

$$g(f, \theta, x, y) = \exp\{-j \frac{2\pi}{\lambda} [R_t(x, y, 0, \theta) + R_{ri}(x, y, 0, \theta)]\} \quad (6.9)$$

where $\lambda = \frac{c}{f}$ is the radar wavelength, and c is the speed of light.

The 2-D scattering function $f_z(x, y)$ can then be reconstructed by coherently focusing the measured fields given in Eq.(6.7) in the image domain,

$$f_z(x, y) = \int_0^\infty \int_0^{2\pi} E_s(f, \theta) g^*(f, \theta, x, y) df d\theta \quad (6.10)$$

where $*$ denotes complex conjugate.

Since the scattered fields are measured over a range of frequency, $f_{min} \leq f \leq f_{max}$ and azimuthal angle, $-\theta_{max}/2 \leq \theta \leq +\theta_{max}/2$, an approximate reconstruction of $f_z(x, y)$, denoted by $\hat{f}_z(x, y)$, can be expressed as

$$\hat{f}_z(x, y) = \int_{f_{min}}^{f_{max}} \int_{-\theta_{max}/2}^{+\theta_{max}/2} E_s(f, \theta) g^*(f, \theta, x, y) df d\theta \quad (6.11)$$

Either FFT-based methods or backprojection algorithms [71, 86, 91] can be applied to the 2-D image reconstruction.

6.4 3-D IF-ISAR Image Processing

In the above section, we obtained the 2-D reconstruction, $\hat{f}_z(x, y)$, which is an approximated axis-integrated version of the 3-D target scattering function $f(x, y, z)$ at any constant target altitude, including $z = 0$. In practice, a real-world target always possesses a varying altitude $z(x, y)$ at every different 2-D position (x, y) .

The derivation leading to Eq.(6.11) shows that, in the reconstruction of 2-D ISAR images, the phase at each pixel in the 2-D image is preserved. This phase term involves target altitude and imaging geometry. The phase at each pixel for a single frame of ISAR images is not very much useful. However, by interferometric processing of the phases, pixel by pixel, of two ISAR images from two receive antennas at different altitudes (or depression angles), additional information about the third dimension, i.e., target altitude, can be obtained. In this section, we discuss how to obtain the 3-D target altitude image from the differential interferometry of its two 2-D ISAR images.

6.4.1 General Bistatic Imaging

Returning to the 3-D bistatic imaging system geometry in Figure 6.1(a), the phase difference between the two 2-D ISAR images at pixel (x, y) can be expressed as

$$\Delta\phi(x, y, \alpha_1, \alpha_2) = \frac{2\pi}{\lambda} [R_{r1}(x, y, z, 0) - R_{r2}(x, y, z, 0)] \quad (6.12)$$

where $R_{r1}(x, y, z, 0)$ and $R_{r2}(x, y, z, 0)$ are the distances between the target and the receiving antenna 1 and 2, respectively, at the rotation azimuthal angle $\theta = 0$. Define

$$\alpha_i = \tan^{-1} \frac{h_i}{R_{r0}}, \quad (6.13)$$

where α_i is the depression angle of the i th ($i = 1, 2$) receive antenna. Then, from Eq.(6.6) we have

$$R_{ri}(x, y, z, 0) = \sqrt{\frac{R_{r0}^2}{\cos^2 \alpha_i} + x^2 + y^2 + z^2 + 2R_{r0}(x \sin \frac{\beta}{2} + y \cos \frac{\beta}{2} - z \tan \alpha_i)}. \quad (6.14)$$

Expand $R_{ri}(x, y, z, 0)$ in a Taylor's series as $(1+x)^{\frac{1}{2}} = 1 + \frac{1}{2}x - \frac{1}{8}x^2 + \dots$. For typical radar imaging geometries, we have $\frac{D}{R_{r0}} \ll 1$ (Note that we do not invoke the more restrictive far-field condition of $R_{r0} \geq \frac{2D^2}{\lambda}$ at this moment). To ensure that the phase be accurate enough for interferometric processing, we preserve all the terms of the order $(\frac{D}{R_{r0}})^2$ in the Taylor's series. Thus we have

$$\begin{aligned} R_{ri}(x, y, z, 0) \simeq & \frac{\cos^3 \alpha_i}{2R_{r0}} z^2 + \sin \alpha_i \left(\frac{x \sin \frac{\beta}{2} + y \cos \frac{\beta}{2}}{R_{r0}} \cos^2 \alpha_i - 1 \right) z + \frac{R_{r0}}{\cos \alpha_i} \\ & + (x \sin \frac{\beta}{2} + y \cos \frac{\beta}{2}) \cos \alpha_i + \frac{(x^2 + y^2) \cos \alpha_i - (x \sin \frac{\beta}{2} + y \cos \frac{\beta}{2})^2 \cos^3 \alpha_i}{2R_{r0}}. \end{aligned} \quad (6.15)$$

Combining Eq.(6.15) into Eq.(6.12), the phase difference, $\Delta\phi(x, y, z, \alpha_1, \alpha_2)$ can be expressed as

$$\Delta\phi(x, y, z, \alpha_1, \alpha_2) = \frac{2\pi}{\lambda} [A(\alpha_1, \alpha_2)z^2 + B(x, y, \alpha_1, \alpha_2)z + C(x, y, \alpha_1, \alpha_2)] \quad (6.16)$$

where

$$A(\alpha_1, \alpha_2) = \frac{1}{2R_{r0}} k_1(\alpha_1, \alpha_2), \quad (6.17)$$

$$B(x, y, \alpha_1, \alpha_2) = (\sin \alpha_2 - \sin \alpha_1) \left[1 - \frac{x \sin \frac{\beta}{2} + y \cos \frac{\beta}{2}}{R_{r0}} k_2(\alpha_1, \alpha_2) \right], \quad (6.18)$$

$$C(x, y, \alpha_1, \alpha_2) = \left[\frac{R_{r0}}{\cos \alpha_1 \cos \alpha_2} - x \sin \frac{\beta}{2} - y \cos \frac{\beta}{2} - \frac{x^2 + y^2}{2R_{r0}} + \frac{(x \sin \frac{\beta}{2} + y \cos \frac{\beta}{2})^2}{2R_{r0}} k_3(\alpha_1, \alpha_2) \right] (\cos \alpha_2 - \cos \alpha_1), \quad (6.19)$$

and

$$k_1(\alpha_1, \alpha_2) = \cos^3 \alpha_1 - \cos^3 \alpha_2, \quad (6.20)$$

$$k_2(\alpha_1, \alpha_2) = 1 - \sin^2 \alpha_2 - \sin^2 \alpha_1 - \sin \alpha_2 \sin \alpha_1, \quad (6.21)$$

$$k_3(\alpha_1, \alpha_2) = \cos^2 \alpha_1 + \cos \alpha_1 \cos \alpha_2 + \cos^2 \alpha_2. \quad (6.22)$$

Therefore, the target altitude z as a function of x, y can be derived by solving the following equation

$$A(\alpha_1, \alpha_2) z^2 + B(x, y, \alpha_1, \alpha_2) z + C'(x, y, \alpha_1, \alpha_2) = 0. \quad (6.23)$$

where

$$C'(x, y, \alpha_1, \alpha_2) = C(x, y, \alpha_1, \alpha_2) - \frac{\Delta \phi(x, y, \alpha_1, \alpha_2)}{2\pi} \lambda. \quad (6.24)$$

It can be shown that the physically valid value of the altitude $z(x, y)$ is obtained from

$$z(x, y) = \frac{-B + \sqrt{B^2 - 4AC'}}{2A} \quad (6.25)$$

For typical microwave imaging geometries, it is possible to further simplify the above solution, as discussed in the following.

Far-Field Imaging

In radar imaging, we have $\alpha_2 = \alpha_1 + \Delta\alpha$, where $\Delta\alpha$ is an increment of the depression angle, and the Nyquist sampling theorem requires that $\Delta\alpha \leq \frac{\lambda}{2D}$. It is easy to show that, in Eqs.(6.20-6.22), we have $|k_1(\alpha_1, \alpha_1 + \Delta\alpha)| \leq \frac{2}{\sqrt{3}}\Delta\alpha$, $-2 \leq k_2(\alpha_1, \alpha_1 + \Delta\alpha) \leq 1$, and $0 \leq k_3(\alpha_1, \alpha_1 + \Delta\alpha) \leq 3$. Therefore, when the conventional far-field condition is satisfied, i.e

$$\frac{D^2}{R_{r0}} \leq \frac{\lambda}{2}, \quad (6.26)$$

all the terms including $1/R_{r0}$ in Eqs.(6.15-6.18) can be ignored without introducing noticeable errors. In this case, the target altitude can be approximated as

$$z_f(x, y) \simeq \frac{1}{B_f(\alpha_1, \alpha_2)} \left[\frac{\lambda}{2\pi} \Delta\phi(x, y, \alpha_1, \alpha_2) - C_f(x, y, \alpha_1, \alpha_2) \right], \quad (6.27)$$

where

$$B_f(\alpha_1, \alpha_2) = \sin \alpha_2 - \sin \alpha_1, \quad (6.28)$$

and

$$C_f(x, y, \alpha_1, \alpha_2) = \left(\frac{R_{r0}}{\cos \alpha_1 \cos \alpha_2} - x \sin \frac{\beta}{2} - y \cos \frac{\beta}{2} \right) (\cos \alpha_2 - \cos \alpha_1). \quad (6.29)$$

Ground Plane Imaging

In this case, the two receiving antennas are symmetrically placed on each side of the ground plane, we have $\alpha_2 = -\alpha_1 = \alpha$, $A(\alpha_1, \alpha_2) = 0$ and $C(x, y, \alpha_1, \alpha_2) = 0$. Thus the target altitude can be calculated by

$$z_g(x, y) = \frac{\Delta\phi(x, y, \alpha)\lambda}{2\pi B_g(x, y, \alpha)} \quad (6.30)$$

where

$$B_g(x, y, \alpha) = \left(2 - \frac{x \sin \frac{\beta}{2} + y \cos \frac{\beta}{2}}{R_{r0}} \cos^2 \alpha \right) \sin \alpha. \quad (6.31)$$

For far-field ground plane imaging, we have

$$B_g(x, y, \alpha) \simeq 2 \sin \alpha. \quad (6.32)$$

6.4.2 Single Antenna Imaging

It should be noted that in above, all the equations are derived from the bistatic imaging geometry, where the transmit antenna is assumed to be located at a fixed position. When the bistatic angle $\beta = 0$ it represents the monostatic case.

There is a unique monostatic imaging configuration where the signals are transmitted and received by a single same antenna, i.e., the monostatic one-antenna imaging case. In this case, the height of the transmit antenna is not fixed but varies with different depression angles, and we have $R_{t1} = R_{r1}, R_{t2} = R_{r2}$. Thus, Eq.(6.12) should be modified by

$$\begin{aligned} \Delta\phi(x, y, \alpha_1, \alpha_2) &= \frac{2\pi}{\lambda}(R_{r1} - R_{r2} + R_{t1} - R_{t2}) \\ &= \frac{4\pi}{\lambda}[R_{r1}(x, y, z, 0) - R_{r2}(x, y, z, 0)] \end{aligned} \quad (6.33)$$

Accordingly, Eqs.(6.24),(6.27) and (6.30) should be replaced by

$$C'(x, y, \alpha_1, \alpha_2) = C(x, y, \alpha_1, \alpha_2) - \frac{\Delta\phi(x, y, \alpha_1, \alpha_2)}{4\pi}\lambda, \quad (6.34)$$

$$z_f(x, y) = \frac{1}{B_f(x, y, \alpha_1, \alpha_2)}\left[\frac{\lambda}{4\pi}\Delta\phi(x, y, \alpha_1, \alpha_2) - C_f(x, y, \alpha_1, \alpha_2)\right], \quad (6.35)$$

and

$$z_g(x, y) = \frac{\Delta\phi(x, y, \alpha)\lambda}{4\pi B_g(x, y, \alpha)}, \quad (6.36)$$

respectively.

6.5 Image Formation Issues

Up to this point, we have mathematically related the target altitude to the phase difference of the 2-D ISAR images. In this section, we discuss several issues special for 3-D IF-ISAR

image formation of man-made targets.

6.5.1 Data Collection Constraints

Two different ISAR images can be obtained in a number ways. In the implementation of IF-ISAR imaging, there are several data collection issues to be considered.

The first issue we need to consider is whether to use two-antenna or one-antenna ISAR interferometry. This is in fact equivalent to the so called one-pass or two-pass interferometry in IF-SAR, respectively, IF-ISAR usually requires higher resolution and thus requires much more dedicated data collection and signal processing. Besides, a man-made fluctuating target usually exhibits very different signatures even if the imaging system geometry has only a slight variation. As a consequence, to ensure better interferometry and higher accuracy of the altitude images, the two-antenna configuration is preferred. However, it is possible to form target altitude image using the one-antenna configuration, as will be shown in section 6. Furthermore, a two-antenna ground plane imaging configuration will always result in better accuracy than a slant plane configuration. Therefore, for diagnostic imaging, two-antenna ground plane configuration is recommended as the first choice.

Second, due to the difficulty of phase unwrapping in IF-ISAR processing, it is necessary to configure the imaging geometry to ensure that the phase difference between each pixel in the two ISAR images is restricted to $[-\pi, +\pi]$. This requires that the two antennas be configured so that the Nyquist sampling theorem is satisfied, i.e.

$$\Delta\alpha = \tan^{-1} \frac{h_2}{R_{r0}} - \tan^{-1} \frac{h_1}{R_{r0}} \leq \frac{\lambda_{min}}{2D} \quad (6.37)$$

where λ_{min} is the shortest radar wavelength. This in fact is the same as the sampling rate requirement in conventional 3-D imaging.

6.5.2 Impact of Multiple Scattering Centers

Notice that the present IF-ISAR 3-D imaging system model implicitly assumes that there exists only a single scattering center at each position (x, y) with altitude $z(x, y)$. This cannot be always true for a real-world complex target. Thus we have to investigate the

effect of multiple scattering centers at the position (x, y) with different altitudes $z_k(x, y), k = 1, 2, \dots, M$, on the IF-ISAR altitude image.

We assume that there are M scattering centers at the pixel (x, y) , where the magnitude, original phase and altitude of the i th scattering center are σ_k, δ_k and z_k , respectively, as is shown in Figure 6.2. Recall that from Eq.(6.8), a 2-D ISAR image $\hat{f}_z(x, y)$ represents the reconstruction of the axis-integrated 3-D scattering function $f(x, y, z)$ at plane $z = 0$. For simplicity and without loss of generality, we consider the far-field imaging case. The distance between the i th ($i = 1, 2$) receiving antenna and the k th scattering center can be approximated as

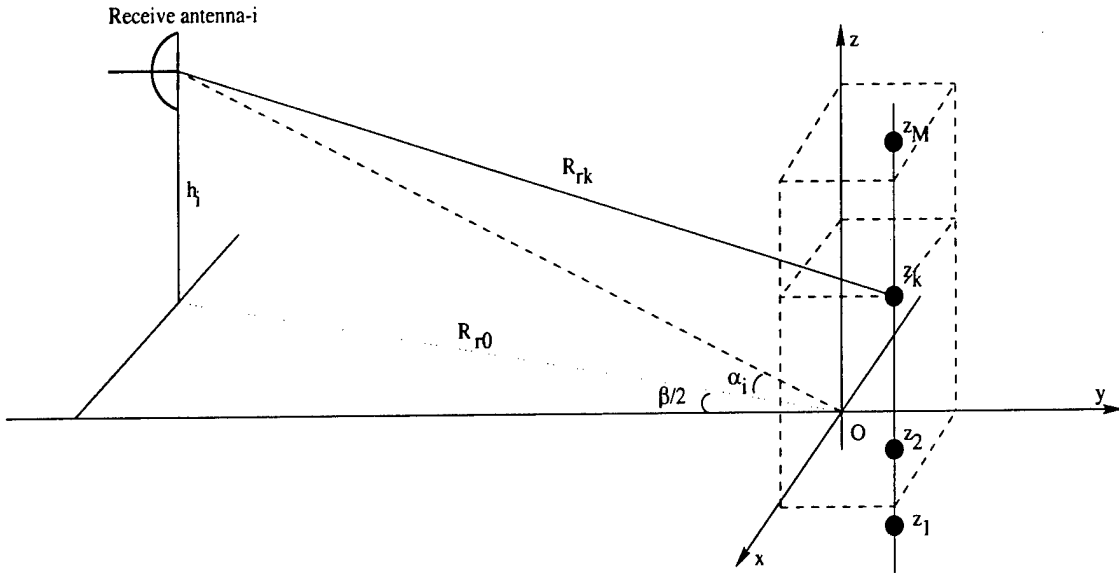


Figure 6.2: Multiple scattering centers at position (x, y) .

$$R_{ik} \simeq \frac{R_{r0}}{\cos \alpha_i} - (x \sin \frac{\beta}{2} - y \cos \frac{\beta}{2}) \cos \alpha_i - z_k \sin \alpha_i. \quad (6.38)$$

The axis-integrated scattering function of the M scattering centers can then be expressed as

$$f(x, y) = \sum_{k=1}^M \sigma_k \exp[j \frac{2\pi}{\lambda} R_{ik} + \delta_k] = \sigma_{ei} e^{j\Phi_{ei}} \quad (6.39)$$

Eq.(6.39) implies that the M scattering centers can be considered to be an equivalent single scattering center at position (x, y) . The magnitude of this equivalent scattering center can be expressed as

$$\sigma_{ei} = \sqrt{\sum_{k=1}^M \sum_{l=1}^M \sigma_k \sigma_l \cos\left[\frac{2\pi}{\lambda}(z_k - z_l) \cos \alpha_i + \delta_k - \delta_l\right]} \quad (6.40)$$

which is dependent on σ_k , δ_k , z_k and the depression angle α_i .

The phase of the integrated signals from the M scattering centers is

$$\Phi_{ei} = \frac{2\pi}{\lambda} \left[\frac{R_{r0}}{\cos \alpha_i} - \left(x \sin \frac{\beta}{2} - y \cos \frac{\beta}{2} \right) \cos \alpha_i \right] - \tan^{-1} \frac{V_{Mi}}{U_{Mi}} \quad (6.41)$$

where

$$U_{Mi} = \sum_{k=1}^M \sigma_k \cos\left(\frac{2\pi}{\lambda} z_k \sin \alpha_i - \delta_k\right), \quad (6.42)$$

$$V_{Mi} = \sum_{k=1}^M \sigma_k \sin\left(\frac{2\pi}{\lambda} z_k \sin \alpha_i - \delta_k\right). \quad (6.43)$$

The first term in Eq.(6.41) is independent of the M scattering centers. Thus we can study the second term in Eq.(6.41) only. Rewrite this term as

$$\Phi_i = \tan^{-1} \frac{V_{Mi}}{U_{Mi}}, \quad (6.44)$$

which can be considered to be the equivalent original phase of the M scattering centers at position (x, y) . The altitude image is derived from the phase difference between two ISAR images, where we assume that the original phase of each scattering center is invariant as the depression angle changes. Unfortunately, it is found from Eq.(6.44) that the equivalent original phase is not only a function of σ_k , δ_k and z_k , but also dependent of the depression angle α_i .

To study the impact of the equivalent original phase Φ_i on the IF-ISAR altitude image, we can study the phase gradient as a function of the depression angle α_i . This phase gradient can be shown to be

$$\frac{\partial \Phi_z}{\partial \alpha_i} = \frac{\frac{2\pi}{\lambda} \sum_{k=1}^M \sum_{l=1}^M z_l \cos \alpha_i \sigma_k \sigma_l \cos\left[\frac{2\pi}{\lambda}(z_k - z_l) \cos \alpha_i + \delta_k - \delta_l\right]}{\sigma_{ei}^2}. \quad (6.45)$$

From Eq.(6.45), it is readily apparent that a very small equivalent scattering magnitude may lead to a very large phase gradient, thus destroying the interferometry of the two images. From the viewpoint of monopulse radar, this is just the well-known target glint phenomenology. This target glint, or phase scintillation, may severely contaminate the IF-ISAR altitude images, thereby confounding the interpretation of the images.

Fortunately, in radar imaging applications, our major interests are on the stronger scattering centers. By thresholding the altitude image according to the scattering magnitude at the corresponding pixels in the 2-D ISAR images, the impact of the glint can be greatly reduced. Furthermore, Borden [76, 92] has shown that, the above phase gradient statistics is proportional to the target extent in altitude. Recall that the IF-ISAR altitude image is derived from two 2-D ISAR images. A single frame of such a 2-D image is reconstructed from the data collection as a function of frequency and azimuthal angle. The image reconstruction is equivalent to perform a weighted average processing. This diversity processing also greatly reduces the phase scintillation [93]. Therefore, when there are multiple scattering centers with different altitudes in one pixel, the altitude image is expected to reflect the equivalent altitude of the M scattering centers, as long as its equivalent scattering magnitude is not too small.

Other image formation issues include image registration, consideration of the imaging plane, target layover, and so on. A discussion of these issues for spotlight SAR can be found in [86]. We point out that these issues have no severe impact on IF-ISAR imaging. Besides, as was mentioned in [84], the target altitude image can be in turn, applied to correct the target layover position errors in the 2-D ISAR images, in both down range and cross range dimensions. We also point out that in this study, we assume that for non-cooperate maneuvering target, exact motion compensation was made before the 3-D interferometric processing. In the case of no exact motion compensation available, the processing will become much more sophisticate.

6.6 Experimental Results

To demonstrate the feasibility and to study the accuracy of the 3-D IF-ISAR image processing technique, both simple and complex targets were imaged. These include the image formation of target signature data from computational electromagnetic scattering codes, anechoic chamber measurements, and outdoor range tests. In all cases, a backprojection algorithm was applied to the 2-D ISAR image reconstruction. A 2-D Hamming window function was used to suppress the artifacts in the images. A computational electromagnetic scattering example can be found in [94]. In this section, we provide some altitude image formation examples from indoor and outdoor range measurements of complex targets.

6.6.1 Two-Antenna Ground Plane Imaging

A ground plane 3-D imaging geometry was configured in the anechoic chamber compact range at Beijing Institute of Environmental Features (BIEF). To realize the 3-D IF-ISAR imaging, two antenna feeds at different altitudes were used. In this configuration, one of the feeds transmits wideband signals, and both of the feeds receive the target echoes simultaneously. The imaging parameters are as follows: central frequency $f_0 = 9.25$ GHz, bandwidth $B_w = 1.8$ GHz, azimuthal angle range $[-6^\circ, +6^\circ]$, depression angle $\alpha = 0.2^\circ$, and the radar distance $R_t = R_r = 12.0$ m.

The altitude images of simple targets consisting of one or two metal spheres were first studied. We found in these cases the accuracy of the reconstructed altitudes of the scattering centers was better than 2 cm, roughly half of the radar wavelength.

A 3-D altitude image formation was also performed on a complex aircraft model. Figure 6.3 illustrates the 2-D ISAR and 3-D IF-ISAR altitude images of the aircraft model, where Figure 6.6.1 (a) and (b) are the two 2-D ISAR images. The two ISAR images exhibit very good correlation, as they were obtained simultaneously by two antennas. Figure 6.3 (c) is the corresponding IF-ISAR altitude image. With the altitude image, we note that it is now much easier to relate each scattering center to the target physical structures. It also provides us the following additional information: (1) The aircraft model was not placed on a horizontal level surface. By comparing the altitude values of the scattering center pairs

1,1' or 2,2' (as in Figure 6.3 (a)), it is easy to estimate that there is a roll angle of about 10° for the model. (2) The scattering center 3 in the 2-D ISAR images is in fact composed of 4 scattering centers at different altitudes.

6.6.2 Slant Plane Imaging

The 3-D IF-ISAR image processing algorithm was also applied to the public release ISAR phase history data of the T-72 tank, a very complex target. The signature data were acquired by Georgia Tech Research Institute's Electromagnetic Test Facility [84]. This is a single antenna imaging configuration, i.e., the data at different depression angles were acquired at different times. The imaging parameters are as follows: central frequency $f_0 = 9.6$ GHz, bandwidth $B_w = 0.66$ GHz, azimuthal angle range $[0 - 360^\circ]$, depression angle range $[27.9909 - 31.9334^\circ]$, and the radar distance is $R_r = R_t = 45.8$ m. The data sampling rates are: frequency increment 3 MHz, azimuthal angle increment 0.05° , and depression angle increment 0.138° . For each frame of ISAR image processing, the achievable azimuthal angle range is $[-1.95^\circ, +1.95^\circ]$.

Figure 6.4 shows an example of the 2-D ISAR images (Figure 6.4(a) and (b)) and the corresponding IF-ISAR altitude image (Figure 6.4(c)) of the T-72 tank. In this example, the two ISAR images exhibit greater decorrelation than those seen in Figure 6.6.1. Apart for the increased complexity of the target scattering structure, the single antenna imaging configuration may also be responsible for this decorrelation.

In addition to the information provided on the heights of individual scattering centers on the target, the altitude image also provides some additional important information. For example, according to the altitude image, the scattering center denoted by 1 (as in Figure 6.4(a)) is about 200 cm below the cannon, thus making it easy to study the scattering mechanism of this scattering center. More important, the altitude image not only makes it much easier to distinct the zero-Doppler clutter outside the target body [84] from the true scattering centers on the target, but also tells us those scattering centers contaminated by the zero-Doppler clutter.

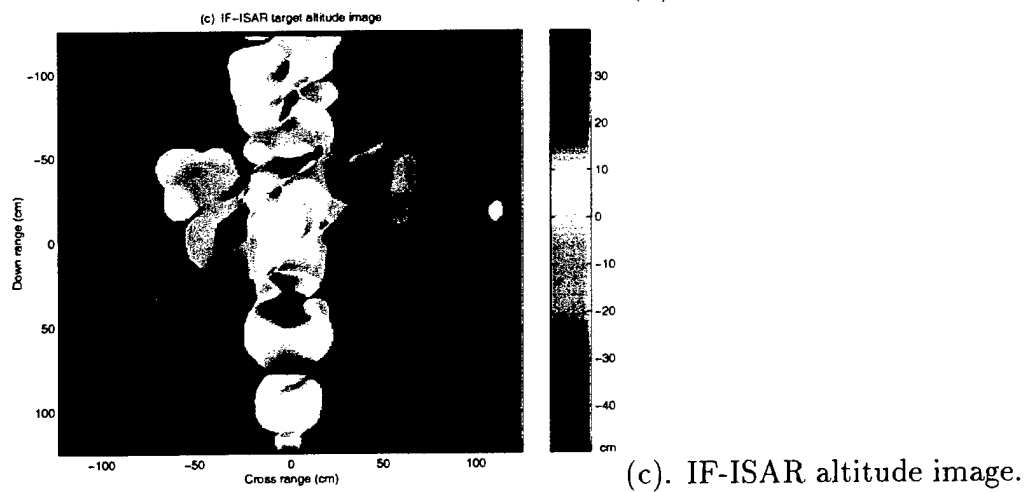
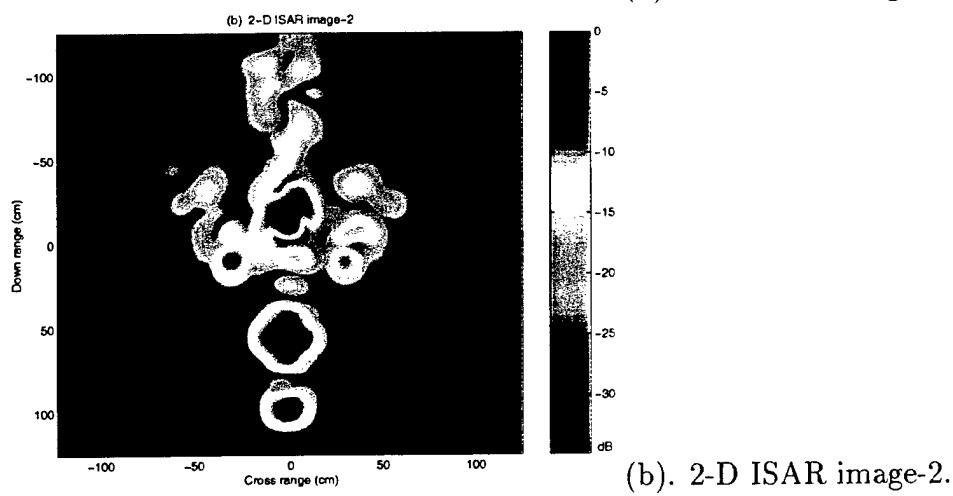
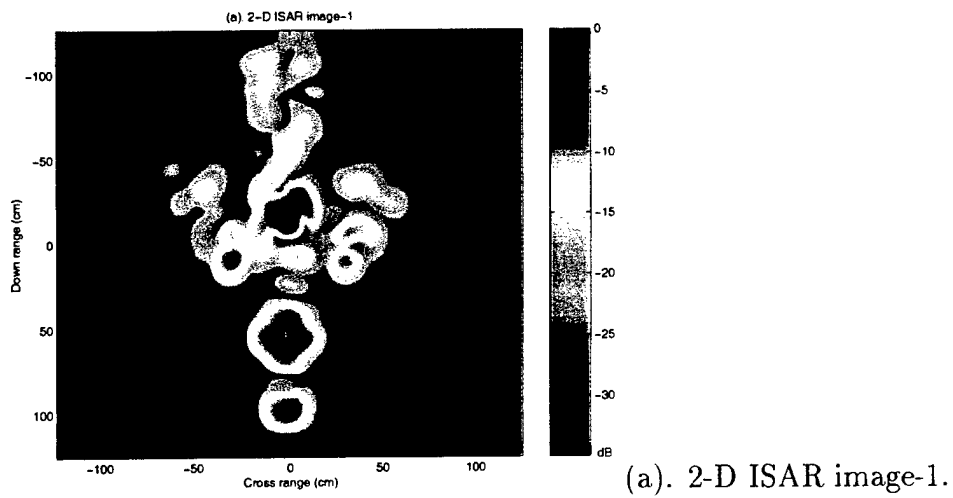
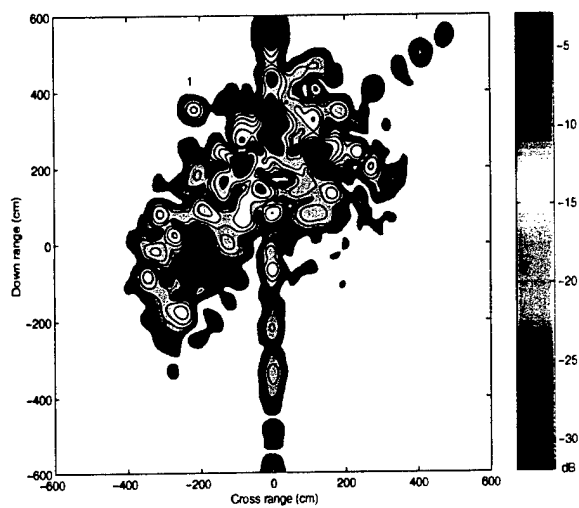
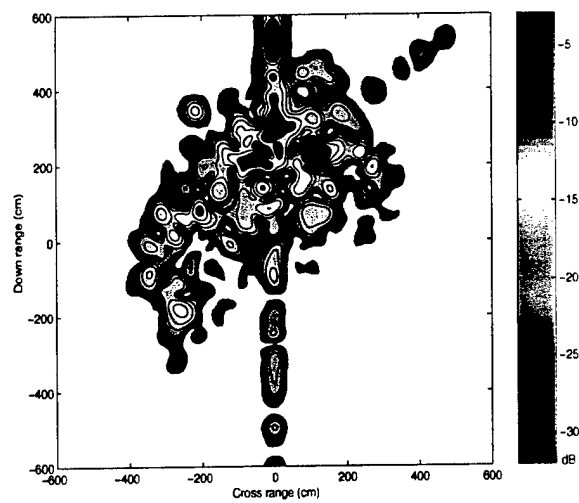


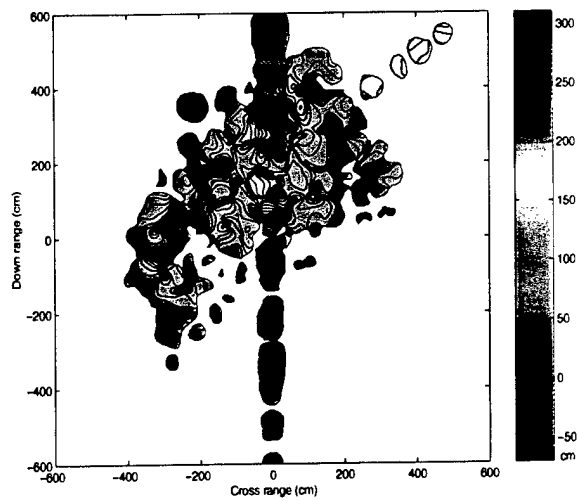
Figure 6.3: Images of a scaled aircraft model.



(a) 2-D ISAR image-1.



(b) 2-D ISAR image-2.



(c) IF-ISAR altitude image.

Figure 6.4: Images of a T-72 tank.

6.7 Summary

3-D radar images give us the information of the scattering magnitudes as well as the 3-D positions of the scattering centers on a complex target. A conventional 3-D ISAR system measures the coherent backscattering signals of a target as a function of frequency, azimuth and elevation angles, thus resulting in great data collection and computation burdens. In the present paper, a IF-ISAR target altitude image formation technique is developed. This technique uses only two frames of 2-D ISAR images to derive an altitude image, thus simplifying the data collection and signal processing, while resulting in promising target altitude images. Applications of this technique can be found in radar target identification, scattering diagnosis and target modeling, and so on.

Chapter 7

EXPERIMENTAL RADAR SYSTEM AND TESTS RESULTS

7.1 Brief Description of the Experimental UWB Random Noise Radar

A block diagram of the polarimetric coherent UWB random noise radar system is shown in Figure 7.1. This system has been designed specially for foliage penetration surveillance applications.

The noise signal is generated by the noise oscillator, which provides a wideband noise signal with a Gaussian amplitude distribution and a constant power spectral density (PSD) in the 20-600 MHz frequency range, with a power output of +10 dBm. This signal is then fed to a band-pass filter which has a pass band of 250-500 MHz. The output of the band-pass filter is split into two equal in-phase components in power divider PD1. One of these outputs is amplified in a broadband power amplifier, which has a 1 dB gain compression point greater than +47 dBm. Thus, the average power output of AMP1 is +40 dBm, but the amplifier is capable of faithfully amplifying noise spikes that can be as high as 7 dB above the mean noise power. The output of the amplifier is connected to a dual-polarized broadband log-periodic transmit antenna. The log-periodic antenna, in addition to being broadband, has desirable features such as a constant gain with frequency, and superior cross-polar isolation.

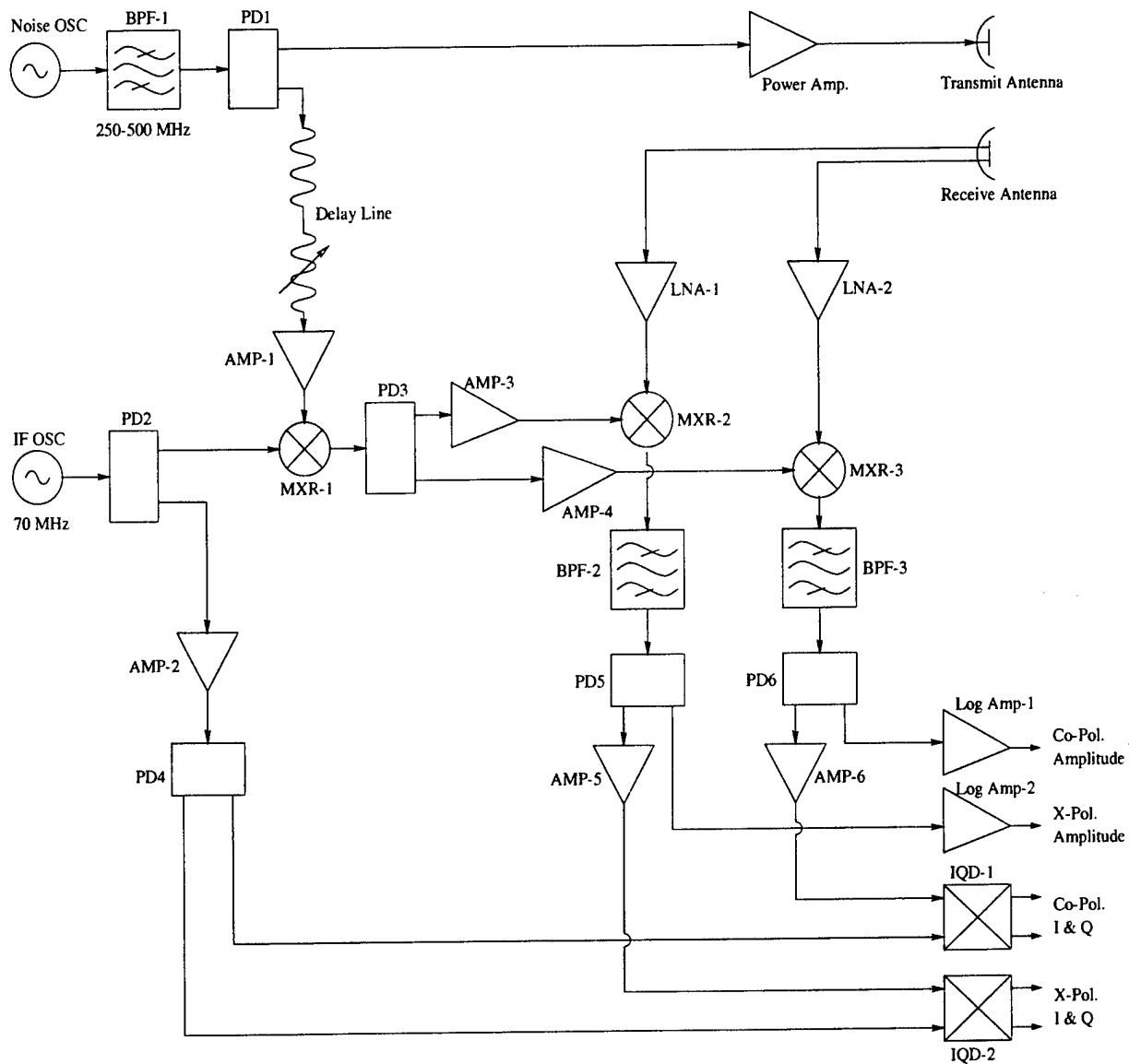


Figure 7.1: Block diagram of the FOPEN random noise radar system

The other output arm of the power divider PD1 is connected to a combination of a fixed and variable delay lines. These delay lines are used to provide the necessary time delay for the sampled transmit signal so that it can be correlated with the received signal back scattered from objects at the appropriate down range corresponding to the delay. Range scanning is performed using a 7-bit coaxial cable delay lines that can be stepped from 0-127 nsec in steps of 1 nsec. The variable delay line can be rapidly programmed to step through the entire range of 19.05 m, so that various probing down range values can be obtained.

In order to perform coherent processing of the noise signals, a unique frequency translation scheme is proposed. The primary component of this technique is a 70 MHz phase-locked oscillator. This is connected via a power divider PD2 to the intermediate frequency (IF) input terminal of MXR-1. The output of MXR-1 is the lower sideband of the mixing process, which lies within the 180-430 MHz frequency range. This coherent noise signal is split by power divider PD3 into two channels: the co-polarized and cross-polarized channels. Also the second output of the power divider PD2 is amplified and again split into two 70 MHz signals in power divider PD4.

We will now discuss the signal processing of the co-polarized channel. The cross-polarized channel operation is essentially identical, so it will not be repeated. One of the outputs of PD3 is amplified and then used as the local oscillator (LO) input to a mixer MXR-3, whose RF input is obtained from the co-polarized channel of the receive antenna and a low noise amplifier LNA-2. The receive antenna is identical to the transmit antenna. LNA-2 is used to improve the noise figure at the receiver input, which has a noise figure of 1.4 dB, gain 30 dB, and maximum output +5 dBm. In general, the RF input signal to the mixer MXR-2 consists of noise signal at 250-500 MHz scattered from various objects and interferences. However, since the LO signal has a unique delay associated with it, only the signal scattered from the appropriate down range bin will mix with the LO to yield a IF signal at a frequency of exactly 70 MHz. The output of MXR-3 is connected to a narrowband bandpass filter BPF-3 of center frequency 70 MHz and bandwidth 35 kHz -5 MHz. MXR-3 together with BPF-3 serves as the cross-correlator of the received and the reference signals. The choice of the bandwidth of BPF-3 determines the correlation integration period of the correlator. The output of filter BPF-3 is split into two outputs in power divider PD6. One of these

outputs is amplified and detected in a 70 dB dynamic range logarithm amplifier Log Amp-1. The other output of the power divider PD6 is connected to one of the inputs of an in-phase/quadrature-phase (I/Q) detector IQD-1, whose reference input is one of the outputs from PD4. Both of the signals are exactly at 70 MHz; thus the I/Q detector provides the in-phase (I) and quadrature-phase (Q) components of the phase difference between the two signals. Since frequency translation preserves phase differences, the I and Q outputs can be related to the polarimetric co-polarized scattering phase history characteristics of the foliage obscured objects or interferences.

In a similar fashion, the cross-polarized channel is simultaneously processed using biasable mixer MXR-2, bandpass filter BPF-2, power divider PD5, logarithmic amplifier Log Amp-2, and I/Q detector IQD-2.

The system therefore produces the following outputs at various down range as set by the delay lines: (a) Co-polarized amplitude, (b) Co-polarized phase angle, (c) Cross-polarized amplitude, and (d) Cross-polarized phase angle.

Thus, the system outputs can be related to the fully polarimetric scattering characteristics of the targets.

7.2 Performance Analysis of the FOPEN UWB Random Noise Radar System

The technical specifications of the FOPEN UWB random noise radar system are summarized in Table I.

Table I. FOPEN UWB Random Noise Radar System Specifications

Parameter	Specification
Transmitter:	
Operation frequency band	250-500 MHz
Down range resolution	60 cm
Transmit Waveform	Continuous Gaussian Noise
Transmit Power (Max.)	50 W (47 dBm)
Receiver:	
System IF	70 MHz
Sensitivity	-80 dBm
Dynamic range	70 dB
Variable delay time	0 - 127 ns in 128 steps of 1 ns
Antennas:	
Antenna type	Log Periodic
Frequency band	200 - 1000 MHz
Gain	6 dBi
3-dB Beamwidth	45° E-Plane and 90° H-Plane
Polarization	Dual Polarized (Vertical and Horizontal)

7.2.1 System PSF and the down range resolving capability

The typical down range PSF for the two channels of the noise radar system are shown in Figure 7.2. The number of integrated echo samples is 1024 in this figure.

It is seen from Figure 7.2 that, the 3-dB width of the mainlobe is about 4 ns or 60 cm, which is coincident with the theoretical prediction using equation (2.24), where when $B = 250$ MHz, we have $\delta_R = 60$ cm.

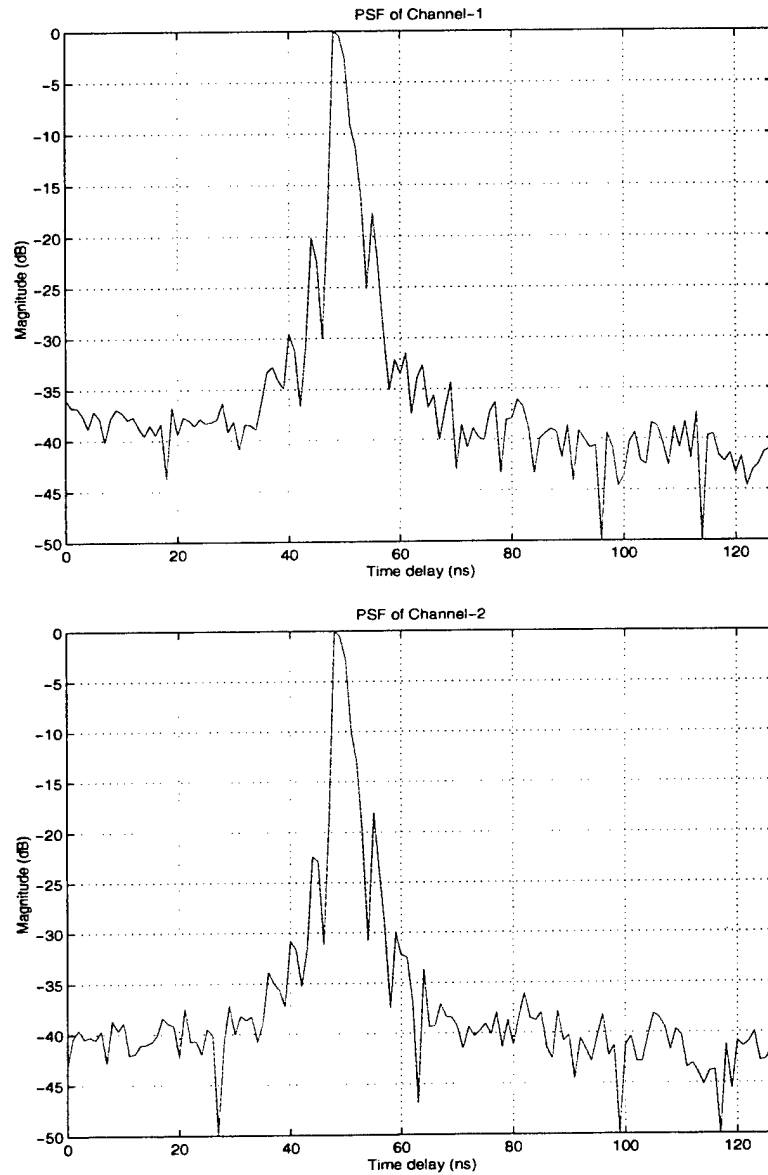


Figure 7.2: PSF of the FOPEN random noise radar system, channel-1 (above) and channel-2 (below).

7.2.2 System dynamic range and sensitivity

In Figure 7.3, we present the noise radar system responses at different input power levels. To do so, we keep the output power of the noise source at a constant level of 0 dBm, and change input power level of the receiver by using attenuators with different attenuation values. Figure 7.3 illustrates the PSFs with input attenuation values at 0, 20, 40, 60 70 and 80 dB, respectively.

It is seen from Figure 7.3 that the dynamic range of the noise radar system is better than 70 dB, while the sensitivity is about -80 dBm.

7.2.3 Impact of the number of integrated echo samples

One of the important considerations for random noise radar is that there must be an integration of multiple returned echoes for a reasonably accurate measurement.

Figure 7.4 demonstrates the impact of the numbers of integrated echo samples on the PSF of the noise radar system, where the PSFs with numbers of integrated echo samples 8, 32, 128, 512, 1024 and 4096, respectively, are shown. The PSF of the system is close to a sinc function (which corresponding to a rectangular window). The sidelobes of the sinc-like PSF can be suppressed by using an apodization filter, as discussed in Chapter 3. In addition to the sidelobes of the sinc-like function, there also exists residual sidelobes in the PSF of the noise radar system, caused by the randomness of the radar waveform. A random noise radar must, therefore, ensure adequate averaging by integration of a number of echo samples to reduce the residual sidelobes. From Figure 7.4, when the number of integrated echo samples is small, the residue sidelobe level is relatively high. For example, when with the numbers of integrated echo samples 8 and 32, the residual sidelobe levels are around -15 dB and -25 dB, respectively. However, when with a number of integrated echo samples larger than 512, the residual sidelobe level can be lower than -35 dB.

As a comparison, the results in Figure 7.4 can be compared to the simulation results in Figure 4.7. The measured residual sidelobe levels in Figure 7.4 are coincident with the simulation results in Figure 4.7. This figure shows that with an adequate number of integrated echo samples (e.g, 512-4096), it is possible for the noise radar to yield images of

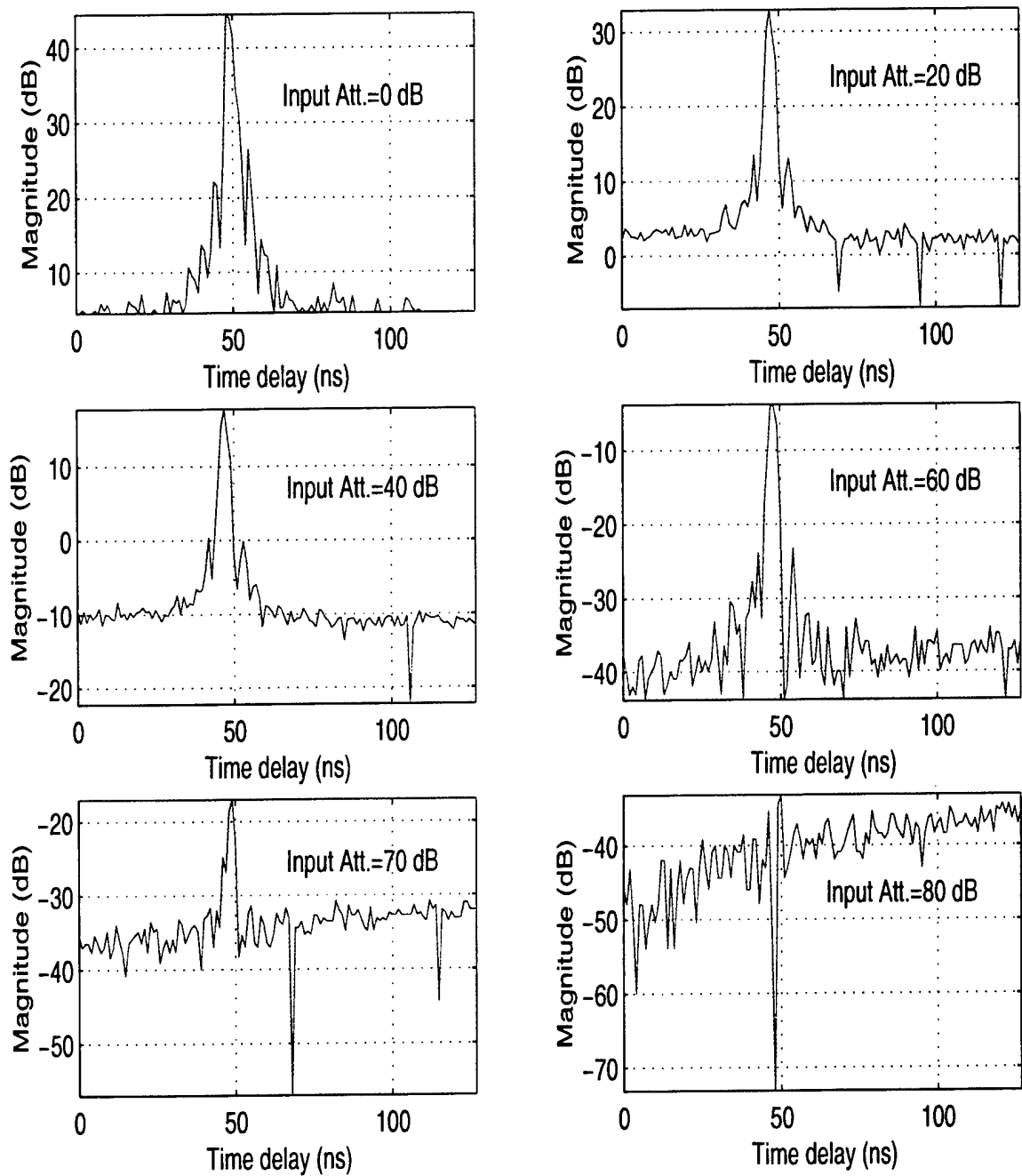


Figure 7.3: System responses at different input power levels

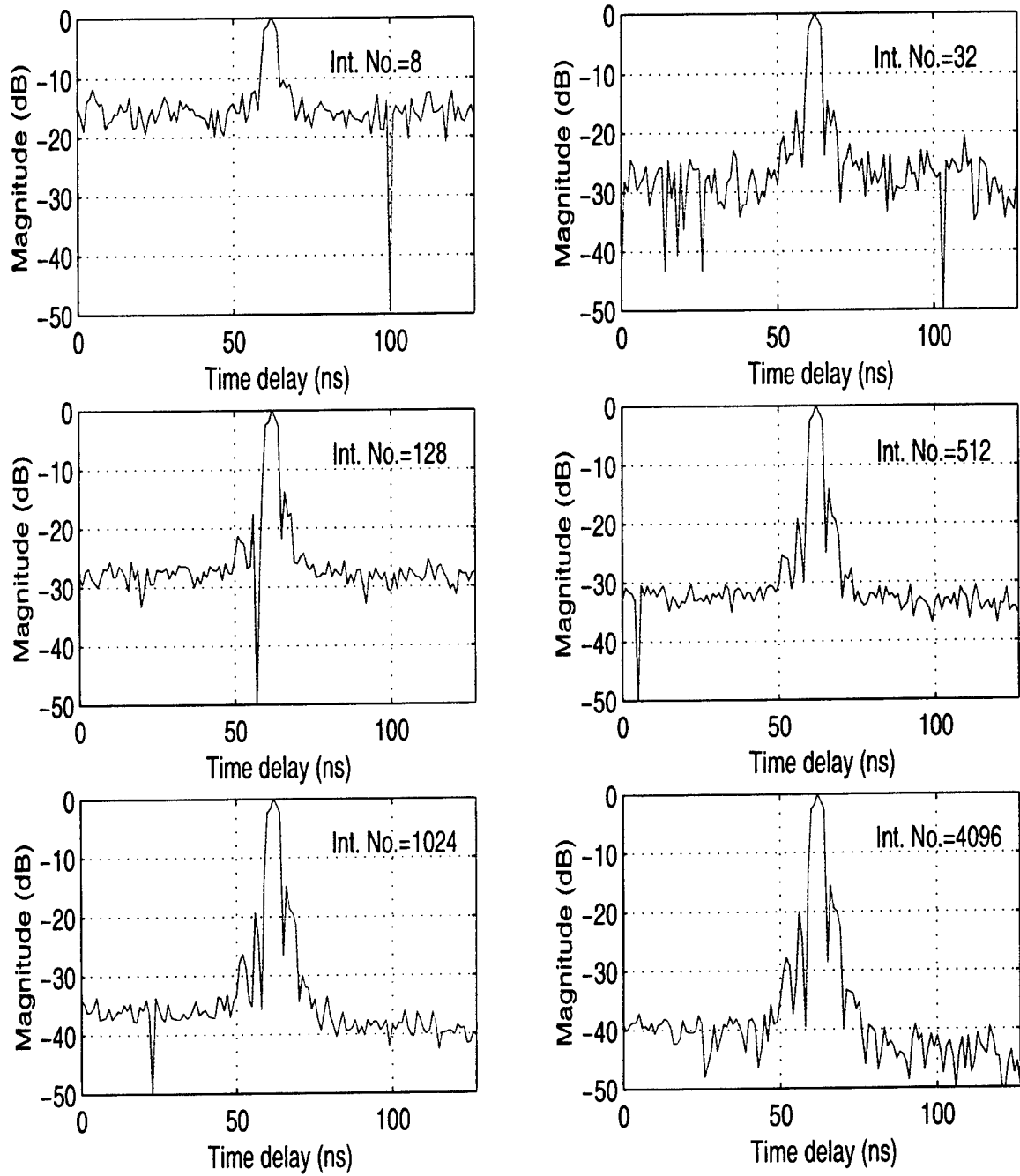


Figure 7.4: System responses for different numbers of the integrated echo samples.

quality as good as a UWB radar using step-frequency or linear frequency modulation (LFM) waveforms.

7.3 Field Test Results

To demonstrate the high resolution and foliage penetration capabilities of the experimental UWB random noise radar system, and to test the imaging algorithms, a variety of field tests were conducted. In this section, we present part of the results.

7.3.1 SAR Imaging on Unobscured Targets

To demonstrate the 2-D high resolution SAR imaging capability of the UWB random noise radar system, we first image unobscured targets sitting on open air ground.

A boom van was used as the platform for the noise radar imaging system. The radar system was placed in the boom van. Two Log periodic antennas were installed on the boom which can rise to about 10 meters above the ground. The two antennas were isolated using a large metal plate so that the coupling between the transmitter and the receiver is reduced. This boom van-mounted UWB random noise SAR system configuration is shown in Figure 7.5.

An additional 50 m of low-loss cable was added to the time delay chain to provide a longer fixed delay. The major objectives to use this fixed length cable are to compensate the two-way transmission length (by cables) between the radar and the antennas, and to set a reference center of the equivalent range gate. The fixed length cable, together with the variable delay line provides a range gate of 19.2 m centered at a distance of about 20 m from the radar antennas.

Figure 7.6 illustrates the co-polarization and cross-polarization images of a trihedral reflector and a van. The hypotenuse of the trihedral is 125 cm. The trihedral was placed on a small cart. In this example, horizontal polarization is used for transmit, while both horizontal and vertical polarized echoes are received and processed. It can be seen that both the trihedral and the van are well resolved in the images.

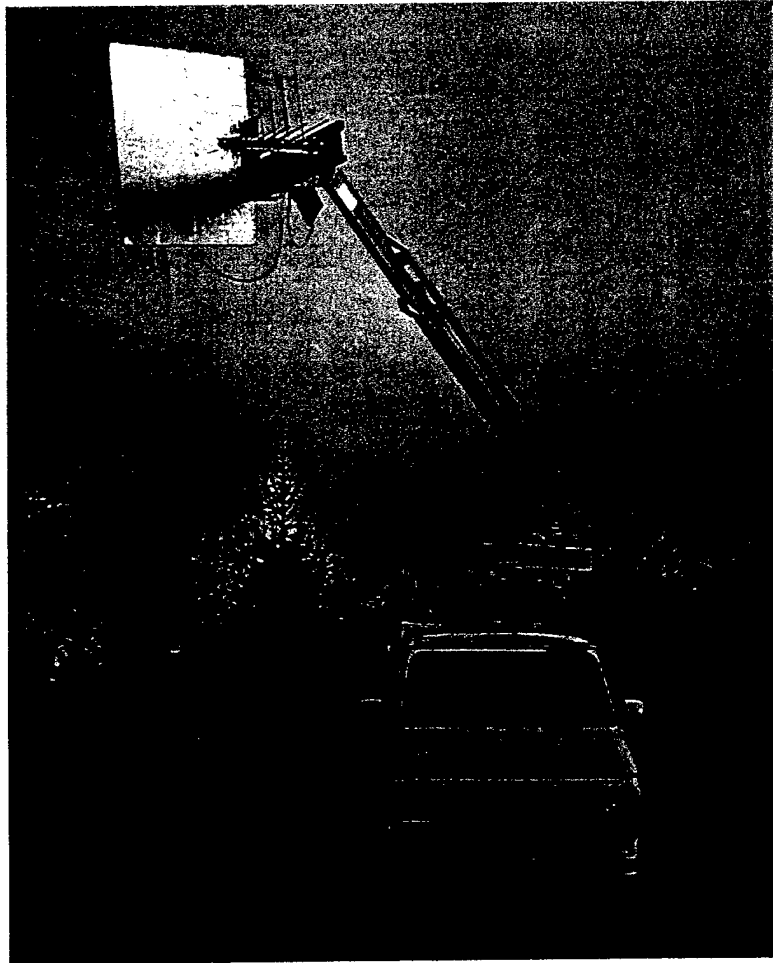


Figure 7.5: The boom van-borne random noise SAR system.

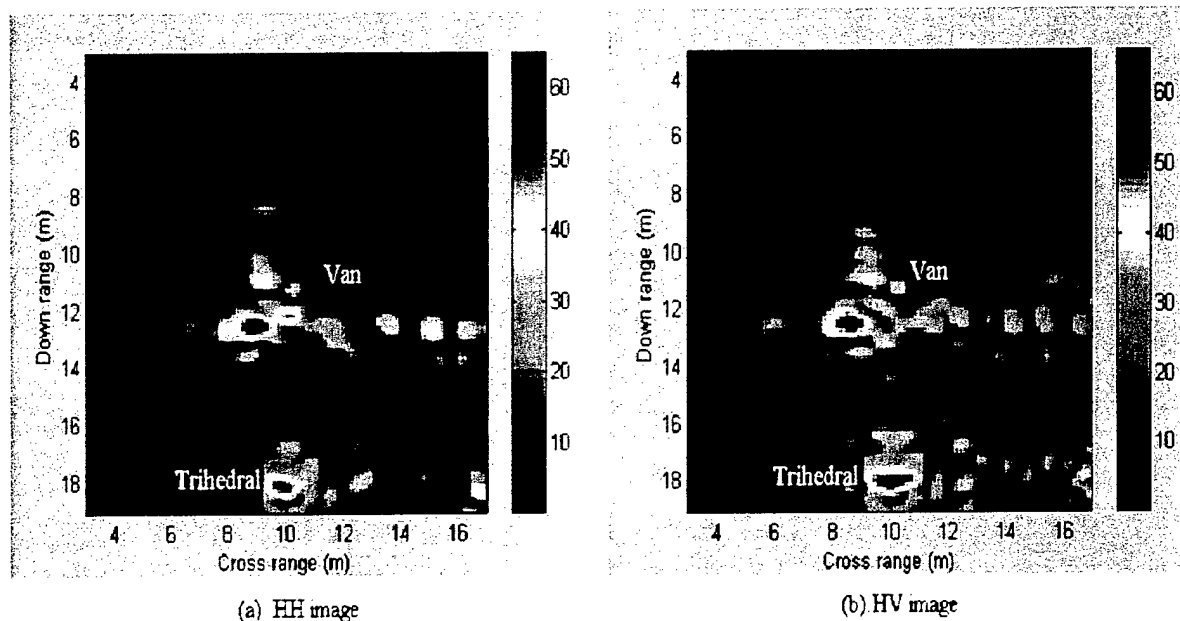


Figure 7.6: 2-D SAR images of a trihedral and a van in open air.

7.3.2 SAR Imaging on Obscured Targets

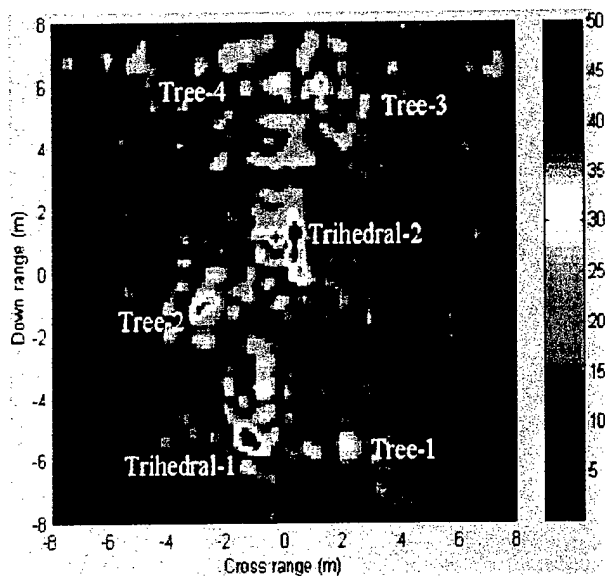
In this study, we made two different tests: foliage penetration and wall penetration tests.

The experimental setup for foliage obscured target imaging is the same as in the former experiment. However, in this case, the targets were placed under fully foliated trees. Figure 7.7 shows the foliage obscured target area and the 2-D SAR image of two trihedral reflectors with hypotenuse of 173 cm. It is seen that both the trihedral reflectors and the separated trees in the target area scenario are all well resolved, thus showing the good foliage penetration capability of the UWB random noise radar system.

To further study the penetrating ability of the radar system on dense medium, we also conducted a wall penetration imaging experiment. In this setup, the radar system operates in an indoor environment, as shown in Figure 7.8(a). The radar system was placed in one room, while a trihedral reflector was placed in another room behind the wall. Other arrangements in the laboratory rooms can also be used as targets. In the experiment, the synthetic aperture was obtained by moving the radar along a straight line path as shown by the arrows in the figure. Figure 7.8(b) shows the resulting image of the wall obscured trihedral reflector and other targets, which demonstrates the good wall penetration imaging capability of the



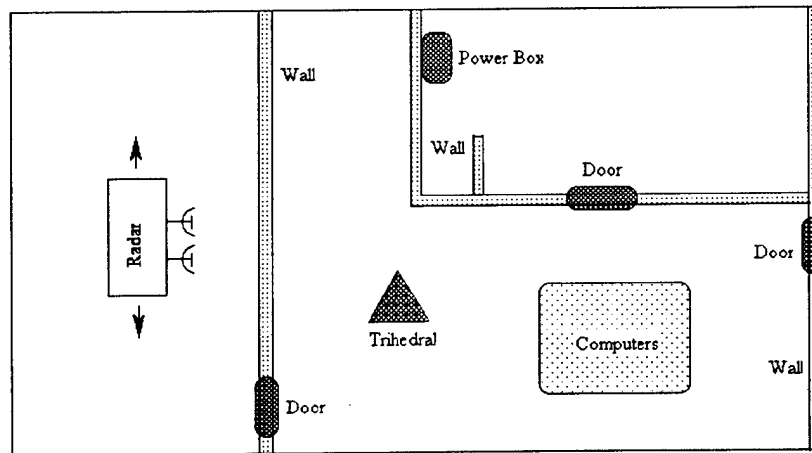
(a). Target area scenario



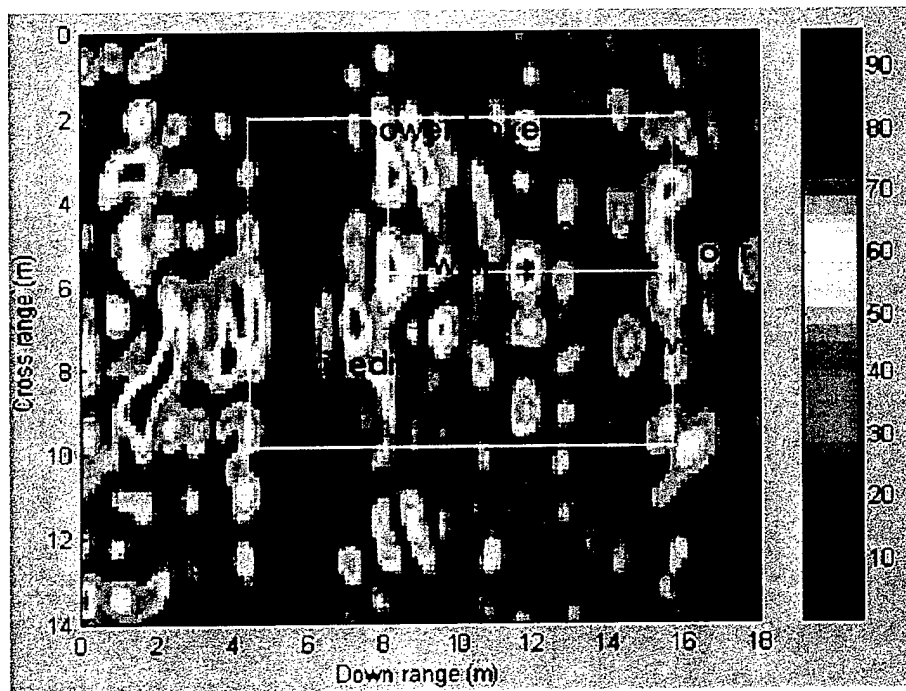
(b). 2-D SAR image, HH Pol.

Figure 7.7: FOPEN random noise SAR image of two trihedral reflectors obscured behind trees.

random noise radar system.



(a) Experiment setup



(b) Wall penetration SAR image

Figure 7.8: Wall penetration SAR image of a trihedral reflector obscured behind wall.

Chapter 8

FOPEN SAR IMAGE ENHANCEMENT

8.1 Background

In SAR or ISAR imaging, conventional Fourier transform (FT) based image reconstruction techniques result images with limited resolution. The down-range and cross-range resolutions of these algorithms are inversely proportional to the radar bandwidth and to the synthetic aperture size, respectively. On the other hand, when modern spectral estimation methods are applied to radar imaging, these nonlinear techniques, usually called super resolution algorithms, offer improved resolution, better contrast, and reduced speckle [95]. Super resolution image processing methods have attracted considerable attention and interests of many researchers. Previous attempts had varying degrees of success.

Bandwidth extrapolation (BWE) is one of the most popular super resolution techniques in radar imaging. In an attempt to achieve the full resolution of the unrestricted spectral range, several methods of linear BWE have been proposed by Gupta [96], Cuomo, Piou and Mayhan [75], and others [97, 98]. BWE uses linear prediction model or its refined version to extrapolate the collected data beyond the observed region, thus results super resolution in images with high signal-to-noise ratios (SNR) or signal-to-clutter ratios (SCR). However, when linear BWE is applied where the SNR or SCR is low, or the target to be imaged is too complex, undesirable image artifacts resulting from the prediction errors in the BWE

images become severe.

Another group of algorithms for super resolution radar imaging includes the application of various parametric spectral estimation methods, such as the total least square (TLS) or maximum likelihood method (MLM) and their variants [99]-[103]. These methods attempt to estimate the amplitudes, phases and locations of the point (or non-point) scatterers to minimize the residual error energy. They usually obtain good results for all the parameters under estimation. But they are also computationally intensive. By combining appropriate target scattering models into the image processing, some more efficient algorithms were developed by Tu *et. al.*[100] and Li *et. al.* [101]-[103].

A third group of the super resolution radar imaging approaches is based on the so-called adaptive beamforming techniques. All the methods in this group attempt to enhance or attenuate the signals from a given source location by finding a set of spatial filter coefficients adaptive to the collected target data. These techniques can be further categorized into two subgroups. The first subgroup consists of those which use the covariance matrix estimated from the target phase history data, such as Capon's minimum variance method (MVM) or its variants [95, 104, 105], the 2-D MUSIC algorithms by Odendaal *et al.* [106], and so on. Some successful examples include Benitz's high-definition vector imaging (HDVI) technique [104, 109, 74] and the amplitude and phase estimation (APES) approach by Li *et. al.* [107, 108].

The second subgroup of these techniques applies a space-variant, symmetric, noncausal finite impulse response (FIR) filter to the sinc impulse response (IPR) images, in an attempt to perform sidelobe nulling without first computing a covariance matrix. This subgroup includes the adaptive sidelobe reduction (ASR) method by DeGraaf [110], and the spatially variant apodization (SVA) and super SVA methods [112, 113], while SVA can be considered to be a special case of ASR with order 1. There are two most favorable advantages of the methods in this subgroup: First, they are highly computationally simple. For an $N \times N$ image, the complexity of applying an order M ASR filter is $O(N^2 M^2)$ (in contrary, the complexity is $O(K^6)$ for MVM and MUSIC, where $K = N/R$, R is the Nyquist interpolation factor)[95]. Second, they provide with interferometric imaging capabilities.

For 2-D SAR imaging, among all the methods mentioned above, SVA is one of the

most attractive techniques due to its computational simplicity. SVA was first proposed by Stankwitz *et al.* [111] as an effective means of reducing sidelobe levels of the sinc IPR in SAR image processing. In conventional FT based radar imaging, the sidelobe reduction is at the cost of broaden mainlobe of the sinc IPR, usually by a factor of 1.6-1.8 if the required sidelobe level is $-30 \sim -40$ dB. Similar to conventional window functions, SVA uses an image location dependent weighting aperture function. Different from the frequency domain weighting in conventional image processing, the SVA algorithm reduces the sidelobes without any mainlobe broadening by using the oscillatory properties of the sinc IPR. Being implemented as a three-point convolution in the image domain, its additional computational complexity is trivial, compared to that of the conventional FT based imaging algorithms. Since SVA keeps the mainlobe of the sinc IPR unchanged while reduces the sidelobes, it is said that SVA has super resolution capability. Stankwitz and Kosek also proposed a super SVA technique to further enhance the image resolution by nonlinear BWE [112, 113].

The discrete implementation of Stankwitz's original version of SVA requires that the data to be sampled at an integer multiple of the Nyquist frequency. If the incoming data are sampled at a noninteger multiple of the Nyquist rate, an upsampling interpolation to an integer rate must be implemented. This becomes the major computational burden when super SVA is applied to 2-D SAR imaging, as at each BWE iteration, an upsampling interpolation must be done before the SVA can be applied. The amount of upsampling is proportional to the desired BWE. To overcome the difficult of such a 2-D interpolation requirement, Smith [114] proposed a formulation by introducing a generalization of SVA to noninteger Nyquist sampling rates. Smith's noninteger Nyquist SVA works well in image sidelobe reduction. However, it is found that, when an iterative super SVA procedure is applied for image resolution enhancement through nonlinear BWE, this method tends to eliminate scatterers with relatively weak amplitudes.

In this chapter, we propose a modified version of noninteger Nyquist SVA. Based on this modified noninteger Nyquist SVA formulation, an iterative super SVA procedure is developed and applied to SAR and ISAR image processing. The remainder of this chapter is organized as follows. A brief review of the SVA, the noninteger Nyquist SVA, and the super SVA techniques is made in the context of image processing in Section 8.2. Based on Smith's

work, we propose a modified version of noninteger SVA in Section 8.3. In Section 8.4, an iterative procedure for SAR/ISAR image enhancement is discussed. Section 8.5 presents two application examples of the iterative super SVA procedure. We summarize the chapter in Section 8.6.

8.2 A Brief Review of SVA and Super-SVA

SVA is based on the idea of using a spatial location dependent aperture function to reduce the IPR sidelobe energy without degrading resolution. It is shown in [115] that SVA is similar in philosophy to Capon's MVM method. In this section, We give a brief review of the one dimensional (1-D) SVA and super SVA in the context of image processing. A 2-D extension is direct and will be discussed in Section 4.

8.2.1 SVA for 1-D image processing

Assume that we are going to reconstruct a 1-D band limited image $g(x)$ from the partial data $G(f)$ of the full spectral range Fourier data $\tilde{G}(f)$ centered at the origin, using a frequency domain cosine-on-pedestal aperture function, $W(f)$. The weighted Fourier spectral data is

$$G_w(f) = G(f)W(f). \quad (8.1)$$

where

$$G(f) = \begin{cases} \tilde{G}(f), & \text{if } f \in [-\Delta, \Delta] \\ 0, & \text{otherwise.} \end{cases} \quad (8.2)$$

and

$$W(f) = 1 + 2\alpha \cos \frac{\pi f}{\Delta}, \quad 0 \leq \alpha \leq \frac{1}{2} \quad (8.3)$$

where α is an adjustable parameter of the weighting aperture. Correspondingly, the reconstructed image can be expressed as

$$g_w(x) = g(x) + \alpha[g(x - X) + g(x + X)] \quad (8.4)$$

where $g(x)$ represents the reconstruction using a rectangular window (i.e., $\alpha = 0$), and $X = \frac{\pi}{\Delta}$.

Eq.(8.4) states that the frequency-domain weighted image reconstruction can be efficiently performed by a three-point convolution in the image domain.

The SVA attempts to find a spatially variant weight α (we denote it by $\alpha(x)$ hereafter to explicitly indicate its spatial position dependence), such that $|g_w(x)|^2$ is minimized, with the constraints $0 \leq \alpha(x) \leq \frac{1}{2}$, i.e.

$$\min_{\alpha(x)} \{|g_w(x)|^2\}, \text{ subject to } 0 \leq \alpha(x) \leq \frac{1}{2} \quad (8.5)$$

The solution to Eq.(8.5) for $\alpha(x)$ is [111]

$$\alpha(x) = -\text{Re}\left[\frac{g(x)}{g(x-X) + g(x+X)}\right], \quad (8.6)$$

where Re represents taking the real part. The SVA image can then be expressed as

$$g_{SVA}(x) = \begin{cases} g(x), & \alpha(x) \leq 0 \\ g(x) + \alpha(x)[g(x-X) + g(x+X)], & 0 < \alpha(x) \leq \frac{1}{2} \\ g(x) + \frac{1}{2}[g(x-X) + g(x+X)], & \alpha(x) > \frac{1}{2}. \end{cases} \quad (8.7)$$

For images which are Nyquist sampled by an integer interpolation factor M , the spacing between samples is $\Delta x = \frac{\pi}{M\Delta}$, such that $x = m\Delta x$, and $X = M\Delta x$. Thus the discrete implementation of the SVA can be directly performed on the image samples at the discrete grids, i.e.,

$$g_w(m) = g(m) + \alpha(m)[g(m-M) + g(m+M)]. \quad (8.8)$$

and

$$\alpha(m) = -\text{Re}\left[\frac{g(m)}{g(m-M) + g(m+M)}\right], \quad (8.9)$$

$$g_{SVA}(m) = \begin{cases} g(m), & \alpha(m) \leq 0 \\ g(m) + \alpha(m)[g(m-M) + g(m+M)], & 0 < \alpha(m) \leq \frac{1}{2} \\ g(m) + \frac{1}{2}[g(m-M) + g(m+M)], & \alpha(m) > \frac{1}{2}. \end{cases} \quad (8.10)$$

When the images are noninteger Nyquist sampled with an interpolation factor R , such that $X = R\Delta x$, where R is an arbitrary real number, the three-point convolution in Eq.(8.4) cannot, thus Stankwitz's SVA formulation cannot be implemented directly on the integer grids of the sampled images. Smith [114] proposed a noninteger Nyquist SVA by introducing a frequency domain aperture function

$$W_s(f) = a + 2\alpha \cos \frac{\pi f}{f_s} \quad (8.11)$$

where f_s is the sampling frequency, a and α are two spatially variant parameters to be determined. Using an aperture function matched to the sampling frequency, the discrete noninteger Nyquist SVA then solves the following constrained minimization problem with respect to $\alpha(m)$

$$\min_{\alpha(m)} \{|g_s(m)|^2\}, \text{ subject to } 0 \leq \alpha(m) \leq \alpha_{max} \quad (8.12)$$

where

$$g_s(m) = ag(m) + \alpha(m)[g(m-M) + g(m+M)], \quad (8.13)$$

$$a = 1 - 2\alpha(m) \frac{\sin \omega_s}{\omega_s}, \quad (8.14)$$

$$\alpha_{max} = \frac{\omega_s}{2[\sin \omega_s - \omega_s \cos \omega_s]} \quad (8.15)$$

and

$$\omega_s = \pi \frac{\Delta}{f_s}. \quad (8.16)$$

In Eq.(8.13), $M = \text{int}(R)$ is the closest integer of the noninteger Nyquist sampling factor R .

The solution to Eq.(8.12) has a similar closed-form to Eq.(8.7), with the upper limit $\frac{1}{2}$ of $\alpha(m)$ in Eq.(8.7) being replaced by α_{max} in Eq.(8.15).

SVA has the following important characteristics [115]:

- (a) Spatially variant aperture function provides sidelobe reduction while preserving main-lobe resolution of the sinc IPR;
- (b) Implicit kernel and the resulting resolution are signal dependent;
- (c) SVA is a nonlinear operation, but pseudo linearity holds for signals with large spatial separation.

Properties (a) and (c) are most desirable for SAR image processing, where an underlying assumption that the data consist of a superposition of discrete point scatterers is usually made.

8.2.2 Super SVA

Super SVA [111, 113] is a nonlinear BWE technique which is based on the premise that SVA preserves sinc IPR mainlobe, but eliminates their sidelobes, i.e., SVA changes the IPR from one which is band-limited (a sinc function) to one which is not band-limited (a sinc mainlobe).

A block diagram of the super SVA algorithm is illustrated in Figure 8.1. A basic super SVA procedure includes the following steps:

- (a) SVA image generation: An FFT is first performed on the band-limited Fourier data, then SVA is applied to the image domain samples to remove the sidelobes. Since SVA is a nonlinear operation, the resultant image is no longer band-limited after SVA processing;
- (b) Bandwidth extrapolation: When performing an inverse FFT on the SVA image, the resultant Fourier spectral domain data will have greater extent than the original band-limited data. The nonlinear SVA operation increases the original bandwidth, but introduces a magnitude taper that includes nulls. For an ideal point scatterer, this taper corresponds to the FFT of a sinc mainlobe and can be computed analytically. Thus, an inverse filtering can be applied to equalize the magnitude taper over an aperture whose extent is within the first

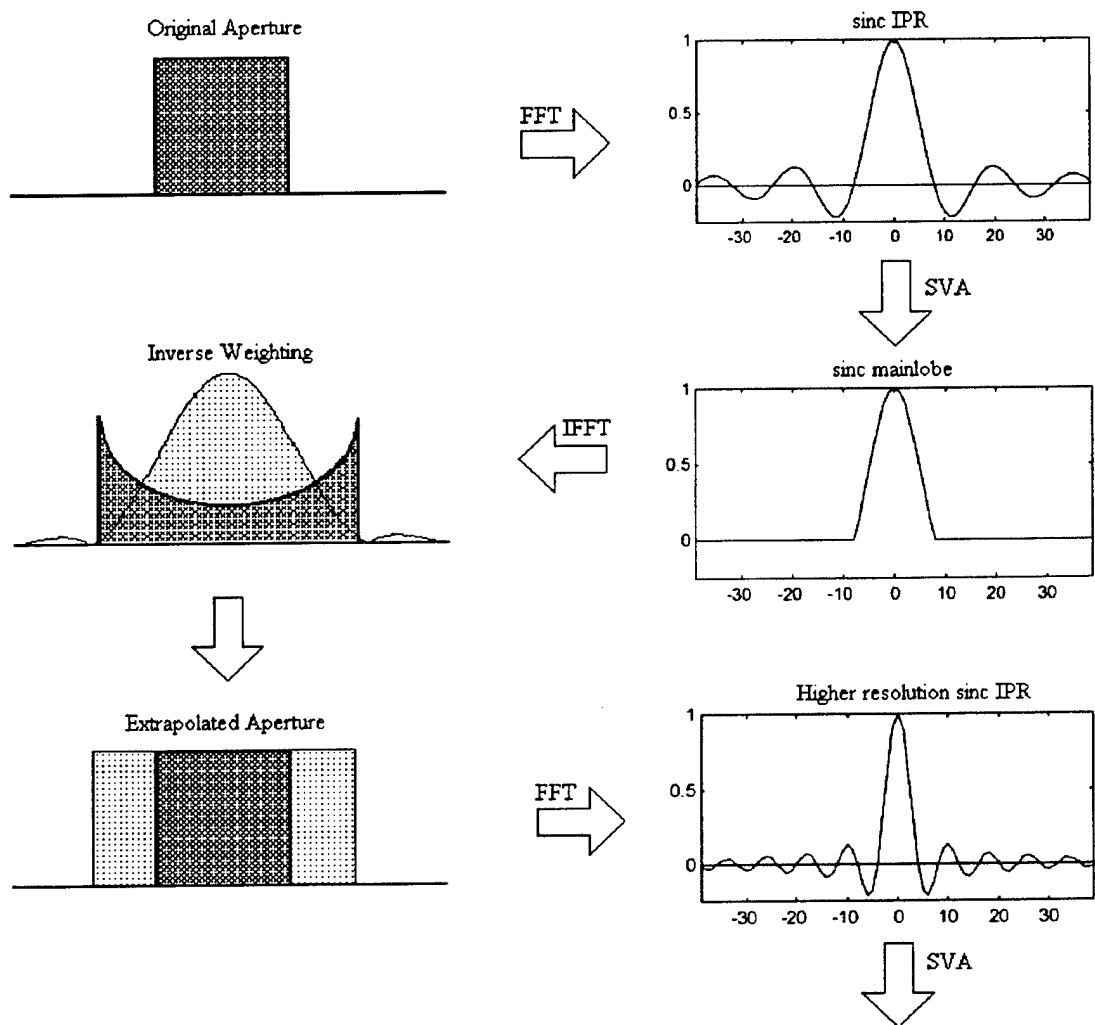


Figure 8.1: The block diagram of super SVA procedure.

nulls on each side so that no singularity exists over the extrapolated aperture (This leads to an expanded aperture which is somewhat larger than the original one by a factor of $\sqrt{2}$); and

(c) Resolution enhanced SVA image generation: An FFT followed by SVA operation can be applied to the bandwidth extrapolated Fourier spectral data to obtain a resolution enhanced image.

The above steps (b) and (c) can be repeated several times for further resolution enhancement. However, in practical applications, if the two steps are repeated in a simple way, at each bandwidth extrapolation iteration some extrapolation error will be introduced. Such an error becomes more and more severe in the successive SVA iterations and prevents the algorithm from achieving a good enhanced resolution. As a consequence, some additional refinements to this procedure must be applied to reduce the extrapolation error, as will be further discussed in Section 8.4.

8.3 A Modified Version of Noninteger Nyquist SVA

Smith's version of noninteger Nyquist SVA performs well in sidelobe reduction. However, it is found that, in SAR/ISAR image processing, when an iterative super SVA procedure is applied for image resolution enhancement, where this version of noninteger Nyquist SVA is used in the iteration process, the resultant images tend to eliminate scatterers which have relatively weak amplitudes. To further study the problem, we consider the IPR of an ideal point scatter.

As shown in Figure 8.2(a), when SVA is formulated on integer Nyquist sampled data, the sidelobes of the IPRs corresponding to the two extreme apertures in Eq.(8.3) for $\alpha_{min} = 0$ and $\alpha_{max} = \frac{1}{2}$, are beating exactly 180° out of phase with each other. Thus, the resulting SVA IPR consists only of a sinc pulse mainlobe. All the sidelobes are perfectly eliminated.

On the other hand, when with noninteger Nyquist sampled data, if Smith's formulation is applied, the two extreme apertures are defined by Eq.(8.11) for $\alpha = 0$ and $\alpha = \alpha_{max}$, where α_{max} is determined by Eq.(8.15). Due to the fact that the sampling frequency f_s is not an integer multiple of Δ , the sidelobes of the two IPRs corresponding to the two extreme

apertures will not beat completely out of phase, as can be seen in Figure 8.2(b).

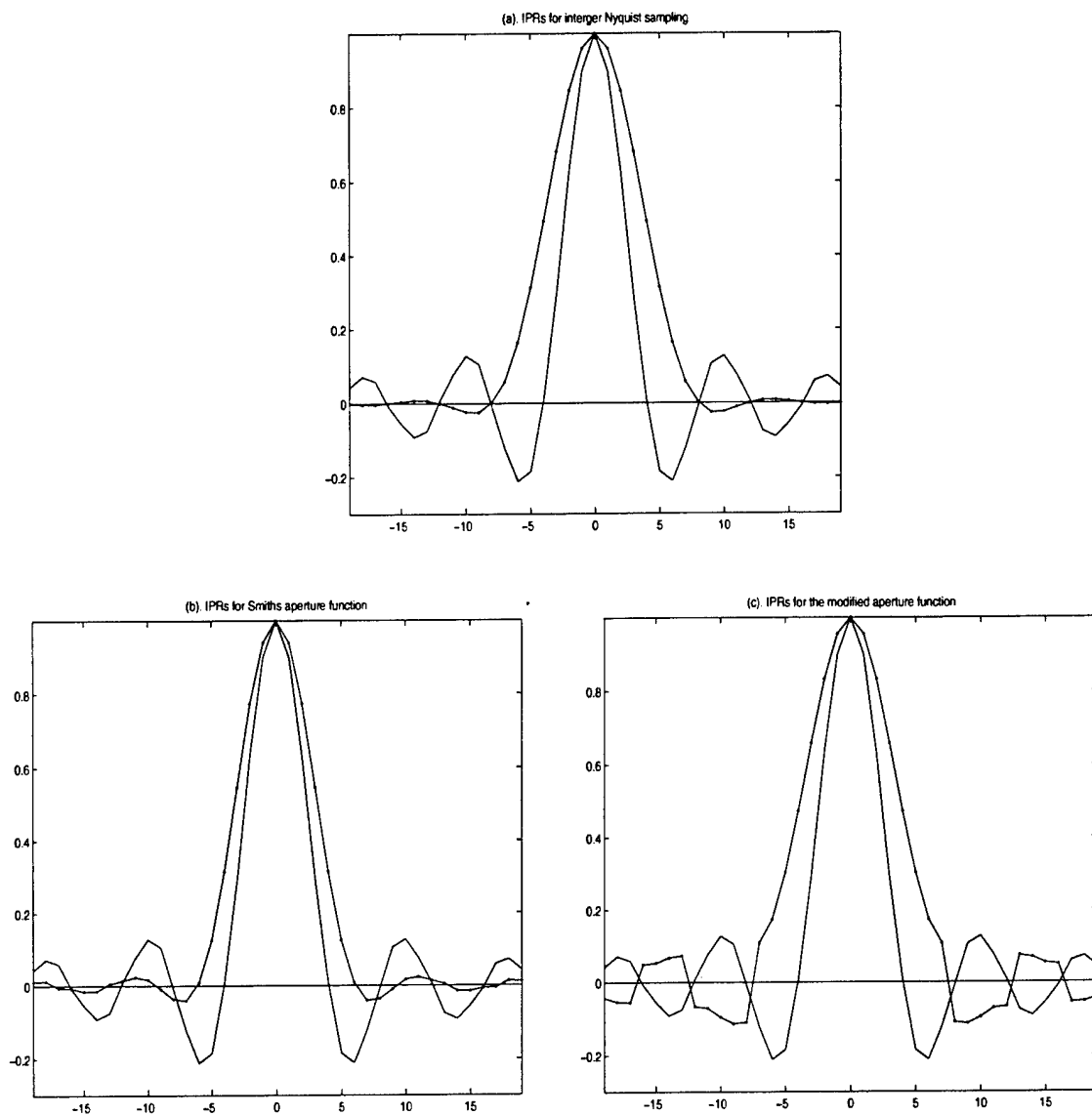


Figure 8.2: The IPRs for different aperture functions.

That is to say, due to the fact that the two extreme apertures have different extents, there exists a residual phase error between the two corresponding IPRs. As a consequence of this residual phase error, for images which consist of multiple scattering centers, the noninteger SVA not only results images with residual sidelobes but also tends to make adverse impact on the mainlobes. Specifically, it tends to eliminate the mainlobes of those scattering centers

which have relatively weak amplitudes. This latter impact is especially severe when an iterative super-SVA procedure is used: With the increase of the number of iterations, more and more scattering centers with relatively weak amplitudes tend to be annihilated.

By noticing the following two facts, it is possible to alleviate the adverse impact of the residual phase error. Firstly, in cosine-on-pedestal aperture, only the two or three sidelobes closest to the mainlobe of its IPR have relatively higher levels. For practical applications, the impact of all the other sidelobes far from the mainlobe is neglectable due to their much lower levels. Secondly, for a given sampling frequency f_s , the residual phase error caused by the noninteger Nyquist aperture can be considered to be constant, i.e.,

$$p = \frac{M - R}{R} \pi \quad (8.17)$$

where R is the noninteger Nyquist sampling factor, and M is the integer closest to R . Thus, it is expected that in the resultant IPR, the above residual phase error can be well compensated at least for those sidelobes closest to the mainlobe, if an additional constant phase is applied to Smith's noninteger Nyquist aperture function.

Based on the above observations, we propose a modified version of the noninteger Nyquist SVA by introducing an aperture function

$$W_N(f) = a + 2\alpha \cos\left[\frac{\pi}{\Delta_s} f + p\right] \quad (8.18)$$

where

$$\Delta_s = (1 + |R - M|)\Delta, \quad (8.19)$$

a and p can be considered to be two aperture compensation coefficients used to compensate for the amplitude and phase errors caused by the noninteger Nyquist sampling, respectively.

The corresponding IPR of the aperture function in Eq.(8.18) can be expressed as

$$w_N(x) = aD(x) + \alpha\left[e^{-jp}D\left(x - \frac{\pi}{\Delta_s}\right) + e^{jp}D\left(x + \frac{\pi}{\Delta_s}\right)\right] \quad (8.20)$$

where $D(x)$ is a sinc kernel in continuous domain. Note that in discrete implementation of the three-point convolution, $D(x)$ is a Dirichlet kernel, i.e.,

$$D(x) = e^{j\frac{\pi}{2}} \frac{\sin[x \cdot \Delta_s]}{\sin[\frac{1}{2}x]}. \quad (8.21)$$

which can be well approximated by a sinc function.

The parameter a and the extreme aperture parameters α_{min} and α_{max} corresponding to the new noninteger aperture function in Eq.(8.18) can be determined by following the same derivation and constraints as in [114], i.e., the unit gain constraint in image domain which requires that

$$w_N(0) = 1, \quad (8.22)$$

and the monotonic gain constraint in frequency domain which requires that

$$W_N(\Delta) \geq 0, \text{ and } W_N(0) > W_N(\Delta). \quad (8.23)$$

From Eqs.(8.18) and (8.21)-(8.23), we have

$$\alpha_{min} = 0, \quad \alpha_{max} = \frac{1}{2[\cos(p)\text{sinc}(\delta_x) + 1]}, \quad (8.24)$$

$$a = \frac{1}{\cos(p)\text{sinc}(\delta_x) + 1} = 2\alpha_{max}, \quad (8.25)$$

where $\delta_x = (R - M)\Delta x$.

It is ready to find that, for the extreme aperture when $\alpha = \alpha_{max}$, the three-point convolution in the image domain can now be expressed as

$$g_N(m) = 2\alpha_{max}\{g(m) + \frac{1}{2}[g(m - M) + g(m + M)]\}. \quad (8.26)$$

This is the desired result: after introducing a residual phase error compensation constant, the extreme aperture for $\alpha = \alpha_{max}$ is equivalent to the case of $a = 1$ and $\alpha = \frac{1}{2}$, plus an aperture gain modification factor $2\alpha_{max}$. Thus, the sidelobes of the IPRs corresponding to the extreme apertures in Eq.(8.18) are forced to beat out of phase.

Figure 8.2(c) demonstrates the IPRs corresponding to the extreme apertures for the new version of noninteger Nyquist aperture function.

8.4 An Iterative Super-SVA Procedure for SAR Image Enhancement

8.4.1 2-D Noninteger Nyquist SVA for SAR image processing

Assume that we have obtained the 2-D Fourier domain (phase history) data $G(u, v)$ of the target to be imaged. In extending the noninteger Nyquist SVA to 2-D SAR imaging, we restrict our discussion to a separable 2-D cosine-on-pedestal aperture function, i.e.,

$$\begin{aligned} W(u, v) &= W_1(u)W_2(v) \\ &= [a_1 + 2\alpha_1 \cos(\frac{\pi}{\Delta_{s1}}u + p_1)][a_2 + 2\alpha_2 \cos(\frac{\pi}{\Delta_{s2}}v + p_2)] \end{aligned} \quad (8.27)$$

where $u \in [-\Delta_1, \Delta_1]$, $v \in [-\Delta_2, \Delta_2]$;

$$\Delta_{s1} = (1 + |R_1 - M|)\Delta_1, \quad (8.28)$$

$$\Delta_{s2} = (1 + |R_2 - N|)\Delta_2, \quad (8.29)$$

and

$$p_1 = \frac{M - R_1}{R_1}\pi, \quad (8.30)$$

$$p_2 = \frac{M - R_1}{R_1}\pi, \quad (8.31)$$

where R_1 and R_2 are two arbitrary real numbers which are the Nyquist sampling factors in u and v directions, respectively, and $M = \text{int}(R_1)$ and $N = \text{int}(R_2)$ are two integers closest to R_1 and R_2 , respectively.

The 2-D windowed phase history data can be expressed as

$$G_w(u, v) = G(u, v)W(u, v) \quad (8.32)$$

and the 2-D SVA image reconstruction relation is obtained as

$$g_w(m, n) = g(m, n) + \alpha_1 P_1 + \alpha_2 P_2 + \alpha_1 \alpha_2 Q \quad (8.33)$$

where

$$P_1 = g(m, n - N) + g(m, n + N) \quad (8.34)$$

$$P_2 = g(m - M, n) + g(m + M, n)$$

$$Q = g(m - M, n - N) + g(m - M, n + N) \\ + g(m + M, n - N) + g(m + M, n + N)$$

where $g(m, n)$ is the image reconstruction using a 2-D rectangular aperture (i.e., $\alpha_1 = \alpha_2 = 0$ and $a_1 = a_2 = 1$).

The 2-D SVA thus attempts to find spatially variant $\alpha_1(m, n)$ and $\alpha_2(m, n)$, such that $|g_w(m, n)|^2$ is minimized, with the constraints $0 \leq \alpha_1(m, n) \leq \alpha_{1max}$ and $0 \leq \alpha_2(m, n) \leq \alpha_{2max}$, i.e.,

$$\min_{\alpha_1(m, n), \alpha_2(m, n)} \{|g_w(m, n)|^2\}, \quad (8.35)$$

subject to $0 \leq \alpha_1(m, n) \leq \alpha_{1max}$ and $0 \leq \alpha_2(m, n) \leq \alpha_{2max}$

where

$$|g_w(m, n)|^2 = |g(m, n) + \alpha_1 P_1 + \alpha_2 P_2 + \alpha_1 \alpha_2 Q|^2 \quad (8.36)$$

Unlike in the 1-D case where we have closed-form solution for the SVA image, minimization of Eq.(8.36) is a nonlinear optimization problem with inequality bounds. The function is not necessarily convex within the region of interest. Thus, this optimization problem represents a very difficult problem, as the solution of it does not guarantee a global minimum. For practical applications, however, additional simplification can be made by noticing that in SAR imaging, both the Fourier domain and the image domain data are usually represented in terms of in-phase and quadrature (I and Q) components. We present two simplified algorithms in the following. Detailed discussion and more algorithms can be found in [111] and [115].

A. 2-D uncoupled SVA on I and Q separately

In this case, SVA processing is applied to the I and Q components of $g(m, n)$ separately. Without severe confusion, if we still use $g(m, n)$ and $g_w(m, n)$ to represent either the I component or the Q component of the complex image, we can write $g_w(m, n)$ as

$$g_w(m, n) = g(m, n) + \alpha_1(P_1 + \alpha_2 Q) + \alpha_2 P_2 \quad (8.37)$$

Notice that now $g(m, n)$ and $g_w(m, n)$ are both real, thus minimizing $|g_w(m, n)|^2$ is equivalent to minimizing $|g_w(m, n)|$.

Eq.(8.37) is a bilinear function of α_1 and α_2 . The optimization scheme simply evaluates $g_w(m, n)$ at the corners of the square $[0, \alpha_{1max}] \times [0, \alpha_{2max}]$, and selects the pixel value which is corresponding to the minimum magnitude of the function, where α_{1max} and α_{2max} can be determined in the same way as in the 1-D case. When using a pseudo computer language to present the algorithm, the procedure for 2-D uncoupled SVA on I and Q separately can be described as follows:

For image pixel (m, n)

Let $S = \{(0, 0), (0, \alpha_{2max}), (\alpha_{1max}, 0), (\alpha_{1max}, \alpha_{2max})\}$.

Compute $g_w(m, n)$ at the corners $(\alpha_1, \alpha_2) \in S$.

if (any of values $g_w(m, n)$ thus computed have sign opposite to that of $g(m, n)$)

$g_{SVA}(m, n) = 0;$

else

$g_{SVA} = g_w(m, n)$ such that $\min_{(\alpha_1, \alpha_2) \in S} \{|g_w(m, n)|\};$

end

It is seen that, this procedure is in principle not appropriate for interferometric image processing, due to the fact that it process the I and Q components separately in the SVA processing. However, experiment results show that, in many cases, the most important interferometric information is still preserved, though it may be not so reliable. For better interferometric SVA imaging, the I and Q jointly SVA procedure can be applied.

B. 2-D coupled SVA on I and Q jointly

When the two dimensions are coupled, i.e., $\alpha_1 = \alpha_2 = \alpha$, the SVA applied to I and Q jointly in Eq.(8.36) can be greatly simplified. In this case, we minimize $h(\alpha) = |g_w(m, n)|^2$ with respect to α at each image pixel (m, n) . From Eq.(8.36) it can be seen that the function $h(\alpha)$ is of fourth order in α . Thus, the optimization problem reduces to solving a cubic equation where a closed-form expression for the roots exists.

The 2-D coupled SVA procedure on I and Q jointly is thus as follows:

```
For image pixel (m, n)
  if  $Q \neq 0$ 
    find the roots  $\tilde{\alpha}$  of the cubic equation.
    if (any of the roots are within  $[0, \alpha_{max}]$ )
      Compute  $g_w(m, n)$  at the roots and at  $\{0, \alpha_{max}\}$ .
       $g_{SVA}(m, n) = g_w(m, n)$  such that  $\min_{\alpha \in \{\tilde{\alpha}, 0, \alpha_{max}\}} |h(\alpha)|$ ;
    else
       $g_{SVA}(m, n) = g_w(m, n)$  such that  $\min_{\alpha \in \{0, \alpha_{max}\}} |h(\alpha)|$ ;
    end
  else
    find  $g_{SVA}$  as in 1-D SVA.
  end
```

8.4.2 An iterative super SVA procedure

Based on the above 2-D SVA algorithms and on the basic super SVA algorithm shown in Figure 8.1, a iterative 2-D super SVA procedure can be implemented and used for SAR image resolution enhancement. The block diagram of the iterative super SVA procedure is illustrated in Figure 8.3. According to Figure 8.3, the iterative procedure mainly consists of two iteration loops. The outer loop is designed for the bandwidth extrapolation by a given factor, while the inner loop is for the refinement of the super SVA processing to reduce the BWE error to within a specified error bound.

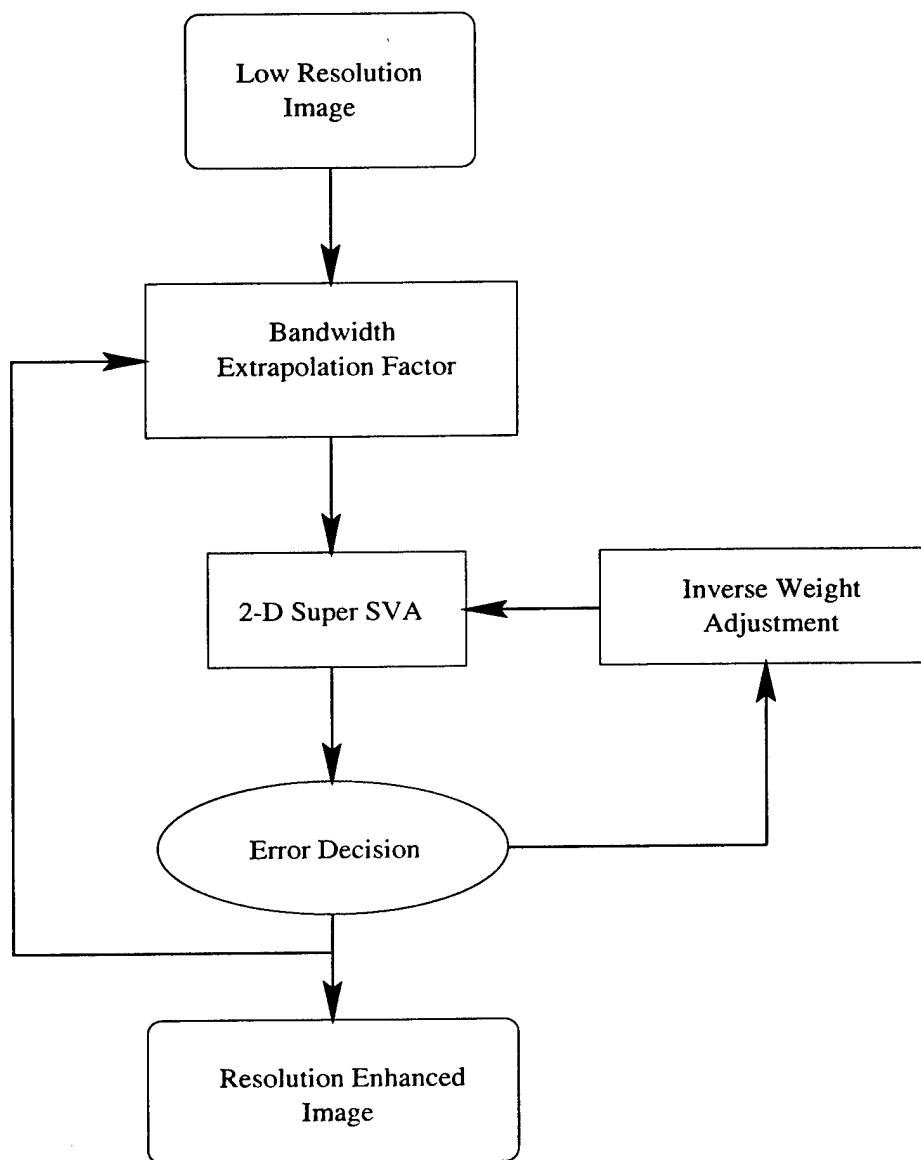


Figure 8.3: The block diagram of the iterative super SVA procedure.

In the inner iteration loop, after 2-D super SVA BWE is applied, the center portion of the extrapolated data is replaced by the measured data. Then non-extrapolative iterations are performed to reduce the extrapolation error. At each iteration, an extrapolation error is established by calculating the relative difference between the extrapolated data and the measured data in the central portion, i.e.,

$$\epsilon = \frac{\sum_{u \in [-\Delta_1, \Delta_1], v \in [-\Delta_2, \Delta_2]} |G(u, v) - \hat{G}(u, v)|}{\sum_{u \in [-\Delta_1, \Delta_1], v \in [-\Delta_2, \Delta_2]} |G(u, v)|}, \quad (8.38)$$

where $G(u, v)$ is the measured data, and $\hat{G}(u, v)$ is the super SVA extrapolated data in the center portion. As soon as the extrapolation error reaches the given error bound ϵ_0 , the procedure switches to another turn of BWE iteration in the outer iteration loop.

The 2-D inverse weight is adjusted at each iteration and is determined as follows. Every time when the procedure switches to a new turn of BWE iteration, for the first iteration in the inner loop, a new inverse weight function, $I(u, v)$, is calculated. For the following iterations, at the k th iteration, this inverse weight, $I_k(u, v)$, is modified as

$$I_k(u, v) = I^{\beta_k}(u, v) \quad (8.39)$$

where $0 \leq \beta_k \leq 1$.

The number of iterations in the outer loop is determined by the specified BWE factor. As in 1-D super SVA case, for one BWE iteration, the BWE factor can be $\sqrt{2}$ or so. To avoid singularity in the 2-D BWE, we constrain the inverse weight function $I(u, v)$ by

$$I(u, v) = \begin{cases} \tilde{I}(u, v), & \text{if } \sqrt{u^2 + v^2} \leq \Delta_u \text{ and } \sqrt{u^2 + v^2} \leq \Delta_v \\ 0, & \text{otherwise.} \end{cases} \quad (8.40)$$

where Δ_u and Δ_v are the extent of the SVA extrapolated data in u -direction and v -direction for the current BWE iteration, respectively, $\tilde{I}(u, v)$ is the inverse weight analytically computed by considering that the magnitude taper in the BWE data corresponds to the FFT of a 2-D sinc mainlobe.

On completion of the determined number of BWE iterations in the outer loop, the procedure then outputs the resultant resolution enhanced super SVA image.

8.5 Application Examples

We first present an example to show the difference of the performance between Smith's formulation and the modified formulation for noninteger Nyquist SVA. Figure 8.4 demonstrates

a 2-D SAR image processing example. The original SAR image is from the MSTAR (Moving and Stationary Target Acquisition and Recognition) public SAR image data sets. The acquisition parameters of the MSTAR data will be given later.

In Figure 8.4, from top to bottom, the first two images are the original unwindowed and the 35 dB Taylor windowed images, the two images in the middle illustrate the SVA image and $2\times$ super SVA image using Smith's formulation, and the last two images demonstrate the SVA image and $2\times$ super SVA image using the modified formulation in this study. It is seen that, as pointed out in Section 8.2, when Smith's formulation is applied, the SVA and super SVA images tend to eliminate scattering centers with weak amplitudes. On the other hand, the weak scattering centers are much better preserved when the modified formulation is applied. We also note that in the latter case, the residual sidelobes in the resultant image are slightly higher. This is due to the fact that when a constant phase is introduced in the aperture function, a higher sidelobe level will result in the corresponding IPR. However, the residual sidelobes are still very low by noticing that the 40 dB image dynamic range in all the images. Therefore, in all the following examples, we only provide the results obtained by using the modified formulation when noninteger SVA is used.

8.5.1 Application to SAR Image Enhancement for ATR

Automatic target recognition (ATR) using SAR images requires the measurement of scatterer positions and the comparison of those positions to a database composed of the positions of strongly backscattering features for each candidate. Resolution is a controlling factor in acquiring details of target structure from its 2-D SAR images. Thus, image resolution is one of the most important specifications for higher recognition probability in automatic target recognition using SAR images. It is reported in [74] that, when the 2-D resolution is enhanced from $1\text{ m} \times 1\text{ m}$ to $0.5\text{ m} \times 0.5\text{ m}$, the correct recognition rate increases by 30%. Therefore, super resolution image processing is a most promising technique for higher correct recognition rates. In this example, we demonstrate the application of the iterative super SVA procedure to SAR image processing for ATR.

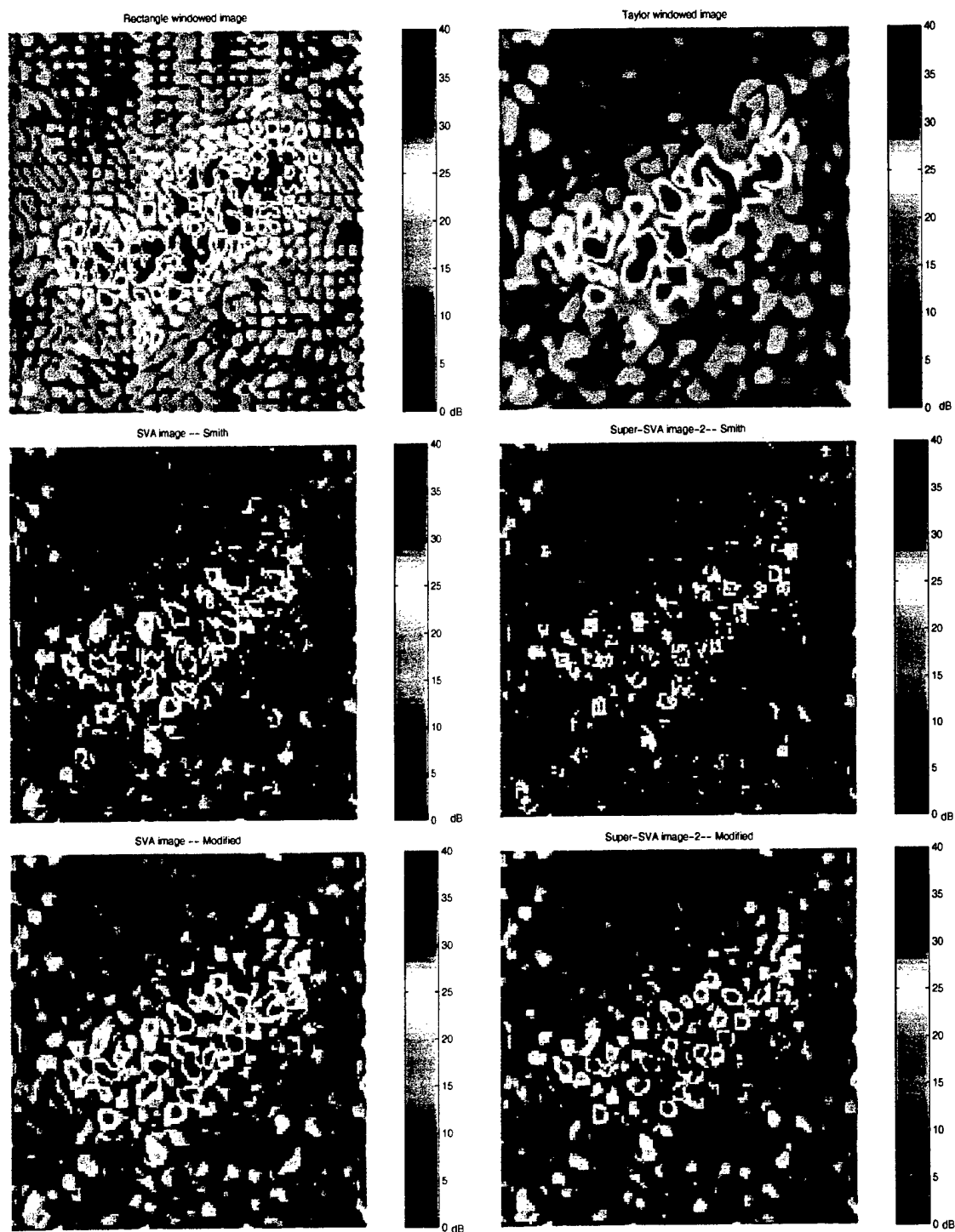


Figure 8.4: Comparison of the super SVA SAR images using different noninteger Nyquist formulations.

The MSTAR airborne SAR public data sets are used. The data were collected by Sandia National Laboratory using the STARLOS sensor. The SAR operates at X band, with central frequency 9.6 GHz, bandwidth 0.591 GHz. The nominal down range resolution and the cross range resolution of the original images are both 0.3 m. In the 2-D image reconstruction of the original MSTAR image chips, a 2-D Taylor window was used. The Taylor windowed image has -35 dB sidelobes, while the resolution is worse by a factor about 1.6. Thus, the practical 2-D resolution of all the images is about $0.5 \text{ m} \times 0.5 \text{ m}$. The super SVA algorithm operates on the unwindowed image. Thus, before super SVA processing can be applied, the original MSTAR SAR images must be equalized using a 2-D inverse Taylor weighting equalization filter to obtain the unwindowed images. A simplified block diagram for the super SVA processing to MSTAR SAR images is illustrated in Figure 8.5.

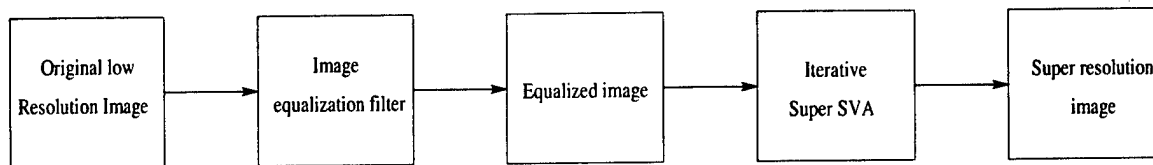


Figure 8.5: Simplified block diagram of super SVA processing of the MSTAR SAR images.

The super resolution image processing begins with a 2-D complex SAR image. The complex SAR image is input into an image equalization filter. The equalization filter transforms the complex image back to phase history domain, removes the Taylor weighting applied to the original SAR image, and then transforms the unweighted phase history data back to the image domain. The formed unwindowed 2-D complex image is then processed using a 2-D iterative super SVA procedure. After completion of the specified BWE extrapolation, the super resolved 2-D SAR image is obtained.

We have tested the procedure on more than 20 different target images under different clutter backgrounds. In all the cases, the iterative procedure proposed in this report performs well without exception. We provide two examples below.

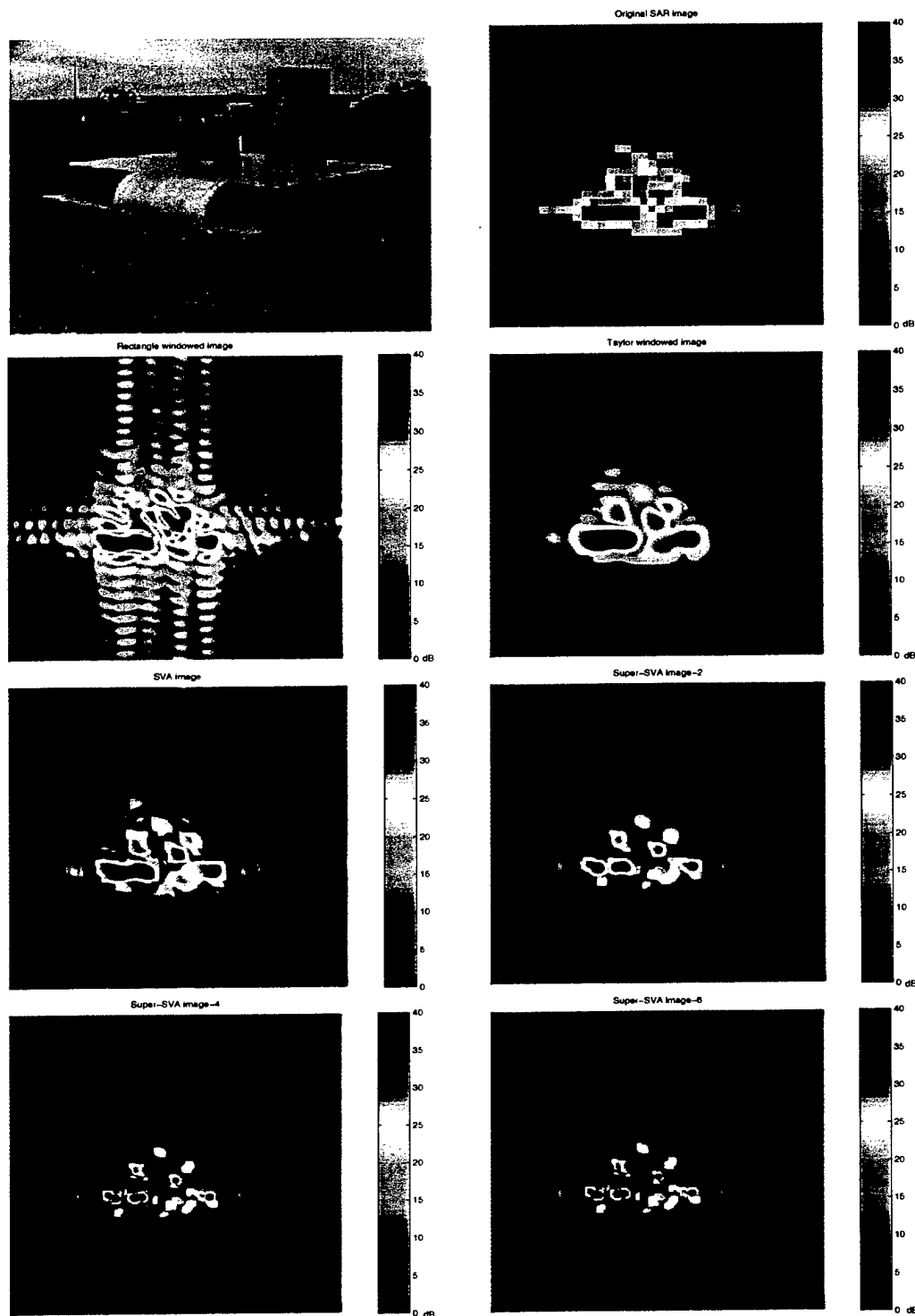


Figure 8.6: SLICY images, from top to bottom, left to right: Target photograph, Original MSTAR image; Equalized image, Taylor windowed image; SVA image, Super SVA image-2; Super SVA image-4, and Super SVA image-6.

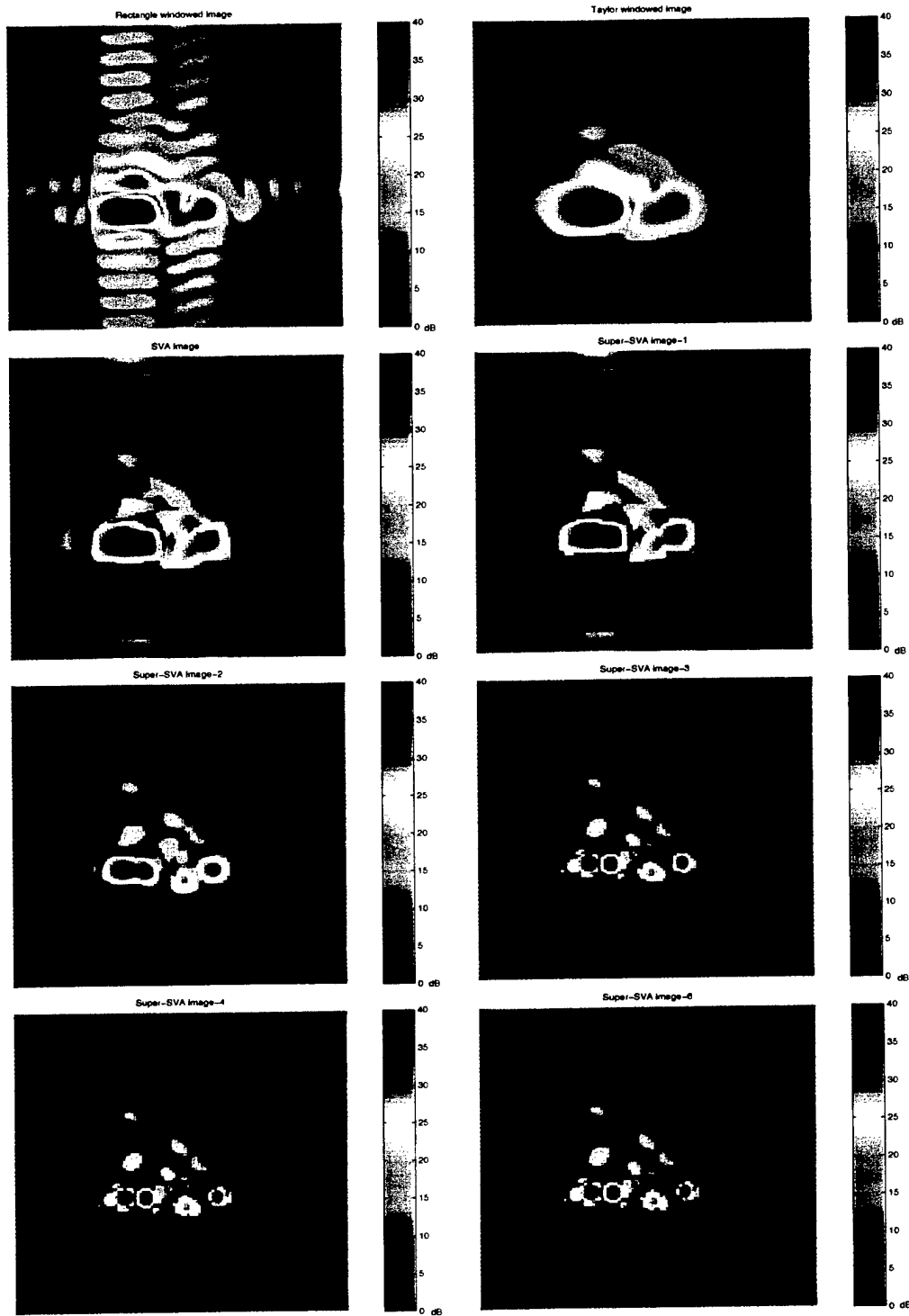


Figure 8.7: SLICY images using 25% partial phase history data, from top to bottom, left to right: Unwindowed image from partial data, Taylor windowed image; SVA image, Super SVA image-1; Super SVA image-2, Super SVA image-3; Super SVA image-4, and Super SVA image-6.

Figure 8.6 shows the images of the MSTAR target SLICY which is a relatively simple target with predictable radar signatures. In this figure, the images are organized as follows, from left to right and top to bottom: The photograph of the target, the original image, the equalization filtered image, the Taylor windowed image, SVA image, $2\times$ super SVA image (image-2), $4\times$ super SVA image (image-4), and $8\times$ super SVA image (image-6) are illustrated. Note that in the unwindowed image, the sidelobes are so high that the image quality is unacceptable. On the other hand, in the SVA image, sidelobes are greatly reduced while the resolution of the unwindowed image is still preserved. Further resolution enhancement is obviously seen in the super SVA images. All the major scattering centers are much better resolved in the super SVA images.

To further investigate the super resolution capability of the super SVA procedure, we present Figure 8.7. The original input image is the same as in Figure 6. However, in this case, only 25% of the phase history data at the output of the equalization filter is used for image processing. Thus, now the 2-D resolution of the Taylor windowed image is about $1\text{ m} \times 1\text{ m}$. In Figure 8.7, the images are organized as follows, from left to right and top to bottom: The unwindowed image using 25% partial phase history data, the Taylor windowed image, SVA image, $\sqrt{2}\times$ super SVA image (image-1), $2\times$ super SVA image (image-2), $2\sqrt{2}\times$ super SVA image (image-3), $4\times$ super SVA image (image-4), and $8\times$ super SVA image (image-6) are illustrated. Once again, the super SVA images have much better resolution than the Taylor windowed image. The multiple scattering centers which previously cannot be resolved in the Taylor windowed image can now be well resolved.

It is also seen that, however, in both Figure 8.6 and Figure 8.7, when the BWE factor is larger than 4, the further improvement of the resolution is not so obvious. This is due to the fact that the BWE error becomes large when with a larger BWE factor. In the present study, we found that the optimum BWE factor is $2\sqrt{2} \sim 4$. For the $2\sqrt{2}\times$ super SVA image, the BWE factor is 2.82. Thus, in theory, this super SVA image has a better 2-D resolution than the Taylor windowed image by a factor of 4.5. In the real world, there will be a resolution degradation due to the impact of the BWE error. Taking into account of such resolution degradation, a resolution improvement factor better than 3 could be expected.

Figure 8.8 illustrates the image processing results for the 2-D SAR image of a T-72

tank. It represents the case where the target under test is very complex and the SCR is relatively low. That is, there exists observable background clutters around the target. The organization of the figure is similar to Figure 8.6, but the $\sqrt{2}\times$, $2\times$, and $2\sqrt{2}\times$ super SVA images are shown in this figure. It is seen that, the iterative super SVA algorithm is capable of generating resolution enhanced images even if the SCR is relatively low.

In the context of ATR, it is also of interest to see how the super SVA performs on the clutter image. Figure 8.9 demonstrates the original and the SVA images of a clutter area. It is seen that, in the sense of super resolution, super SVA performs in the same way on clutter images as well as on target images. However, comparing the SVA images with the original one, it is seen that the texture pattern of the background clutter is changed to be more point-like after super SVA processing.

This property of super SVA algorithm could be an advantage to ATR: the 2-D SAR images of man-made targets usually consists of multiple discrete scattering center, while the clutter images are more likely continuous. Therefore, when a target is embedded in the clutter, super SVA tends to enhance the multiple scattering centers of the target while reducing the impact of the clutter. Figure 8.10 shows the amplitude distribution of the original and the $2\sqrt{2}\times$ super SVA images in Figure 8. The ordinate is the pixel amplitude, while the abscissa is the occurrence probability. Obviously, the amplitude distribution of the super SVA image is more desirable for the CFAR processing [116, 117] to threshold the image for target detection and recognition.

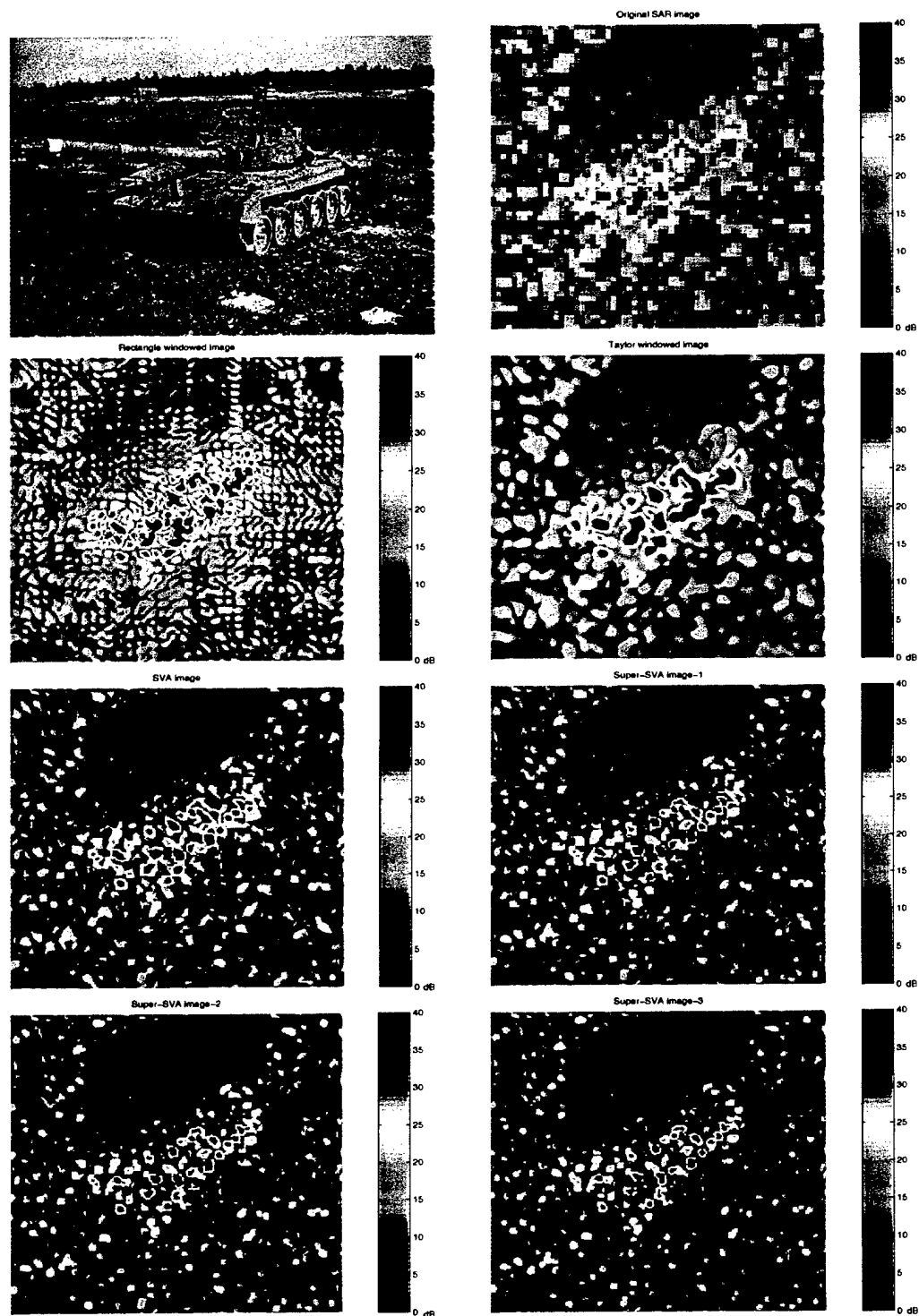


Figure 8.8: T72-A64 images, from top to bottom, left to right: Target photograph, Original
MSTAR image; Equalized image, Taylor windowed image; SVA image, Super SVA image-1;
Super SVA image-2, and Super SVA image-3.

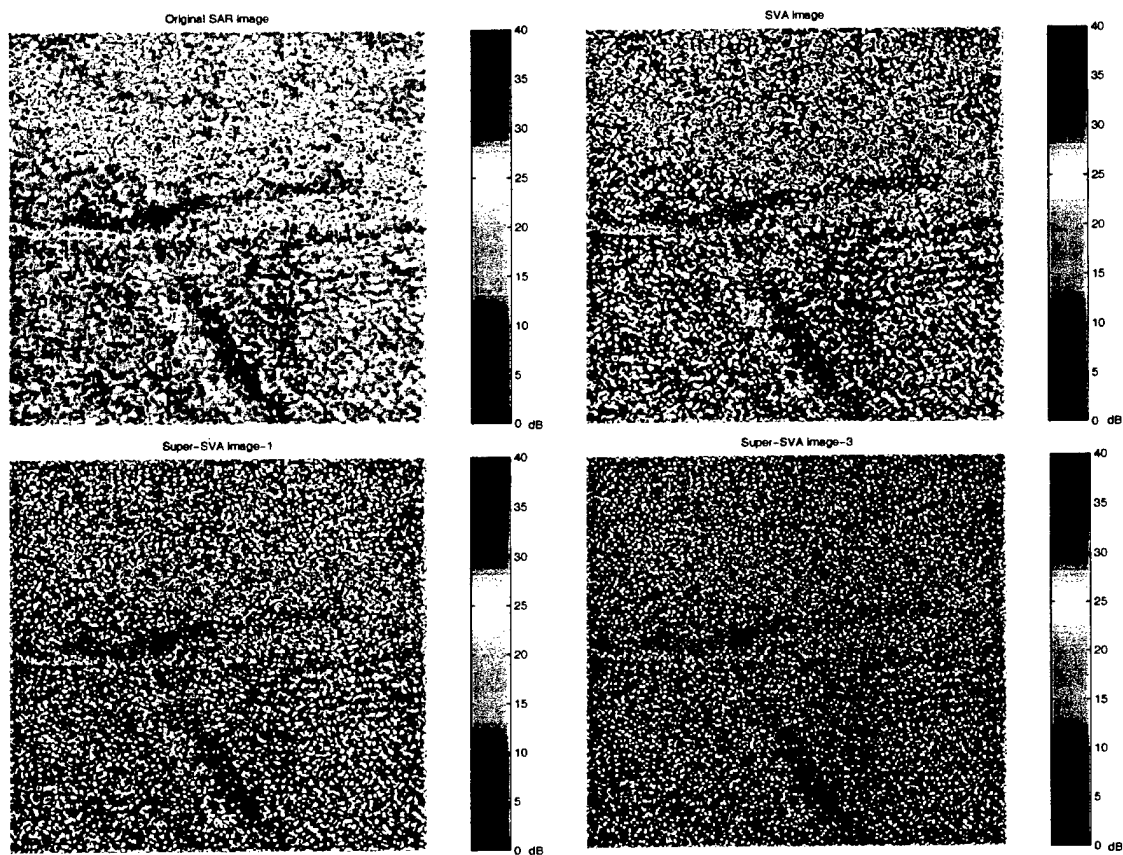


Figure 8.9: Clutter images, from top to bottom, left to right: Original MSTAR image, SVA image, Super SVA image-1; and Super SVA image-3.

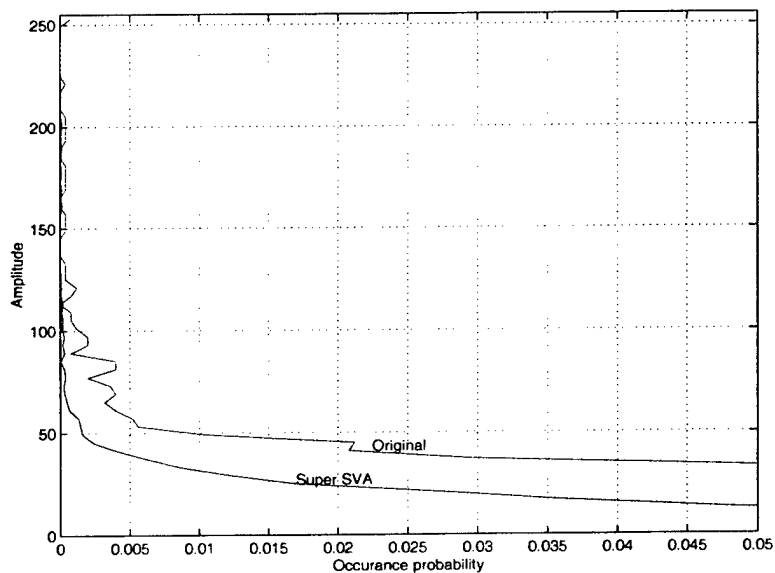


Figure 8.10: Amplitude distribution of the original (blue) and the super SVA (red) images .

8.5.2 Application to 3-D IF-ISAR Image Enhancement

As discussed in Chapter 6, in 3-D IF-ISAR imaging, the target altitude image is derived from two 2-D ISAR images reconstructed from the phase history measurements by antennas at different altitudes. In the 3-D imaging system model, an implicit assumption is that there exists only a single scattering center at each image pixel. When there are multiple scattering centers in one resolution cell, the resultant 3-D altitude reflects the equivalent altitude of the multiple scatterers only when the equivalent scattering magnitude is not too small. Otherwise, the altitude image may be severely contaminated by the phase scintillation due to the coherent interference of the multiple scattering centers. It is thus readily seen that, in 3-D IF-ISAR imaging, the higher the resolution in the 2-D ISAR images, the more accurate is the resulting 3-D altitude image.

In this example, we demonstrate the application of super SVA to 3-D IF-ISAR imaging. Because we use two ISAR images to derive the 3-D altitude distribution of a complex target, due to the requirement of the interferometric phases, the SVA algorithm on I and Q jointly is applied. Furthermore, we point out that, though SVA algorithm on I and Q jointly preserves the image phase, super SVA iteration does introduce additional phase error caused by the nonlinear BWE error, which may destroy the phase interferometry between the two 2-D ISAR images. Therefore, in the 3-D interferometric processing, we only use the SVA image phase to derive the target altitude image, while in the thresholding of the image, the amplitude of the $2\times$ super SVA images are used.

Figure 8.11 shows the resultant images for an aircraft model. The original phase history data were collected in the anechoic chamber compact range at Beijing Institute of Environmental Features. The imaging parameters are: Central frequency 9.25 GHz, bandwidth 1.8 GHz, azimuthal angle range $[-6^\circ, +6^\circ]$. The left column (Figure 11(a)-(c)) illustrates the two ISAR images and the corresponding IF-ISAR altitude image when a conventional backprojection algorithm was used. The right column (Figure 8.11(e)-(f)) illustrates the two ISAR images and the corresponding IF-ISAR image where $2\times$ super SVA was applied. It is seen that, for high SNR/SCR radar imaging data, the super SVA results much better resolved ISAR images, thus forms better target altitude image.

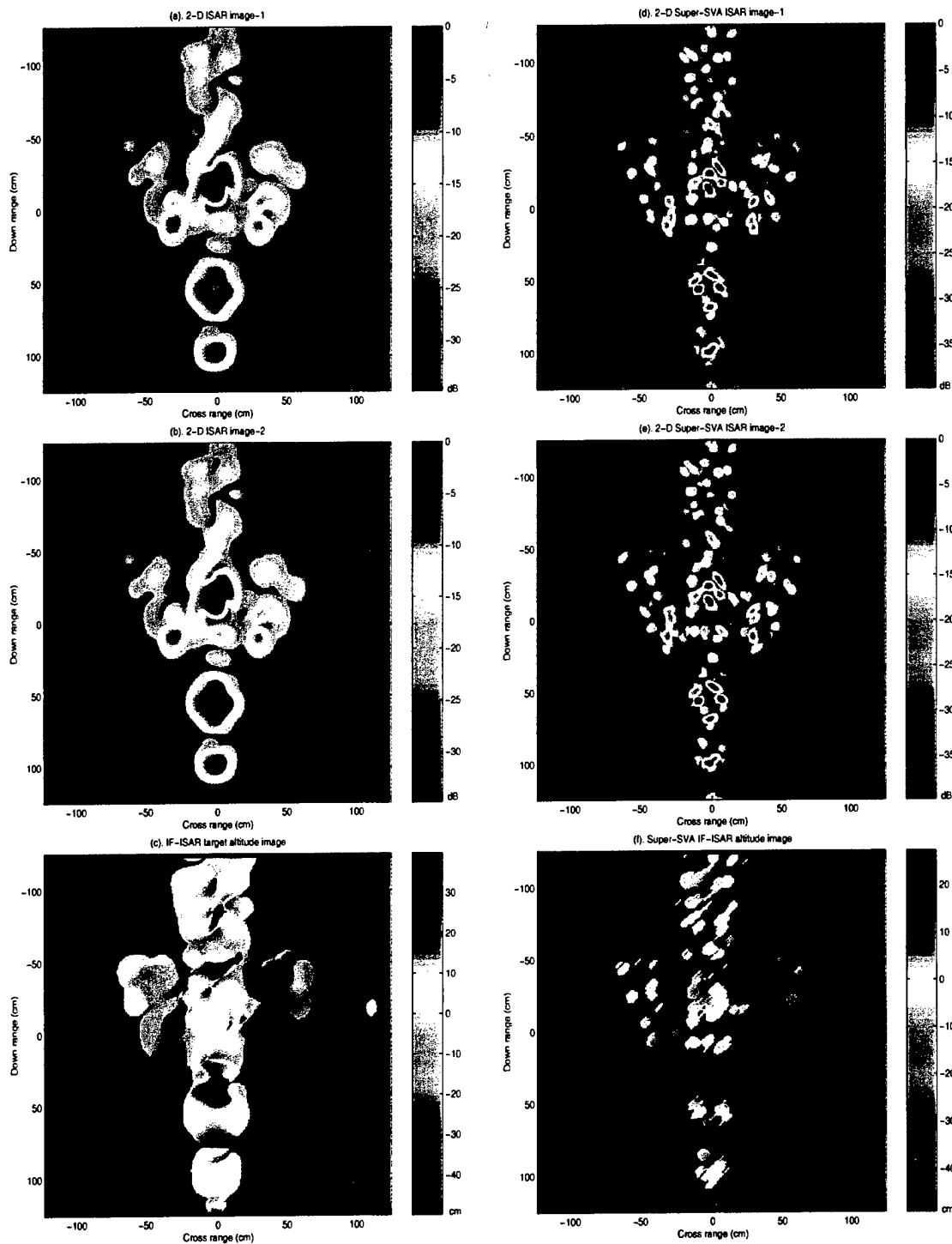


Figure 8.11: Super SVA IF-ISAR images of an aircraft model.

8.6 Application of Super SVA to FOPEN Random Noise SAR Images

SVA is mainly applied to SAR images reconstructed from radar data which have 2-D rectangular spectral ROS. In most SAR and ISAR imaging systems, we usually have circular sector shaped spectral regions of support. For conventional SAR imaging where the radar operates at a higher frequency and with a small fractional bandwidth, the requirement of the the rectangular spectral ROS can be met by spectral domain polar-to-rectangular resampling. However, for FOPEN UWB SAR imaging, this is usually not the case. In FOPEN applications, the imaging radar usually operates at lower frequencies, with a very large fractional bandwidth and a wide aspect angle span for aperture synthesis. As was discussed in Chapter 7, to obtain image resolution in both slant range and cross range, image formation algorithms using the complete circular sector spectral ROS data must be used. As a consequence, a direct use of SVA to the UWBWA SAR images is usually not applicable.

To overcome the above difficulty, we use the following procedure for an approximate processing of FOPEN random noise SAR image enhancement by means of the super SVA technique developed for conventional SAR images.

Step-1: Image reconstruction using the back-projection algorithm and perform image sidelobe reduction using the method developed in Chapter 7;

Step-2: Fourier transform the SAR image to spectral domain and applying an approximate 2-D equalization filter;

Step-3: Limit the so processed spectral ROS to a rectangular region slightly smaller than the original circular sector region, as illustrated in Figure 8.6;

Step-4: Perform super SVA in the same way as in conventional SAR image processing and obtain the final image.

It is found that, when the synthetic aperture angle is not too large (e.g., $< 45^\circ$), by following the above procedure, the super SVA technique is still applicable to the FOPEN

UWB SAR data, although some spectral ROS error was introduced in the procedure. Figure 8.6 illustrates the super SVA image enhancement result of the FOPEN UWB random noise SAR image of two trihedral reflectors obscured behind trees. More information about the original SAR image can be found in Section 5. It is seen that, after $2\times$ super SVA processing, better image resolution is obtained.

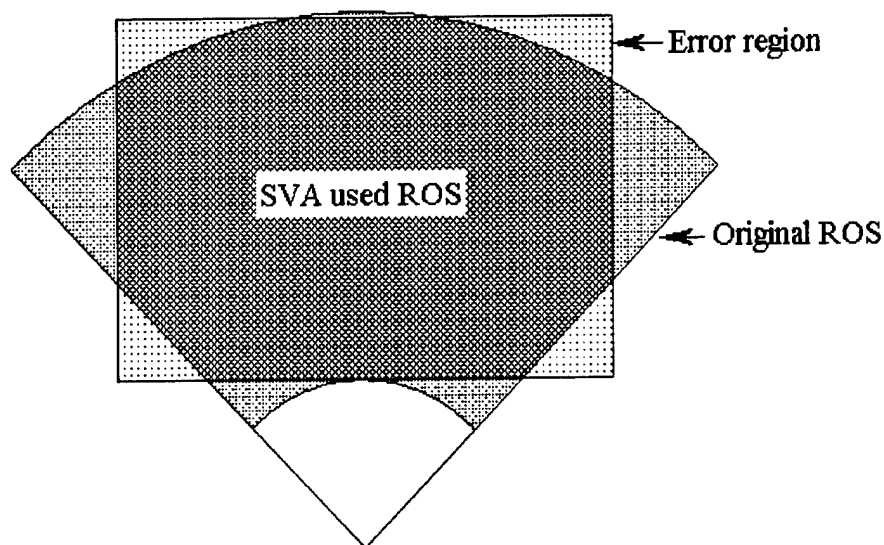
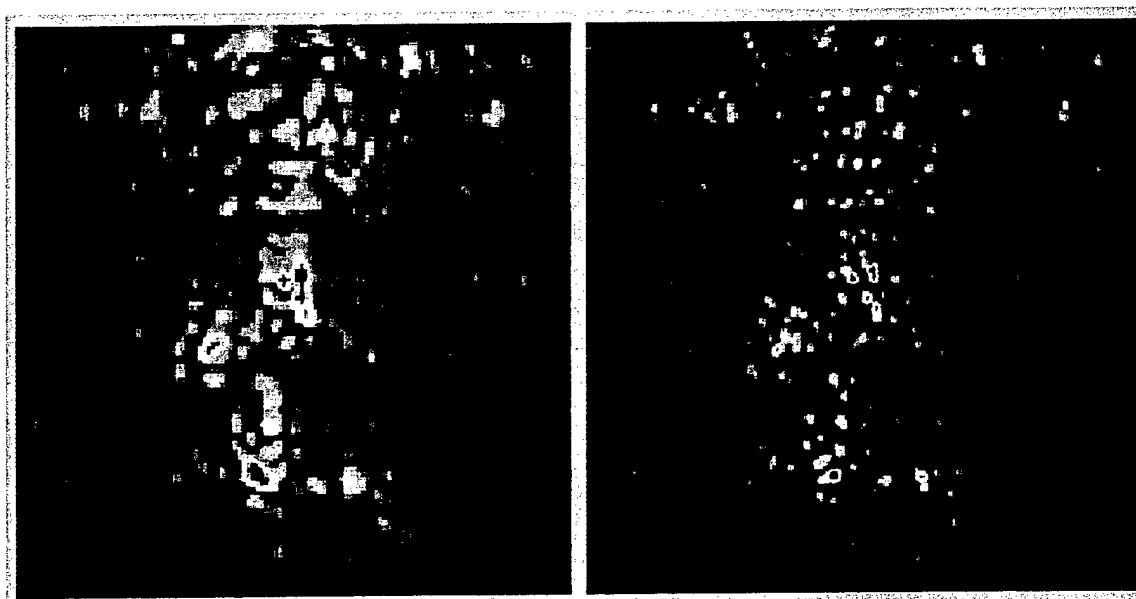


Figure 8.12: Spectral ROS used in super SVA image enhancement

8.7 Summary

We have studied the SVA technique and its applications to SAR/ISAR image processing. A modified noninteger Nyquist SVA formulation is proposed, which is especially useful for radar image processing. An iterative super SVA procedure is developed for SAR image resolution enhancement. The promising results of the examples demonstrate that, applications of the technique developed in this chapter can be found in SAR image processing for automatic target recognition, ISAR image processing for 3-D imaging, target scattering diagnosis and modeling. A slightly modified procedure is also applicable to FOPEN SAR and random noise SAR image processing.



Original FOPEN SAR image

Super SVA enhanced image

Figure 8.13: Super SVA image enhancement of the FOPEN random noise SAR image of two trihedral reflectors obscured behind foliage

Chapter 9

CONCLUSIONS AND FUTURE WORK

UWB radar waveforms at lower frequency band provide fine down range resolution and superior medium penetration performance. UWB random noise waveform has additional advantages, such as low probability of intercept (LPI) and low probability of detection (LPD), inherent anti-RFI and anti-jamming capabilities, low cost design and so on. In this research work, we have presented the theoretical and experimental aspects of a UWB coherent random noise SAR system, as well as the image processing techniques. The system operates over the frequency band 250-500 MHz and is specially designed for foliage penetration imaging applications. We have demonstrated the high resolution foliage penetration SAR imaging capability of the experimental UWB random noise radar.

There are still numerous areas of interest that could be investigated using UWB coherent random noise radar. Some suggestions for future work on foliage penetration imaging and on random noise radar technique for covert detection and identification of targets obscured by foliage include:

- Enhancement of the polarization matrix measurement capability of the FOPEN random noise radar system and polarimetric clutter suppression and image enhancement techniques for UWB random noise radar imagery;
- Theoretical and experimental studies of precursor fields when electromagnetic pulses

of different characteristics propagate in dense foliage media, and the applications of this unique wave propagation phenomenon to FOPEN radar imaging;

- Radar penetration imaging using spectrally fragmented UWB random noise waveforms, which is specially of importance in a practical battlefield scenario for UWB radar imaging operation; and
- Development of algorithms for detection and identification of targets obscured by foliage using a polarimetric random noise foliage penetration radar.

References

- [1] J.G. Fleischman, S. Ayasli, E.M. Adams, and D.R. Gosselin, "Foliage penetration experiment, Part I: Foliage attenuation and backscatter analysis of SAR imagery," *IEEE Transactions on Aerospace and Electronic Systems*, Vol.32, No.1, Jan. 1996, pp.134-144.
- [2] M.F. Toups, Ayasli, and J.G. Fleischman, "Foliage penetration experiment, Part II: Foliage-induced synthetic pattern distortion," *IEEE Transactions on Aerospace and Electronic Systems*, Vol.32, No.1, Jan. 1996, pp.145-155.
- [3] D. R. Sheen, N. P. Malinas, D. W. Kletzli, Jr., T. B. Lewis, and J. F. Roman, "Foliage transmission measurement using a ground-based Ultrawide band (300-1300 MHz) SAR system," *IEEE Transactions on Geoscience and Remote Sensing*, Vol.32, No.1, Jan. 1994, pp.118-130.
- [4] M. E. Davis, P. G. Tomlinson, and R. P. Malony, "Technical challenges in ultra-wideband radar development for target detection and terrain mapping," *Proc. IEEE Radar Conf.*, Boston, MA, April 1999, pp.1-7.
- [5] B. M. Horton, "Noise-modulated distance measuring systems", *Proceedings of IRE*, Vol. 49, No. 5, May 1959, pp. 821-828.
- [6] M. P. Grant, G. R. Cooper, and A. K. Kamal, "A class of noise systems," *Proc. IEEE*, Vol.51, No.7, July 1963, pp. 1060-1061.
- [7] G. R. Cooper and C. D. McGillem, "Random signal radar," Final Rep. TR-EE67-11, Purdue Univ. School Elect. Eng., Lafayette, IN, June 1967.

- [8] E. K. Walton, "Use of the fixed range noise radar for moving vehicle identification", *Proc. Sensors and Electrical Devices Symposium (University of Maryland)*, 1997.
- [9] R. M. Narayanan, and M. Dawood, "Doppler estimation using a coherent ultrawide-band random noise radar", *IEEE Transactions on Antennas and Propagation*, Vol.48, No.6, June 2000, pp.868-878.
- [10] R. M. Narayanan, Y. Xi, P. D. Hoffmeyer, and J. O. Curtis, "Design, performance, and applications of a coherent ultrawideband random noise radar", *Opt. Eng.*, Vol.37, No.6, June 1998, pp.1855-1869.
- [11] R. M. Narayanan, R. D. Mueller, and R. D. Palmer, "Random noise radar interferometry", *Proc. SPIE Conference on Radar Processing, Technology, and Applications*, (W. Miceli, Ed.), Vol.2845, Denver, CO, August 1996, pp.75-82.
- [12] D. S. Garmatyuk, and R. M. Narayanan, "SAR imaging using a coherent ultrawideband random noise radar," *Proc. SPIE Conference on Radar Processing, Technology, and Applications IV*, (W. Miceli, Ed.), Denver, CO, Vol.3810, July 1999, pp. 223-230.
- [13] D. Tarchi, D. Leva, K. A. Lukin, A. A. Mogila, and A. J. Sieber, "Short range imaging applications using noise radar technology," *Proc. of EUSAR'2000, Munich Germany*.
- [14] E. K. Walton, V. Fillimon, and S. Gunawan, "ISAR imaging using UWB noise radar," *Proc. 18th AMTA Symposium*, Seattle, Sept.30 - Oct.3, 1996, pp.167-171.
- [15] D. C. Bell and R. M. Narayanan, "Inverse synthetic aperture radar imaging using a coherent ultrawideband random noise radar system," *Opt. Eng.*, Vol.40, Nov. 2001, pp.2612-2623.
- [16] D. C. Bell, and R. M. Narayanan, "Theoretical aspects of radar imaging using stochastic waveforms," *IEEE Transactions on Signal Processing*, Vol.49, No.2, Feb. 2001, pp.394-400.
- [17] G. Liu, H. Gu and W. Su, "Development of random signal radars," *IEEE Transactions on Aerospace and Electronic Systems*, Vol.35, No.3, July 1999, pp.770-777.

- [18] S. Haykin, *Communication Systems*, John Wiley & Sons, Inc., 4th Edition, 2001.
- [19] J. G. Proakis and M. Salehi, *Communication Systems Engineering*, Prentice Hall, Upper Saddle River, New Jersey, 1994.
- [20] J. B. Thomas, *An Introduction to Statistical Communication Theory*, John Wiley & Sons, Inc., New York, 1969.
- [21] Y. Xu, R. M. Narayanan, X. Xu, and J. O. Curtis, "Polarimetric processing of coherent random noise radar data for buried object detection," *IEEE Transactions on Geoscience and Remote Sensing*, Vol.39, No.3, March 2001, pp.467-478.
- [22] M. Dawood, "Ultrawideband coherent random noise radar: theory and experiments," PhD. dissertation, University of Nebraska-Lincoln, April 2001.
- [23] D. S. Garmatyuk and R. M. Narayanan, "SAR imaging using fully random bandlimited signals," *IEEE 2000 APS Intl. Symp.*, Vol.4, Salt Lake City, Utah, July 16-21, 2000, pp.1948-1951.
- [24] D. C. Bell and R. M. Narayanan, "ISAR turntable experiments using a coherent ultrawideband random noise radar," *IEEE 1999 APS Intl. Symp.*, Vol.3, Orlando, FL, July 11-16, 1999, pp.1768-1771.
- [25] D. C. Bell, and R. M. Narayanan, "ISAR imaging using coherent random noise radar techniques", *Proc. SPIE Conference on Radar Processing, Technology, and Applications III*, (W. Miceli, Ed.), Vol.3462, July 1998, San Diego, CA, pp. 284-265.
- [26] D. J. Daniels, "Resolution of ultra-wideband radar signals," *IEE Proc.-Radar, Sonar Navig.*, Vol.146, No.4, Aug. 1999, pp.189-194.
- [27] F.J.Harris, "On the use of windows for harmonic analysis with the discrete Fourier transform," *Proc. of IEEE*, Vol.66, No.1, Jan. 1978, pp.51-83.
- [28] B. D. Steinberg, D. Carlson, and R. Bose, "High resolution 2-D imaging with spectrally thinned wideband waveforms", *Ultra-Wideband Short-Pulse Electromagnetics 2*, (Edited by L. Carin and L. B. Felsen), New York: Plenum Press, 1995, pp.563-569.

- [29] B. D. Steinberg, *Microwave Imaging with Large Antenna Arrays*, New York: Wiley, 1983.
- [30] L. Y. Astanin, A. A. Kostylev, Y. S. Zinoviev, and A. Y. Pasmarov, *Radar Target Characteristics: Measurements and Applications*, Boca Raton: CRC Press, 1994.
- [31] A. Segalovitz and B. D. Frieden, "A 'CLEAN'-type deconvolution algorithm," *Astron. Astrophys.*, Vol.70, 1978, pp.335-343.
- [32] J. Tsao, and B. D. Steinberg, "Reduction of sidelobe and speckle artifacts in microwave imaging: the CLEAN technique", *IEEE Transactions on Antennas and Propagation*, Vol.36, No.4, April 1988, pp.543-556.
- [33] X. Xu and Ram M. Narayanan, "Range sidelobe suppression technique for coherent ultra wide-band random noise radar imaging," *IEEE Transactions on Antennas and Propagation*, Vol.49, No.12, Dec. 2001, pp.1836-1842.
- [34] K. Takaba, "Projection method for solving a singular system of linear equations and its applications," *Numeriche Mathematik*, Vol.17, 1971, pp.203-214.
- [35] T. S. Huang, D. A. Barker, and S. P. Berger, "Iterative image restoration," *Applied Optics*, Vol.14, No.5, May 1975, pp.1165-1168.
- [36] R. Kapoor, A. Banerjee, G. A. Tsihrintzis, and N. Nandhakumar, "UWB radar detection of targets in foliage using alpha-stable clutter models," *IEEE Transactions on Aerospace and Electronic Systems*, Vol.35, No.3, July 1999, pp.819-834.
- [37] B. Walker, G. Sander, M. Thompson, B. Burns, R. Fellerhoff, and D. Dubbert, "A high-resolution, four-band SAR testbed with real-time image formation," *Proc. 1996 Intl. Geoscience and Remote Sensing Symp.*, Vol.III, Lincoln,NE, May 1996, pp.1881-1885.
- [38] A. Gustavsson, L. M. H. Ulander, L. E. Andersson, P. O. Frolind, H. Hellsten, T. Jonsson, B. Larsson, and G. Stenstrom, "The experimental airborne VHF SAR sensor

CARABAS: a status report," *Proc. 1996 Inter. Geoscience and Remote Sensing Symp. (IGARSS'96)*, Vol.III, Lincoln,NE, May 1996, pp.1877-1880.

- [39] J. W. McCorkle, "Early results from the Army Research Laboratory ultra-wide-bandwidth foliage penetration SAR," *Proc. SPIE on Underground and Obscured Object Detection*, Vol.1942, Orlando, FL, April 1993, pp.88-95.
- [40] L. A. Bessette, S. M. Crooks, and S. Ayasli, "P-3 ultra-wideband SAR, Grayling, Michigan, target and clutter phenomenology," *Proc. IEEE Radar Conf.*, Boston, MA, April 1999, pp.125-129.
- [41] M. F. Toups and S. Ayasli, "Results from the Maine 1992 foliage penetration experiments," *Proc. SPIE on Underground and Obscured Object Imaging and Detection*, Vol.1942, Orlando, FL, April 1993, pp.66-75.
- [42] D. A. Giglio, "Overview of foliage/ground penetration and interferometric SAR experiments," *Proc. SPIE on Algorithms for Synthetic Aperture Radar Imagery*, Vol.2230, Orlando, FL, April 1994, pp.209-217.
- [43] E. K. Walton and S. Gunawan, "Comparative analysis of UWB underground data collected using step-frequency, short pulse and noise waveforms," *Ultra-Wideband, Short-Pulse Electromagnetics*, Vol.3, Edited by C. E. Baum *et al.*, Plenum Press, New York, 1997, pp.511-516.
- [44] I. P. Theron, E. K. Walton, S. Gunawan, and L. Cai, "Ultrawide-band noise radar in the VHF/UHF band," *IEEE Transactions on Antennas and Propagation*, Vol.47, No.6, June 1999, pp.1080-1084.
- [45] F. T. Ulaby, K. Sarabandi, K. McDonald, M. Whitt, and M. C. Dobson, "Michigan microwave canopy scattering model," *Intl. J. of Remote Sensing*, Vol.11, No.7, July 1990, pp.1223-1253.
- [46] K. C. McDonald, M. C. Dobson, and F. T. Ulaby, "Using MIMICS to model L-band multiangle and multitemporal backscatter from a walnut orchard," *IEEE Transactions on Geoscience and Remote Sensing*, Vol.28, No.4, July 1990, pp.477-491.

- [47] M. A. Karam, F. Amar, and A. K. Fung, "Electromagnetic wave scattering from a forest or vegetation canopy: ongoing research at the University of Texas at Arlington," *IEEE Antennas and Propagation Magazine*, Vol.35, No.2, April 1993, pp.18-26.
- [48] M. A. Karam, A. K. Fung, R. H. Lang, and N. S. Chuahan, "A microwave scattering model for layered vegetation," *IEEE Transactions on Geoscience and Remote Sensing*, Vol.30, No.4, July 1992, pp.767-784.
- [49] L. Tsang, C. H. Chan, J. A. Kong, and J. Joseph, "Polarimetric signature of a canopy of dielectric cylinders based on first and second order vector radiative transfer theory," *J. Electromagn. Waves Applicat.*, Vol.28, No.3, May 1990, pp.315-324.
- [50] N. S. Chauhan, R. H. Lang, and K. J. Ranson, "Radar modeling of a boreal forest," *IEEE Transactions on Geoscience and Remote Sensing*, Vol.29 No.4 July 1991, pp.627-638.
- [51] B. T. Binder, M. F. Toups, S. Ayasli, and E. M. Adams, "SAR foliage penetration phenomenology of tropical rain forest and northern U.S. forest," *Proc. IEEE 1995 Int. Radar Conf.*, Washington D.C., May 1995, pp.158-163.
- [52] S. L. Durden, J. D. Klein, and H. A. Zebker, "Radar measurement of L-band signal fluctuations caused by propagation through trees," *IEEE Transactions on Antennas and Propagation*, Vol.39, No.10, Oct. 1991, pp.1537-1539.
- [53] S. L. Durden, J. D. Klein, and H. A. Zebker, "Measurement and simulation of signal fluctuations caused by propagation through trees," *Radio Science*, Vol.28, No.6, Nov.-Dec. 1993, pp.1049-1051.
- [54] G. C. Hsu, J. A. Kong, M. F. Toups, J. G. Fleischman, S. Ayasli, and R. T. Shin, "Electromagnetic modeling of foliage obscured point source response," *Proc. SPIE Conf. on Underground and Obscured Object Imaging and Detection*, Vol.1942, Orlando, FL, April 1993, pp.76-87.

- [55] K. Sarabandi and Y. Lin, "Simulation of interferometric SAR response for characterizing the scattering phase center statistics of forest canopies," *IEEE Transactions on Geoscience and Remote Sensing*, Vol.38, No.1, Jan. 2000, pp.115-125.
- [56] Y. Lin and K. Sarabandi, "A Monte Carlo coherent scattering model for forest canopies using fractal-generated trees," *IEEE Transactions on Geoscience and Remote Sensing*, Vol.37, No.1, Jan. 1999, pp.440-451.
- [57] N. C. Currie, R. D. Hayes, and R. N. Trebits, *Millimeter-Wave Radar Clutter*, Boston: Artech House, 1992, pp.14-23.
- [58] R. E. Walpole and R. H. Myers, *Probability and Statistics for Engineers and Scientists*, Fifth Edition, New York: Macmillan Publishing Company, 1993, pp.166-171.
- [59] J. Feder, "Fractals," *Plenum Press*, New York, 1988, p.235.
- [60] G. Franceschetti, A. Iodice, and D. Riccio, "Scattering from dielectric random fractal surfaces via method of moments," *IEEE Transactions on Geoscience and Remote Sensing*, Vol.38, No.4, July 2000, pp.1644-1655.
- [61] H. A. Wheeler, "The interpretation of amplitude and phase distortion in terms of paired echoes," *Proceedings of the IRE*, Vol.27, No.6, June 1939, pp.359-384.
- [62] C. R. Burrows, "Discussion to the interpretation of amplitude and phase distortion in terms of paired echoes," *Proceedings of the IRE*, Vol.27, No.6, June 1939, pp.384-385.
- [63] J. A. Henning, R. M. Narayanan, and X. Xu, "Design and performance of an UWB random noise foliage penetration radar," *Digest of 2000 USNC/URSI Radio Science Meeting*, Salt Lake City, Utah, July 2000, p.344.
- [64] M. Braunstein, J. Ralston, and D. Sparrow, "Signal processing approaches to radio frequency interference (RFI) suppression," *Proc. SPIE Conf. on Algorithms for Synthetic Aperture Radar Imagery*, (D. A. Giglio, ed.), Vol.2230, Orlando, FL, April 1994, pp.190-208.

- [65] B. H. Ferrell, "Interference suppression in UHF synthetic aperture radar," *Proc. SPIE Conf. on Algorithms for Synthetic Aperture Radar Imagery II*, (D. A. Giglio, ed.), Vol.2248, Orlando, FL, April 1995, pp.96-106.
- [66] M. Ressler, L. Happ, L. Nguyen, T. Ton, and M. Bennett, "The Army Research Laboratory ultra-wideband testbed radar," *Proc. of the IEEE 1995 International Radar Conference*, pp.686-691, May 1995.
- [67] R. Rau and J. H. McClellan, "Analytical models and postprocessing techniques for UWB SAR," *IEEE Transactions on Aerospace and Electronic Systems*, Vol.36, No.4, pp.1058-1074, Oct. 2000.
- [68] M. Soumekh, "Reconnaissance with ultra wideband UHF synthetic aperture radar," *IEEE Signal Processing Magazine*, Vol.12, No.4, pp.21-40, July 1995.
- [69] B. Borden, "Some issues in inverse synthetic aperture radar image reconstruction," *Inverse Problems*, Vol.13, pp.571-584, 1997.
- [70] E. F. Knott, J. F. Shaeffer, and M. T. Tuley, *Radar Cross Section*, Boston: Artech House, 1985.
- [71] M. Soumekh *Synthetic Aperture Radar Signal Processing*, New York: John Wiley and Sons, Inc, pp.382-384, 1999.
- [72] G. T. Ruck, D. E. Barrick, W. D. Stuart, and C. K. Krichbaum, *Radar Cross Section Handbook*, New York: Plenum, 1970.
- [73] S. R. J. Axeleson, "Frequency and azimuthal variations of radar cross section and their influence upon low-frequency SAR imaging," *IEEE Transactions on Geoscience and Remote Sensing*, Vol.33, No.5, pp.1258-1265, Sept. 1995.
- [74] L. M. Novak, G. J. Owirka, and A. L. Weaver, "Automatic target recognition using enhanced resolution SAR data," *IEEE Transactions on Aerospace and Electronic Systems*, Vol.35, No.1, Jan. 1999, pp.157-175.

- [75] K. M. Cuomo, J. E. Piou, and J. T. Mayhan, "Ultrawide-band coherent processing," *IEEE Transactions on Antennas and Propagation*, Vol.47, No.6, June 1999, pp.1094-1107.
- [76] B. H. Borden, "Enhanced range profiles for radar-based target classification using monopulse tracking statistics," *IEEE Transactions on Antennas and Propagation*, Vol.43, No.8, Aug. 1995, pp.759-765.
- [77] L. C. Potter and R. L. Moses, "Attributed scattering centers for SAR ATR," *IEEE Transactions on Image Processing*, Vol.6, No.1, Jan. 1997, pp.79-91.
- [78] D. J. Andersh, S. W. Lee, J. Moore, D. Sullivan, J. Hughes, and H. Ling, "Xpatch prediction improvements to support multiple ATR applications," *Proc. of SPIE on Radar Sensor Technology III*, Vol.3395, Orlando, FL, April 1998, pp.108-119.
- [79] R. Bhalla and H. Ling, "Three-dimensional scattering center extraction using the shooting and bouncing ray technique," *IEEE Transactions on Antennas and Propagation*, Vol.44, No.11, 1996, pp.1445-1453.
- [80] M. L. Hastriter and P. J. Collins, "Range dependent target scattering in the intermediate-zone," *Proc. of 1998 IEEE Radar Conf.*, Dallas, TX, May 12-13, 1998, pp.387-392.
- [81] A. Broquetas, J. Palau, L. Jofre, and A. Cardama, "Spherical wave near-field imaging and radar cross-section measurement," *IEEE Transactions on Antennas and Propagation*, Vol.46, No.5, May 1998, pp.730-735.
- [82] D. L. Mensa, *High Resolution Radar Cross-Section Imaging*, Boston, MA: Artech House, 1991.
- [83] R. A. Marr and U. H. W. Lammers, "Coherent 3-D Imaging of model targets," *Proc. of 1997 IEEE National Radar Conf.*, Dallas, TX, May 12-13, 1997, pp.289-294.
- [84] G. A. Showman, K. J. Sangston, and M. A. Richards, "Correction of artifacts in turntable inverse synthetic aperture radar images," *Proc. of SPIE on Radar Sensor Technology II*, Vol.3066, Orlando, FL, April 1997, pp.40-51.

- [85] L. C. Graham, "Synthetic interferometer radar for topographic mapping," *Proc. IEEE*, Vol.62, No.6, June 1974, pp.763-768.
- [86] C. V. Jakowatz, Jr., D. E. Wahl, D. C. Ghiglia, and P. A. Thompson, *Spotlight-Mode Synthetic Aperture Radar: A Signal Processing Approach*, Boston: Kluwer Academic Publishers, 1996, pp.273-348.
- [87] C. Prati, F. Rocca, M. Guanieri, and E. Damonti, "Seismic migration for SAR focusing: interferometric applications," *IEEE Transactions on Geoscience and remote sensing*, Vol.28, No.4, July 1990, pp.627-640.
- [88] M. Soumekh, "Automatic aircraft landing using interferometric inverse synthetic aperture radar imaging," *IEEE Transactions on Image Processing*, Vol.5, No.9, Sept.1996, pp.1335-1345.
- [89] A. K. Gabriel, R. M. Goldstein, and H. A. Zebker, "Mapping small elevation changes over large areas: differential radar interferometry," *Journal of Geophysical Research*, Vol.94, No.B7, July 1989, pp.9183-9191.
- [90] G. Franceschetti and R. Lanari, *Synthetic Aperture Radar Processing*, Boca Raton: CRC Press, 1999, pp.167-222.
- [91] A. F. Yegulalp, "Fast backprojection algorithm for synthetic aperture radar," *Proc. of 1999 IEEE Radar Conf.*, Boston, MA, April 20-22, 1999, pp.60-65.
- [92] B. H. Borden, "Requirements for optimal glint reduction by diversity methods," *IEEE Transactions on Aerospace and Electronic Systems*, Vol.30, No.4, Aug. 1994, pp.1108-1114.
- [93] B. H. Borden, "High-frequency statistical classification of complex targets using severely aspect-limited data," *IEEE Transactions on Antennas and Propagation*, Vol.34, No.12, Dec. 1996, pp.1455-1459.
- [94] X. Xu, H. Luo, and P. Huang, "3-D Interferometric ISAR images for scattering diagnosis of complex radar targets," *Proc. of 1999 IEEE Radar Conf.*, Boston, MA, April 20-22, 1999, pp.237-240.

- [95] S. R. Degraaf, "SAR imaging via modern 2-D spectral estimation methods," *IEEE Transactions on Image Processing*, Vol.7, No.5, May 1998, pp.729-761.
- [96] I. J. Gupta, "High-resolution radar imaging using 2-D linear prediction," *IEEE Transactions on Antennas and Propagation*, Vol.42, No.1, Jan. 1994, pp.31-37.
- [97] S. L. Borison, S. B. Bowling, and K. M. Cuomo, "Super-resolution methods for wideband radar," *The Lincoln Laboratory Journal*, Vol.5, No.3, 1992, pp.441-461.
- [98] H. J. Li, N. H. Farhat, and Y. S. Shen, "A new iterative algorithm for extrapolation of data available in multiple restricted regions with applications to radar imaging," *IEEE Transactions on Antennas and Propagation*, Vol.35, No.5, May 1987, pp.581-588.
- [99] S. R. DeGraaf, "Parametric estimation of complex 2-D sinusoids," *4th IEEE ASSP Soc. Annual Workshop on Spectrum Estimation and Modeling*, Minneapolis, MN, 3-5 Aug. 1988, pp.391-396.
- [100] M. W. Tu, I. J. Gupta, and E. K. Walton, "Application of maximum likelihood estimation to radar imaging," *IEEE Transactions on Antennas and Propagation*, Vol.45, No.1, Jan. 1997, pp.20-27.
- [101] J. Li, and P. Stoica, "Efficient mixed-spectrum estimation with applications to target feature extraction," *IEEE Transactions on Signal Processing*, Vol.44, No.2, Feb. 1996, pp.281-295.
- [102] Z. Bi, J. Li, and Z. Liu, "Super resolution SAR imaging via parametric spectral estimation methods," *IEEE Transactions on Aerospace and Electronic Systems*, Vol.35, No.1, Jan. 1999, pp.267-281.
- [103] R. Wu, J. Li, and P. Stoica, "SAR image formation via semiparametric spectral estimation," *IEEE Transactions on Aerospace and Electronic Systems*, Vol.35, No.4, Oct. 1999, pp.1318-1333.
- [104] G. R. Benitz, "Adaptive high-definition imaging," *Proc. of the SPIE Conf. on Algorithms for SAR*, Orlando, FL, April 1994, pp.106-119.

- [105] S. Barbarossa, L. Marsili, and G. Mungari, "SAR super-resolution imaging by signal subspace projection techniques," *AEU International Journal on Electronics and Communications*, Vol.50, No.2, March 1996, pp.133-138.
- [106] J. W. Odendaal, E. Bernard, and C. W. I. Pistorius, "Two dimensional superresolution radar imaging using the MUSIC algorithms," *IEEE Transactions on Antennas and Propagation*, Vol.42, No.10, Oct. 1994, pp.1386-1391.
- [107] J. Li, and P. Stoica "An adaptive filtering approach to spectral estimation and SAR imaging," *IEEE Transactions on Signal Processing*, Vol.44, No.6, June 1996, pp.1469-1484.
- [108] M. R. Palsetia, and Jian Li, "Using APES for interferometric SAR imaging," *IEEE Transactions on Image Processing*, Vol.7, No.9, Sept. 1998, pp.1340-1353.
- [109] G. R. Benitz, "High-definition vector imaging for synthetic aperture radar," *Proc. of the 31st Asilomar Conf. on Systems, Signals and Computers*, Pacific Grove, CA, Nov. 1997, pp.1204-1209.
- [110] S. R. DeGraaf, "Sidelobe reduction via adaptive FIR filtering in SAR imagery," *IEEE Transactions on Image Processing*, Vol.3, No.5, May 1994, pp.729-761.
- [111] H. C. Stankwitz, R. J. Dallaire, and J. R. Fienup, "Nonlinear apodization for sidelobe control in SAR imagery," *IEEE Transactions on Aerospace and Electronic Systems*, Vol.31, No.1, Jan. 1995, pp.267-279.
- [112] H. C. Stankwitz, and M. R. Kosek, "Super-resolution for SAR/ISAR RCS measurement using spatially variant apodization (Super-SVA)," *Proc. of 17th Meeting and Symposium of the Antenna Measurement Techniques Association*, Nov. 13-17, 1995, pp.251-256.
- [113] H. C. Stankwitz, and M. R. Kosek, "Sparse aperture fill for SAR using Super-SVA," *Proc. of 1996 IEEE Radar Conference*, pp.70-75.
- [114] B. H. Smith, "Generalization of spatially variant apodization to noninteger Nyquist sampling rates," *IEEE Transactions on Image Processing*, Vol.9, No.6, June 2000, pp.1088-1093.

- [115] J. A. C. Lee, and D. C. Munson, Jr., "Spatially variant apodization for image reconstruction from partial Fourier data," *IEEE Transactions on Image Processing*, Vol.9, No.11, Nov. 2000, pp.1914-1925.
- [116] G. W. Lank, and N. M. Chung "CFAR for homogeneous part of high-resolution imagery," *IEEE Transactions on Aerospace and Electronic Systems*, Vol.28, No.2, April 1992, pp.370-382.
- [117] A. W. Rihaczek, and S. J. Herschkowitz, "Theory and Practice of Radar Target Identification," *Artech House, Inc.*, Norwood, MA, 2000, pp.705-711.

Appendix: Publication List

- [1] Ram M. Narayanan, and Xiaojian Xu, "Foliage penetration stripmap SAR imaging using UWB random noise waveform," *Proc. of the 6th Ultra-Wideband Short-Pulse Electromagnetics Conference of the AMEREM 2002 Symposium*, Annapolis, MD, June 2002.
- [2] Xiaojian Xu and Ram M. Narayanan, "SAR image enhancement using noninteger Nyquist SVA technique," *Digest of 2002 IEEE AP-S Intl. Symp.*, Vol.4, San Antonio, TX, June 2002, pp.298-301.
- [3] Cihan Kumru, Ram M. Narayanan, and Xiaojian Xu, "Polarimetric Image Processing of an Ultra Widedand FOPEN Random Noise Radar," *Digest of 2002 USNC/URSI National Radio Science Meeting*, San Antonio, TX, June 2002, p.202.
- [4] Ram M. Narayanan, Xiaojian Xu, and Cihan Kumru, "UWB random noise radar FOPEN imaging: signal processing and experimental results," *AFOSR 13th Annual Electromagnetics Workshop*, San Antonio, TX, Jan. 17-19, 2002, pp.21-24.
- [5] Xiaojian Xu and Ram M. Narayanan, "Range sidelobe suppression technique for coherent ultra-wideband random noise radar imaging," *IEEE Transactions on Antennas and Propagation*, Vol.49, No.12, Dec. 2001, pp.1836-1842.
- [6] Xiaojian Xu and Ram M. Narayanan, "FOPEN SAR imaging UWB step-frequency and random noise waveforms," *IEEE Transactions on Aerospace and Electronic Systems*, Vol.37, No.4, Oct. 2001, pp.1287-1300.
- [7] Xiaojian Xu and Ram M. Narayanan, "Three-dimensional interferometric ISAR imaging for target scattering diagnosis and modeling," *IEEE Transactions on Image Processing*, Vol.10, No.7, July 2001, pp.1094-1102.
- [8] Ram M. Narayanan, Xiaojian Xu and Joseph Henning, "Comparison of FOPEN SAR imaging using ultra-wideband step-frequency and random noise waveforms," *AFOSR 12th Annual Electromagnetics Workshop*, San Antonio, TX, Jan. 11-13, 2001, pp.14-18.

- [9] Xiaojian Xu and Ram M. Narayanan, "Imaging performance analysis of a FOPEN UWB random noise radar," *Digest of 2001 IEEE AP-S Intl. Symp.*, Vol.4, Boston, July 8-13, 2001, pp.273-276.
- [10] Ram M. Narayanan, Xiaojian Xu and Joseph Henning, "Random noise polarimetry technique for covert detection of targets obscured by foliage," *AFOSR 11th Annual Electromagnetics Workshop*, San Antonio, TX, Jan. 13-15, 2000, pp.17-21.
- [11] Xiaojian Xu and Ram M. Narayanan, "A comparative study of UWB FOPEN radar imaging using step-frequency and random noise waveforms," *Digest of 2000 IEEE AP-S Intl. Symp.*, Vol.4, Salt Lake city, July 16-21, 2000, pp.1956-1959.
- [12] Joseph A. Henning, Ram M. Narayanan, and Xiaojian Xu, "Design and performance of an ultra-wideband random noise foliage penetration radar," *Digest of 2000 USNC/URSI National Radio Science Meeting*, Salt Lake city, July 16-21, 2000, p.344.
- [13] Xiaojian Xu and Ram M. Narayanan, "3-D radar cross section imaging using interferometric ISAR technique," *Proc. of the 22nd Antenna Measurement Techniques Association Annual Meeting and Symp.*, Philadelphia, Oct. 16-20, 2000, pp.56-61.